Smart Technology Centre
Institute of Fundamental Technological Research
Polish Academy of Sciences

Doctor of Philosophy Dissertation

Adaptive impact absorbers based on magnetorheological fluids

by

Grzegorz Mieczysław Mikułowski

Supervisor: Prof. Jan Holnicki-Szulc

Warsaw, 2008

To my family.

Contents

Acknowledgements

The author gratefully acknowledges the financial support through FP6 EU Project, Adaptive Landing Gears for Improved Impact Absorption, ADLAND (FP6-2002-Aero- 1, 2003-2006), developed by a consortium: Institute of Fundamental Technological Research (IPPT PAN) Warsaw, EADS Munich, PZL Mielec, Institute of Aviation Warsaw, FhGISC Wuerzburg, CEDRAT-TECH Grenoble, USFD Sheffield, MESSIER-DOWTY Velizy. Financial support was also obtained via the Polish Research Project MAT-INT (PBZKBN- 115/T08/2004). The authors would like to gratefully acknowledge the Faculty of Cars and Heavy Machinery, and the Warsaw University of Technology for cooperation in the field of measurement software development (LabView software). Fragments of this work are parts of a monograph in preparation [25].

Chapter 1

Introduction

Adaptive impact absorption (AIA) is a modern control problem being solved nowadays for several transportation and industry branches [1, 2, 3, 4, 5, 6]. The objective of the impact absorption process is dissipation of impact energy with simultaneous generation of the minimal deceleration on the protected structure. However, in many applications the exploitative impacts, which the absorbers are exposed to, exhibit a broad variety in the domain of their energies. The passive devices that are currently in usage, do not offer a proper behaviour for various impact conditions, what effects in needless overloading of the protected structures. A possible solution for minimisation of the deceleration level is using of adaptive shock absorbers that would enable adjusting theirs damping force characteristics to the actually recognised impact energy.

An an example of application, which is exhibited during regular operation to repetitive impact loadings, are aircrafts in touchdown. The problem of impact energy in this case of application is uniquely difficult as landing gears must operate properly in a wide range of conditions that may occur during landing. Civil aircraft may be endangered by a variety of weather conditions which may enforce a hard landing. Situations when the vertical landing speed at the moment of impact is higher than 1.5 m/s is undesirable and exceeding the sink speed level of 3 m/s may cause serious increase of the relative fatigue of the aeroplane's structures. Application of adaptive landing gear (ALG) may improve the impact absorption capabilities of the existing landing gears and, therefore, to reduce the threat of damage of the fleet and to prolong the service life of the air vehicles. The economical aspect plays here a significant role since the air transport rises continuously its share in public transport during the recent years.

Except the foreseen benefits in civil aviation, the adaptive landing gears may play a key role in the case of landing systems for helicopters in the coastguards services. The air vehicles being used in the rescue actions usually must operate

in heavy weather conditions. Despite the difficult circumstances, it sometimes happens that pilots must land on a deck of a threatened ship or mining platform. Having in mind that usually such an operation must be realised in presence of a strong wind, the landing is extremely hazardous for the aircraft's and ship's crews. In these circumstances, the adaptive landing gears would play very important role as, device that improve significantly safety of landings of the air vehicles and lower the risk of accidents.

This work is devoted to analysis of adaptive impact absorbers applied as aircraft landing gears. The presented work discusses a possibility of utilisation of active dampers based on magnetorheological fluids (MRF) as the actuator for the proposed system. Control issues of an impact absorption system are widely presented.

1.1 Design of shock absorbers

The general objective of shock absorbers is to mitigate undesirable dynamic effects caused by accidental impact forces acting on the protected structure. The impacts can be considered in catastrophic and non-catastrophic scale, but in both cases the proper energy absorption capabilities of the landing gears and structural elements are significant from the point of view of safety [7, 8, 9]. In the non-catastrophic cases, one of the forces' origins are kinetic excitations coming from the shock of the base, where it is fixed to the structure (e.g. road vehicles, rail vehicles, aircraft during landing and taxiing) [10, 11]. Impacts result in the impulsive generation of acceleration levels within the suspension. The objective of the shock absorbers is then to minimize the acceleration peak levels being transferred to the structure.

Let us analyse a structure that is schematically presented in Fig. 1.1. The isolated mass m (object), which can be considered as a rigid body with six degrees of freedom, is connected via a shock absorbing device to a base. If the shock appears in such a direction that the resultant force in the shock absorber crosses the centre of the mass, a translational vibration will be induced. In other situations, coupled rotational vibrations will also appear additionally. Let us assume that the condition for excitation of the translational vibrations is satisfied and also the direction of the object's movement is known. For these assumptions the system can be treated as 1 DoF.

Let $z(t)$ and $y(t)$ describe absolute displacements of the object and the base. So

$$x(t) = y(t) - z(t) \tag{1.1}$$

is the relative displacement of the object and base, which is equivalent to the deflection of the shock absorbing device consisting of a spring k and the damper c. When the shock absorbers force is denoted as $Q(x, \dot{x})$ then the equation of

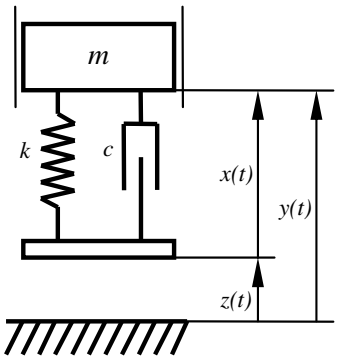

Figure 1.1: Model of a damped oscillator excited with impact loading.

motion of the object can be formulated as follows:

$$m\ddot{y}(t) + Q(x, \dot{x}) = 0. \tag{1.2}$$

Absolute acceleration of the object is

$$\ddot{y}(t) = \ddot{x}(t) + \ddot{z}(t) \equiv a(t). \tag{1.3}$$

The efficiency of the shock absorption process is described as follows:

$$\frac{max|z(t)|}{max|a(t)|} \equiv \sigma, \tag{1.4}$$

where σ is shock transmissibility that depicts the amount of acceleration reduction [10, 11], i.e. how much the maximum acceleration of the object is lower in comparison to the acceleration of the base after impact. Naturally, an effective shock absorber has to have $\sigma > 1$, and the higher the number is, the better will be the shock absorber designed. However, in order to reach a significantly high value of the ratio σ, the shock absorbing elements (k and c in Fig. 1.1) must be capable of long deflections. In other words, the stroke of the shock absorber must be sufficiently large. On the other hand, the necessity to minimize the shock absorber's size drives the designer to reduce the stroke.

For the above reasons the designer must propose a solution that maximizes the acceleration reduction, whilst minimizing the size of the shock absorber's housing. As a consequence, there are acceptable values of deflections and accelerations assumed:

$$\text{accept } \max|a(t)| \equiv W \quad \text{and} \quad \text{accept } \max|x(t)| \equiv X.$$

The limits are imposed by strength and design considerations. On one side, it is important to limit the forces affecting the structure. On the other side, it

is important to prevent the occurrence of shock strut bottoming, which would result in high force peaks. As a result, the following conditions should be satisfied for every time instant t of the movement:

$$max|a(t)| \leq W, \tag{1.5}$$

$$max|x(t)| \leq X. \tag{1.6}$$

The presented methodology of the shock absorbers conceptual design allows tuning of the damping and stiffness characteristics to one particular magnitude of impact energy. However, in the case of landing gear shock absorbers, the impacts vary significantly between landings. According to the industry regulations [12], all landing gears are optimized for the case of an impact with the maximum aircraft weight and sink speed (i.e. max. impact energy). This is purely for the reason of safety. This situation results in non-optimal landing gear behaviour for more common landings with lower impact energies. More specifically, this non-optimal behaviour results in the generation of very high damping forces and an unwanted reduction in the effective stroke. Consequently, the acceleration of the protected structures is increased. These unnecessary overloads of the structure significantly influence the fatigue processes.

A solution of the mentioned problem is the introduction of an adaptive landing gear, which has the possibility of fitting its characteristics to particular landing sink speeds and weights of the aircraft. This adaptation of the shock absorber would allow optimal performance to be achieved for a wide range of impact velocities and weights of the structure. The introduction of such a system would improve the fatigue of the protected structure as a result of reduced accelerations that the structure is subjected to. The statistical benefit from the introduction of an ALG was estimated as 16% [13].

The force generated by the LG depends on the difference between the fluid pressures Δp in the lower and upper chamber of the strut [14, 15] (Fig. 1.2). This force can be controlled in three ways. The pressure drop Δp can be modified via control of the gas pressure in the upper chamber, or by regulating the fluid flow resistance across the orifice (using a fast actuated valve) or by changing the rheological properties of the fluid in the gap. In the following study the third option is analysed.

1.2 Active landing gears

The primary objective for landing gears in aeroplanes from the beginning of their existence, was to soften the moment of touchdown and therefore to avoid damages and fatigue in the airframes of aircraft during ground operations. The first landing gears were made in the form of stiff structures where only the wheels exhibited viscoelastic properties. Development of the technology and increase of

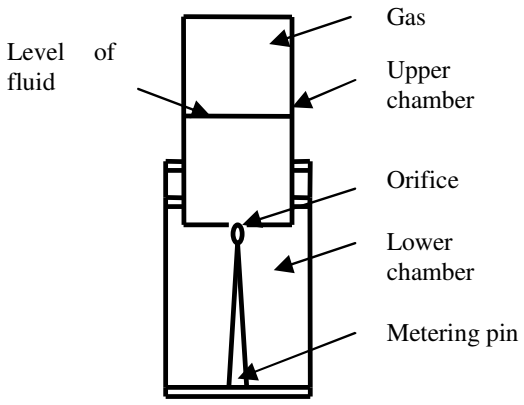

Figure 1.2: Scheme of an oleo-pneumatic shock strut with metring pin.

the speeds and masses of aeroplanes, drove the designers to implement more and more advanced solutions for the landing gears, which adapted elastic and dissipative properties [16].

Intensive development of landing gears started in the United States in 1950's when oleo-pneumatic design became popular and widely employed. These shock absorbers were composed of a combination of gas spring and two hydraulic chambers, divided by an orifice providing a resistant reaction of hydraulic fluid pressed through it. This type of shock absorbers was reported to have the highest efficiency in relation to the weight [14] but it also demonstrated a problem with tuning of its properties for wide demands of the touchdown operation. The problem appeared because the reacting forces produced by landing gears are awaited to vary in the particular phases of the landing loading. Additionally, the same landing gear must also perform satisfactorily during taxi operations. However, the hydraulic orifices of constant geometries were producing the reaction in linear relation to the velocity of the piston. It was quickly determined as beneficial that the hydraulic reaction was adjustable during the operation of the landing shock struts. The first innovation that was introduced to the oleo-pneumatic shock absorbers was the metering pin, which modulated the cross-section of the orifice depending on the position of the piston as depicted in Fig. 1.2 [14].

Extended research on behaviour of oleo-pneumatic landing gears and on its analytical prediction was conducted by NACA researchers. The objective was development of modelling methods for landing gears' behaviour and design tools. The studies were conducted as numerical analyses with laboratory validations [15, 17] and in parallel, the behaviour of landing gears was measured on especially equipped aeroplanes [18]. One of the first methods of calculation of the metering pin's cross-section was proposed and described in [19].

Development of supersonic aeroplanes in 1960's introduced a new class of problems in front of landing gears designers. The ground-induced dynamic and vibration problems were magnified because of increased structural flexibility of the slender bodies, thin-wing designs and higher take-off and landing speeds. During design studies and investigations in particular designs, there were reported extremely high vibration levels of fuselages during take-off [20]. In these circumstances, the primary objective for landing gears were extended to the effective devices for mitigation of vibrations. From the beginning of 1970's a concept of active landing gear started to be considered as a solution for the vibration problems [21].

The active landing gear were defined as shock struts with actively controlled damping force. The control procedure contained increasing or decreasing, according to an applied control strategy, the internal hydraulic pressure by means of external reservoirs of compressed medium. Initially the developers of the new type of the landing gears were focused on recognition of the character of the phenomenon, analytical modelling and assessing the feasibility of the active landing gear's behaviour [22, 23]. The first results were very promising in the field of the vibration mitigation, but technological problems were reported since the estimated flow rates of the hydraulic fluid in the system were predicted up to 1000 litres per minute [22]. At the beginning of 1980's the new concept was matured to the phase of prototype system that was designed in accordance to all aeronautical regulations [24, 25] and then tested in experimental field of Langley Research Centre on the impact and roll-out operation [26, 27]. These tests have shown that the device is effective in reduction of dynamics effects on the airframe but it was also pronounced a significant unfavourable influence of bending of the landing gear during spin-up phase of touchdown. In 1990's the active landing gear was adapted for employment in several military aircraft as reported in [28, 29, 30]. The actively controlled landing gear were analysed for utilisation in military aviation also in Europe in 1990's [31].

The presented active solutions were characterised by high energy consumption due to necessity of delivering of high pressures, and thereafter these were generating high power costs. Taking into account a large number of parts in the design of the landing gears, these devices were probably much less reliable in comparison to the traditional landing gears. However, the load control feature is very desired in the undercarriage and therefore, in 1990's a new proposition became widely discussed [32, 33]. This was an introduction to the landing gears of a semi-active technology. This proposition had a serious advantage in comparison to the active solution since the main idea was managing of energy dissipation in the landing gears via controllable damping force, but without the necessity of adding hydraulic energy to the system. The designs were focused on optimal control development and possible actuation systems analysis [32, 34, 35]. After

year 2000 scientific research centres were reporting the results of experimental testing of the semi-active landing gears [36, 37]. The proposed solutions were employing fast servo-valves mounted in the system [36].

Another possibility of development of a semi-active landing gear is to employ a magnetorheological fluid instead of hydraulic oil. This functional fluid exhibits a possibility of changing its effective viscosity under influence of externally provided magnetic field. This feature of the medium allows to control its flow via modification of the external magnetic field density. This solution has the following advantages in comparison to classical oil and valves: simplicity of design as the fluid paths require no valves, low power consumption as the power is needed only to supply an electromagnet coil, high reliability as the solution is free of complicated mechanical systems and fast moving parts.

In accordance to the presented discussion, a concept of adaptive landing gear based on a magnetorheological fluid was analysed in this research. The idea of magnetorheological landing gear was the subject of European project developed in frame of 6FP entitled "Adaptive landing gears for improved impact absorption" [38] and part of the designing problems were presented in the following publications: [6, 39, 40].

1.3 Functional fluids

Magnetorheological fluids belong to the class of functional materials defined as materials that exhibit changes in their mechanical properties under the influence of an external non-mechanical excitation i.e. electrical or magnetic. Examples of the materials can be found among solids and fluids. Solids belonging to this class are piezoceramics [41, 42], which change their geometry due to applied voltage, or magnetorheological elastomers [43], which change their rheological properties under influence of magnetic field. Sensitive to magnetic field density is also the group of magnetostrictive materials [44, 45] that change the geometry. To the group of functional fluids belong electrorheological and magnetorheological fluids, which change their apparent rheological properties in response to the applied fields, relatively: electric and magnetic. In this study magnetorheological fluids are in the scope of research.

Magnetorheological fluids are non-colloidal suspensions consisting of two main components: micron-sized particles made of soft magnetic materials and carrier fluid with non-magnetic characteristic [46, 47, 48]. Commonly the magnetic materials are iron oxides (Fe_2O_3 and Fe_3O_4), and for the carrier fluids the following ones are used: water, silicon, mineral or synthetic oil and glycerol. Typically it contains between 30 and 35 % of the ferroparticles by volume, which is correlated with typical density on the level of 3.5 to 4 g/cm^3. Magnetorheological fluids can operate in the temperature range -40 – 150 Celsius degrees and are insensitive to

contaminants.

The phenomenological explanation of the effects taking place in the fluid in the presence of magnetic field can be presented as follows. Under influence of an externally applied magnetic field, the ferromagnetic particles distributed randomly in the volume of carrier fluid form chains connecting the magnetic poles as presented in Fig. 1.3. In the result the fluid exhibits a yield stress, which is in the interval from 50 to 100 kPa under the magnetic flux $\approx$250 kA/m.

The magnetorheological fluids can be employed in three modes of operation, which are depicted in Fig. 1.4 A, B and C. In the first - flow mode, the MRF's were under pressure gradient developed between two ends of the orifice presented in Fig. 1.4 A. In this mode MR fluid flows between stationary poles and the magnetic field causes a controllable resistance to flow of the medium, which in result modulates the pressure and acts as a valve. Incorporation of such a valve to connect chambers of a hydraulic damper gives a possibility of gaining the controllable reaction damping force.

The second operational mode of MRF is direct shear depicted in Fig. 1.4 B. In this configuration, the magnetic poles are in the relative movement and the MRF distributed between them is under pure shear. This mode of operation is widely employed in designs of brakes or clutches [49, 50].

In the third operational mode the MRF is squeezed between the poles in the direction parallel to the lines of the magnetic field as depicted in Fig. 1.4 C. In this concept, reacting forces that can be obtained are much higher than in flow and shear modes but the displacements are limited to a few millimetres. This mode of MRF operation can be used for designing of bumpers or fenders with small strokes.

MRFs have time-dependent properties, a finite time is required for the particles to realign as they were sheared. When the excitation is changed this time is found to be less than one millisecond. The delay time here depends on the inertia of the particles. In wide class of cases they proved to be an excellent choice for applications where strong dynamic features are required [48].

The devices based on MR technology are widely developed, designed and tested by researchers and some applications are already commercialised. The most widely considered application field for the MRF is semi-active mitigation of vibration. The applications were proposed for protection of civil constructions against seismic threatens [51, 52] as well as for semi-active vehicle suspensions [53, 54, 55]. The MR technology was also applied in prosthetics where an artificial knee was developed [47]. All of the mentioned applications employ linear MR dampers.

Another group of applications that utilise the MRF are rotary brakes and clutches. These devices allow to mitigate a wide class of undesirable dynamic effects appearing on rotating shafts or axles [49, 56]. For example, a rotary break

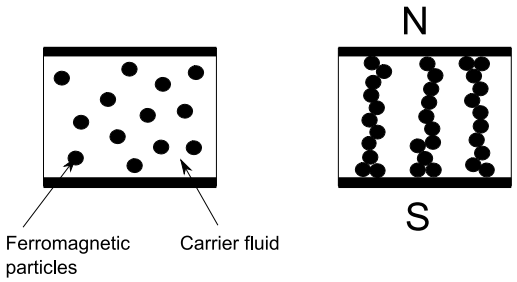

Figure 1.3: Principle of MRF behaviour.

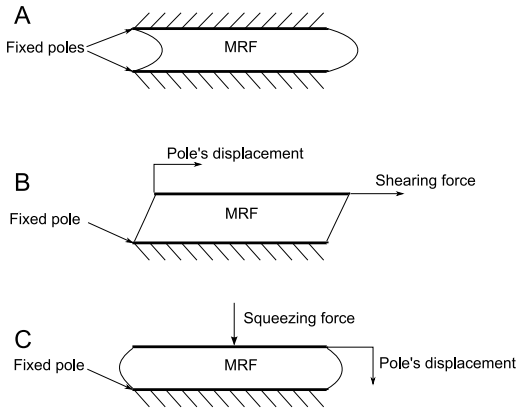

Figure 1.4: Modes of MRF's operation.

was developed to protect the patient lying on the bed in ambulance from a shock due to sudden break [57].

In the recent years conceptual research was performed on an adaptive landing gears actuated via magnetorheological fluids, cf the ADLAND project [38, 58, 6, 59]. The implementation of the MR fluid into the shock absorber gives an unique opportunity to control the pressure drop Δp between the upper and lower chamber in a continuous manner. Having the magnetic field generator incorporated around the hydraulic orifice, one can reach a controllable valve effect by means of control of the local apparent viscosity of the fluid.

1.4 Background, objectives and composition of the thesis

A major part of the present research was carried out under the ADLAND project [38] - Adaptive landing gear for improved impact absorption - developed by an European consortium in the frame of the 6th Framework Program. The project partners have investigated a possibility of incorporating of various semi-active actuators into classical landing gear in order to assess the feasibility of development of adaptive landing gear for a civil aircraft. One of the key methods developed in

the project was MR technology and consequently, an appropriate control system must have been studied.

The objective of application of the magnetorheological fluids into the aircraft landing gear had driven the researchers to the necessity of performing a deep research on the MR fluid's mechanics under the flow mode of operation. This requirement was fulfilled via conducting of an elementary research program on an intentionally built testing stand. Consequently, the objective of this research was:

To derive and experimentally validate a model of flow of MR fluid in the conditions of significant field density variation.

The original author's contribution was:

- building of the mockup for flow visualisation of the MR fluid
- formulation of a more precise flow law for MRF under non-homogeneous magnetic field
- development of analytically based model of a magnetorheological damper and its experimental verification

The task was completed on the example of a commercially available MR damper used in the research.

The feasibility of impact absorbers based on MRF for the adaptive landing gears depend strongly on the response time exhibited by the actuation system. An advanced control system must have been designed in such a way that allow the actuator to operate with time delays below 5 ms (0.005 s). Moreover, the developed control strategy must have been able to meet all of the specific requirements and constraints typical for aviation. Consequently, the second key objective of the present research was:

To develop and experimentally validate a control procedure for adaptive impact absorbers based on magnetorheological fluids.

The analysed control procedure primarily focused on the impact phase of an aircraft's landing as this is the crucial point in assessment of the feasibility of the system.

The original author's contribution was:

- building of the stand for dropping tests able to demonstrate the concept of the adaptive landing gear
- programming of the controller for the system with the response time equal or less 0.005 s

- integration of the adaptively controlled ALG model based on MR damper RD-1005-3 and the developed controller
- experimental verification of the ALG concept
- numerical and experimental assessment of the potential improvement in the behaviour of landing gears on an example of an existing aircraft

This work was divided into two parts, both related to the magnetorheological fluids. The first part was devoted to the topic of basic mechanics of the medium in the flow mode. The key problem presented in the first part of the research was derivation of a more precise law of flow for MRF. Then the analytical model of magnetorheological damper was formulated and validated experimentally.

The second part of the work was devoted to the problem of control of the MR devices under operation in Adaptive Impact Absorption applications. This part was focused on the analysis of challenges in design and the proposition of control algorithm that would enable us to process the control within the time limits characteristic for the impact phenomenon.

Composition of the work

The thesis was organised as follows:

Chapter 2 discusses the area of the fundamental mechanics of magnetorheological fluids. It starts with a literature review, which gives an overview of MRF modeling issues and current problems that researchers are faced to. The main part of the chapter presents a model used in this research for description of MRF in flow mode, where there is a significant fluctuation of magnetic flux density across the flow orifice. Finally, an experimental verification of the results is presented on an intentionally fabricated device, which allows the visualisation of the MRF under flow mode.

Chapter 3 presents an analysis of operation and formulation of modelling of a magnetorheological damper manufactured by LORD Corporation. That damper was the dissipative magnetorheological device used in the experiments for this study. An analytically formulated model of the device is proposed, which incorporates all of the physical effects occurring in the device. A special attention was applied to the problem of modelling of MR fluid flow in the device with reference to Chapter 2.

Chapter 4 presents a discussion devoted to methods of accelerating of the MR devices operation. The main sources of the time delays in the execution systems are presented and the solutions are proposed. The discussion contains a set of experimental examples for illustration of the described methods.

Chapter 5 presents issues that are connected to implementation of the MR fluids in the adaptive landing gears. The objective of this chapter is to present

the operation of an experimental system devoted to adaptive impact absorption. The results of the research depict the feasibility of an AIA based on MRF. A complete adaptive control system was constructed and validated experimentally.

Chapter 6 introduces a discussion about the gains that can be obtained as a result of using the controlled AIA systems. The special attention here is given to the potential for improvement that would be possible to be obtained in aircraft landing gears. The analysis was performed on the numerical example of an existing aircraft.

Chapter 7 presents the key conclusions of this research and some suggestions for further work.

Chapter 2

Modelling of MR fluid's flow

2.1 Introduction

Magnetorheological fluids belong to the class of functional materials. It is typical for them to change apparent viscosity when an external magnetic flux is applied. The behaviour of that smart medium is very complex in nature. Therefore, the most challenging task in modelling of devices based on MR fluids is the ability of predicting of the medium's response under various magnetic and pressure excitation. In the case of magnetorheological dampers, the dominant mode of operation of the medium is flow under pressure gradient. The following part of the work is devoted to the topic of mathematical modelling of the MR fluid's flow.

In order to study the mechanics of the MR fluid under the flow mode, an experimental apparatus was designed and fabricated. The apparatus allowed to test an experimental volume of MR fluid being under the flow mode by continuously applied pressure gradient. The experimental volume of fluid of rectangular shape was excited with magnetic flux in perpendicular direction.

This chapter presents at the beginning a review of methods of modelling of MR fluids under the flow mode and introduces the experimental stand with analysis of their magnetic properties. The further part introduces the models used for prediction of the MR fluid behaviour in the experiments and gives verification of the measured results.

2.2 Review of the methods of modelling

The problem of modelling of the magnetorheological fluids' behaviour was attempted to be solved by means of several methods. The primary papers devoted to that topic focused on the phenomenological modelling of complete magnetorheological devices [60]. A significant advantage of these methods was the ability of

prediction of full dynamics of the modelled devices. However, since the methods did not come into analysis of the fluid's behaviour itself, they could not serve as supporting tools for designers.

The second group of the proposed models were based on the analysis of the MR fluid's mechanics in steady conditions [61, 62, 63, 64]. The analysis was based on analogy between behaviours of magnetorheological and electrorheological fluids [61, 65, 66]. The models were based on the Bingham plastic body constitutive relation, which was adapted from classical mechanics of non-Newtonian fluids. This constitutive model of MR fluid behaviour was introducing the yield stress level varying depending on the applied magnetic field intensity. This way of modelling has proved its usefulness in characterisation, and the preliminary scaling of many adaptive devices based on MRF [52, 67, 68, 69]. The Bingham model has a very important advantage: it gives an opportunity of derivation of equations describing the flow of the fluid with analytical solutions. Therefore, the model can serve as well as a tool for prediction of the behaviour of existing MR devices and it can be used as a tool for design purposes. Due to the complexity of the equations, the analytical solutions can be found only after assuming non-inertial character of the medium. Because of this limitation, the Bingham model gives only a possibility of prediction of the MR fluids behaviour in the steady flows.

During nineties the models were continuously tested and researchers noticed that the Bingham model does not respond properly in the range of very low and very high shear rates. The models were continuously improved in order to obtain the closest response of the model to the results of experiments. Examples of effects of these research are: biviscous modelling and Hershell-Bulkley modelling [64, 70]. Biviscous modelling was proposed by Werely [63], who introduced a principle of bilinear constitutive relation describing the fluid. This method intended to model the behaviour of the medium in the range of very low shear rates. The model of Hershell-Bulkley was introduced in order to predict the behaviour of the MR fluid in the range of high shear rates and reflect the phenomenon of shear thickening and shear thinning of the fluids. However, the model is identifiable only by means of empirical search, which limits its applicability to the task of modelling of the existing devices on the basis of measurements.

The discussion presented above gives a strong recommendation for Bingham model which is a useful tool for analytical modelling of the existing devices and it can serve as tool for designers, on the preliminary stage of the design process.

In accordance to the presented discussion, in this research a special attention will be given to the modelling and initial sizing of the MR devices by the Bingham model.

Another important problem that is rarely considered is characterisation of the magnetic field perpendicular to the fluid gap. In many of the investigations described above, the magnetic flux density and hence the yield stress is assumed

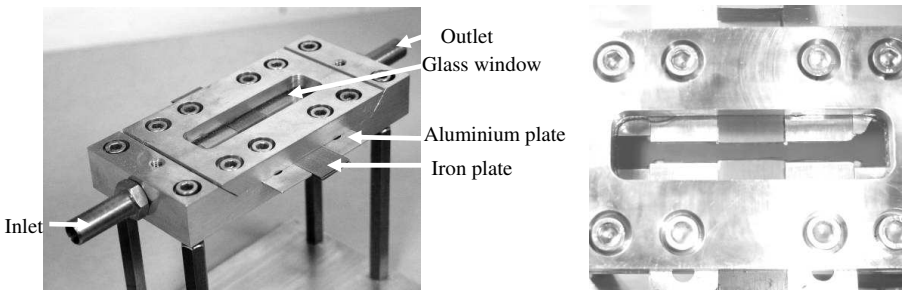

Figure 2.1: Overview of the experimental valve.

to be constant across the entire flow area. This assumption is valid in a wide class of devices that have the orifice gap small in comparison to the volume of magnetic circuit material, but there may be instances when the assumption is not valid, e.g. the seismic protection devices where a gel is utilised as the carrier fluid and, therefore, the orifice is larger in accordance to the higher base viscosity of the MRF.

Transverse variation of the magnetic field in the gap was reported as the general analytical issue that can influence the character of flow in MR fluid ducts [52]. The authors developed an axisymmetric model that accounted for a variable yield stress by using an inverse power law. This was compared to a simplified model that assumed a constant yield stress, although the simplified model was found to be adequate for that problem.

In summary, the distribution of the magnetic field intensity is not a widely considered problem. Nevertheless, it is an important issue to be analysed in the case of potential devices where the fluidic gap must be designed to be larger, and then the predictions of the ER/MR fluid behaviour require a magnetic field intensity analysis perpendicular to the valve gap. Such a case is analysed both numerically and experimentally in the last part of this chapter.

2.3 Experimental setup

In order to perform the research on the MRF in the flow mode, an experimental model of a magnetic valve was designed and fabricated (Fig. 2.1(a)). The magnetic valve was designed in the way to enable the following measurements: determination of pressure drop variation as a function of the magnetic field intensity and visualisation of the MR fluid in the flow mode.

The experimental volume of the MR flow channel that was activated by the magnetic field was a rectangular block as shown in Fig. 2.2. The fluid in the channel was excited with the magnetic field lines along the Y axis and the fluid was under a pressure gradient along the X axis (Fig. 2.2). The dimensions of

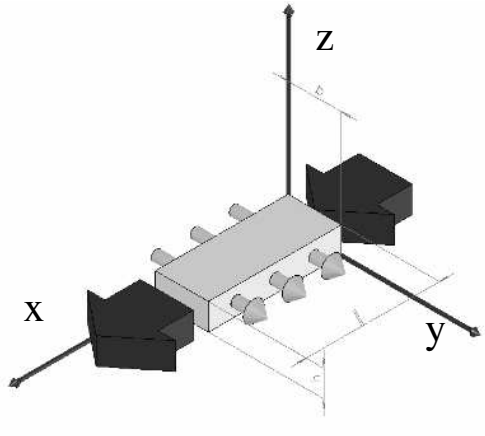

Figure 2.2: Geometrical representation of the active volume of the MR fluid, round arrows – magnetic induction, rectangular arrows – pressure gradient.

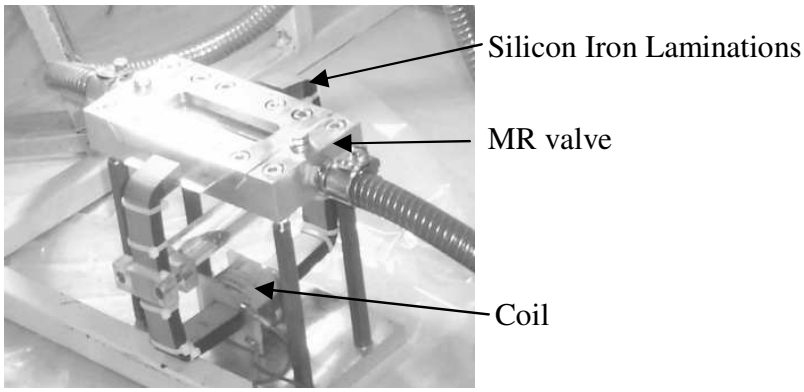

Figure 2.3: Assembled experimental stand

the channel were: 1 mm height, 3 mm width and the magnetically active length was 20 mm. Fig. 2.1(b) presents the top view of the experimental valve. The top surface of the device is made of glass in order to enable the MR fluid flow observations. The dark grey area visible in Fig. 2.1(b) represents the MR fluid. The channels side borders are six plates. Four of them are aluminum plates (having non-magnetic properties) and two of them are made of silicon iron and play the role of magnetic poles, connected to the magnetic circuit (Fig. 2.3).

The magnetic circuit was designed in a way to provide a sufficient magnetic field to excite the volume of MR fluid across the orifice. The magnetic circuit consisted of a magnetic core made of silicon iron and a coil (Fig. 2.3). The main part of the core had a cross-section 20 mm x 10 mm (width x height) and for the part, which was connected to the experimental channel, the dimensions were reduced to 20 mm x 1 mm (width x height). The coil had 140 turns and was positioned symmetrically with respect to the gap in the magnetic circuit. The

magnetic excitation system was able to generate B = 0.5T between the poles. The symmetrical positioning of the coil allowed the generation of an exactly equal level of flux density on both surfaces of the poles.

The pressure gradient was generated by a piston pump, which could produce a maximum level of 2MPa. The resulting flow rates tested were up to $2.5 \cdot 10^{-5}$ $\mathrm{m^3 s^{-1}}$. The experiments included the following measurements: pressure signal on the inlet and outlet of the flow channel, displacement of the pumps piston, and the current applied to the coil. This was sufficient to enable the quasi-steady pressure/flow rate characteristic of the valve to be calculated.

2.4 Constitutive relation

In accordance to the discussion presented in the previous section, the Bingham model of the MR fluid behaviour was chosen for further analysis. The MR fluid flow was modelled by means of a non-Newtonian constitutive relation in order to utilise adaptive properties of the MR damper. The constitutive relation describing the plastic bodies is given by Eq. (2.1). The relation introduces a parameter, which describes the dynamic yield stress τ_0 of the fluid, which defines a shear stress level (yield stress) below which the flow of MR fluid is not developed. The yield stress level τ_0 varies depending on the magnetic flux intensity of the MR fluid's excitation. The relation is formulated as follows:

$$\tau = \tau_0 + \mu_p \frac{\mathrm{d}u}{\mathrm{d}y} \,. \tag{2.1}$$

Here τ_0 is dynamic yield stress, μ_p is base viscosity of the fluid and $\frac{\mathrm{d}u}{\mathrm{d}y}$ is the 1D shear rate. The Bingham model was widely used for description of the MR fluid behaviour [66].

In the present work the MR fluid was modelled in two modes of operation. At first the damper was assumed to be a passive device. This assumption was made for the operation of the damper with zero magnetic field applied. The objective for this analysis was determination of the value of the base viscosity μ_p in an intentionally designed experiment. In the case of passive operation of the MR fluid the yield stress τ_0 was assumed to be equal zero, which leads to the following form of the constitutive relation:

$$\tau = \mu_p \frac{\mathrm{d}u}{\mathrm{d}y} \,, \tag{2.2}$$

in which μ_p is the base viscosity.

The relation Eq. (2.2) is the constitutive relation for Newtonian fluids [71], expressing proportional relation between shear stress τ and shear rates $\dot{\gamma}$. Fig. 2.4 depicts a comparison between rheological characteristics of the Newtonian and non-Newtonian fluids.

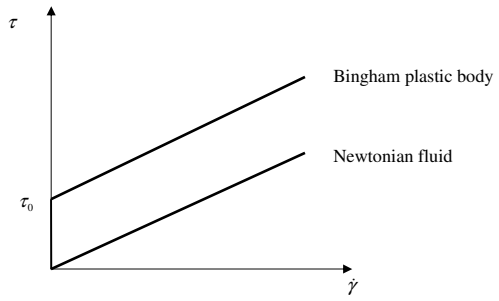

Figure 2.4: Illustration of constitutive relations for Newtonian fluids and Bingham plastic bodies.

The modelling of the MR fluid with the Bingham model is based on the assumption that the magnetorheological fluid under excitation of magnetic flux behaves like a plastic body and can be described by the relation Eq. (2.1). Depending on the intensity of the magnetic excitation, the MR fluid exhibits the higher yield stress described by τ_0.

2.5 MR fluid's flow in passive mode of operation

The passive mode of operation in the case of an MR fluid is behaviour of the medium when the external magnetic field is not applied. Assumption here is that the behaviour of the fluid in such conditions can be described by means of relations derived for an incompressible Newtonian fluid. The constitutive relation of Newtonian fluids was defined in Eq. (2.2).

2.5.1 Flow of a viscous fluid - governing equations

The flow of an incompressible Newtonian fluid can be expressed by the Navier-Stokes equations [72] as:

$$\rho \frac{D\underline{u}}{Dt} = \rho \underline{g} - \nabla p + \eta \nabla^2 \underline{u}, \tag{2.3}$$

in which: $\frac{D\underline{u}}{Dt}$ - material derivative, ρ - fluid density, $\underline{u}$ - fluid velocity vector, $\underline{g}$ - gravity, p - fluid pressure, η - viscosity of the fluid.

By reduction of the expressions connected with z direction, one can obtain fluid flow equations for a 2D analysis in the form of components in the Cartesian coordinate system:

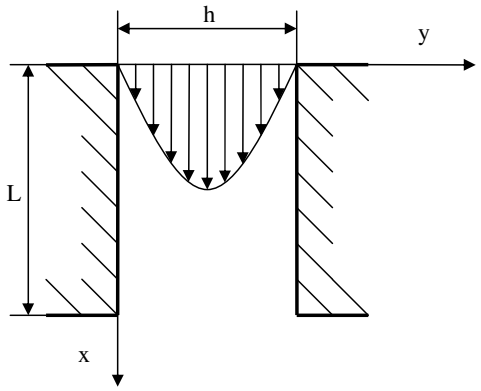

Figure 2.5: Illustration of the Newtonian fluid flow case.

$$\begin{aligned}
\rho\left(\frac{\partial u}{\partial t}+u\frac{\partial u}{\partial x}+v\frac{\partial u}{\partial y}\right) &= \rho g_x-\frac{\partial p}{\partial x}+\eta\left(\frac{\partial^2 u}{\partial x^2}+\frac{\partial^2 u}{\partial y^2}\right),\\
\rho\left(\frac{\partial v}{\partial t}+u\frac{\partial v}{\partial x}+v\frac{\partial v}{\partial y}\right) &= \rho g_y-\frac{\partial p}{\partial y}+\eta\left(\frac{\partial^2 v}{\partial x^2}+\frac{\partial^2 v}{\partial y^2}\right).
\end{aligned} \tag{2.4}$$

Exact reformulation of the equation can be found in Appendix A.

2.5.2 Flow of a viscous fluid between parallel plates

Let us consider the Newtonian fluid flow between two parallel plates that are fixed in a vertical position presented schematically in Fig. 2.2. The fluid flow will be developed by a pressure gradient in the flow direction parallel to x axis. Let us assume that the flow is two-dimensional, steady, uniform and analysed in the (x, y) coordinate system as presented in Fig. 2.5. In the analysis the fluid was assumed to be incompressible.

An analysis of the assumptions of the case under consideration leads to the following:

– Steady flow	$\frac{\partial u}{\partial t}=0,$	
– Uniform flow	$\frac{\partial u}{\partial x}=0,$	$\frac{\partial^2 u}{\partial x^2}=0,$
– No flow in Y direction	$v=0,$	
– Gravitation	$g_x=0,$	$g_y=0,$
– Pressure gradient	$\frac{\partial p}{\partial x}<0.$	

In accordance with the above expressions, the flow equation Eq. (2.4) can be reduced to:

$$0 = -\frac{\partial p}{\partial x} + \mu \frac{\partial^2 u}{\partial y^2}\,. \tag{2.5}$$

Since it was assumed that the pressure gradient varies linearly along the length of the orifice, it can be formulated as:

$$\frac{\partial p}{\partial x} = \frac{\mathrm{d}p}{\mathrm{d}x}\,. \tag{2.6}$$

When we analyse the case present in the experiment, then: $dx = L$ - length of the orifice and $dp = \Delta P$ - pressure drop across the orifice.

Thus the equation of flow for the considered case is:

$$\frac{\Delta P}{L} = \mu \frac{\partial^2 u}{\partial y^2}\,. \tag{2.7}$$

Flow rate for the case of parallel plates flow

Double integration of Eq. (2.7) enables us to obtain the velocity profile between parallel plates:

$$u = \frac{1}{2\mu}\frac{\Delta P}{L}y^2 + \frac{A}{\mu}y + B, \tag{2.8}$$

in which A and B are constants of integration. In the considered case of flow through a duct, the boundary conditions are:

$$u(y)|_{y=0} = 0,$$
$$u(y)|_{y=a} = 0,$$

in which a is the distance between the considered plates.

Substitution of the boundary conditions enables us to evaluate the constants of integration:

$$B = 0,$$
$$A = -\frac{1}{2}\frac{\mathrm{d}P}{\mathrm{d}L}\,a.$$

Eliminating A and B results in:

$$u = \frac{1}{2\mu}\frac{\Delta P}{L}(y^2 - ay). \tag{2.9}$$

The discharge past a fixed cross-section is obtained by integration of Eq. (2.9) with respect to y:

$$Q = h \int_0^a u \, dy = -h \frac{1}{12\mu} \frac{\Delta P}{L} a^3, \tag{2.10}$$

in which h is depth of the analysed orifice that has a rectangular cross-section.

2.6 MR fluid's flow in active mode

2.6.1 Flow of Bingham plastic body - governing equations

The fluid flow equation was derived from the generalized form of the Navier-Stokes equations [72]. The flow equation for an incompressible, non-Newtonian fluid can be expressed as:

$$\rho \frac{D\underline{u}}{Dt} = \rho \underline{g} + div(\underline{\tau}), \tag{2.11}$$

where: $\frac{D}{Dt}$ - material derivative, ρ - fluid density, $\underline{u}$ - fluid velocity vector, g - gravity, $\underline{\tau}$ - general stresses on the fluid element.

And by reduction of the expressions connected to z direction one can obtain fluid flow equations for a 2D analysis:

$$\begin{aligned} \rho \left(\frac{\partial u}{\partial t} + u \frac{\partial u}{\partial x} + v \frac{\partial u}{\partial y} \right) &= \rho g_x - \frac{\partial p}{\partial x} - K \frac{\partial^2 u}{\partial x^2} + \frac{\partial \tau_{yx}}{\partial y}, \\ \rho \left(\frac{\partial v}{\partial t} + u \frac{\partial v}{\partial x} + v \frac{\partial v}{\partial y} \right) &= \rho g_y - \frac{\partial p}{\partial y} + \frac{\partial \tau_{xy}}{\partial x} - K \frac{\partial^2 v}{\partial y^2}. \end{aligned} \tag{2.12}$$

Exact reformulation of the equation can be found in Appendix B.

2.6.2 Flow of a Bingham plastic body between parallel plates

Let us consider a Bingham plastic body flow between two parallel plates that are fixed in a vertical position. The object is placed in a non-gravitational field. Let us assume that the flow is two-dimensional, steady, uniform and that it is analysed in a 2D coordinate system. The considered fluid is assumed to be incompressible. The flow is developed parallel to the x axis and positive and is developed by a pressure gradient between both ends of the considered duct.

The case of 2D flow between parallel plates is schematically presented in Fig. 2.6.

The flow of the MR fluid can be successfully modelled by means of Bingham plastic body constitutive law [66, 61]. The equations of the non-viscous fluid flow between parallel plates can be expressed as Eq. (2.12):

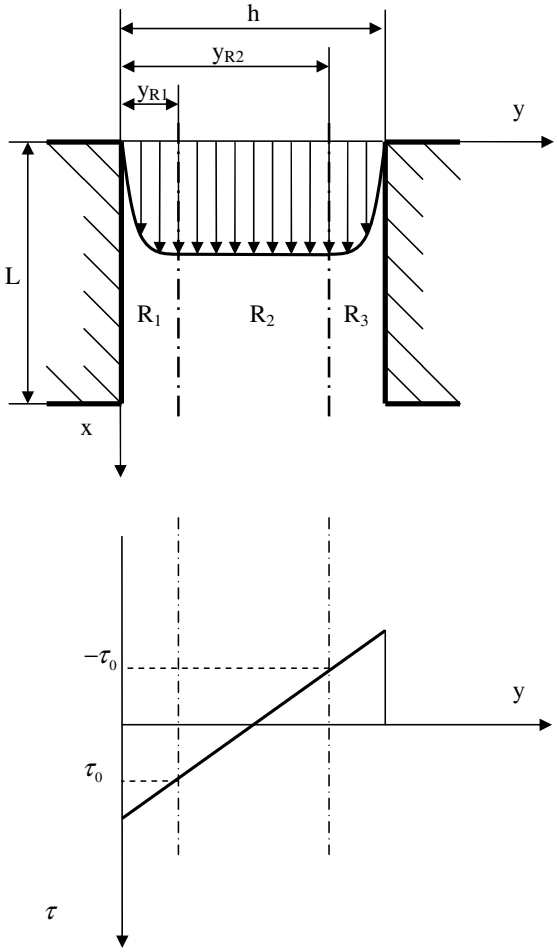

Figure 2.6: Illustration of the MR fluid flow case.

$$\begin{aligned} \rho\left(\frac{\partial u}{\partial t}+u\frac{\partial u}{\partial x}+v\frac{\partial u}{\partial y}\right) &= \rho g_x-\frac{\partial p}{\partial x}-K\frac{\partial^2 u}{\partial x^2}+\frac{\partial \tau_{yx}}{\partial y}\,, \\ \rho\left(\frac{\partial v}{\partial t}+u\frac{\partial v}{\partial x}+v\frac{\partial v}{\partial y}\right) &= \rho g_y-\frac{\partial p}{\partial y}+\frac{\partial \tau_{xy}}{\partial x}-K\frac{\partial^2 v}{\partial y^2}\,. \end{aligned} \tag{2.13}$$

The considered flow is analysed in a two-directional Cartesian coordinate system, velocity vector is $\underline{u}=(u,v)$.

For the flow analysis, the following set of assumptions is going to be taken into account:

– Steady flow	$\frac{\partial u}{\partial t} = 0,$
– Uniform flow	$\frac{\partial u}{\partial x} = 0,$
– Gravitation	$g_x = 0, \quad g_y = 0,$
– Fluid is incompressible	$\frac{\partial^2 u}{\partial x^2} = 0,$
– No flow in Y direction	$v = 0.$

After taking the assumptions into account the flow equation reduces to the following form:

$$\begin{aligned} 0 &= -\frac{\partial p}{\partial x} + \frac{\partial \tau_{yx}}{\partial y}\,, \\ 0 &= -\frac{\partial p}{\partial y}\,. \end{aligned} \tag{2.14}$$

It can be seen that the pressure gradient in y direction is zero what is consistent with the assumptions made for the analysis. For further considerations the following equation is valid:

$$\frac{\partial p}{\partial x} = \frac{\partial \tau_{yx}}{\partial y}\,. \tag{2.15}$$

Note that τ_{yx} is the shear stress in direction of the x axis.

Since pressure p depends exclusively on variable x, then the flow equation takes form:

$$\frac{\mathrm{d}p}{\mathrm{d}x} = \frac{\partial \tau_{yx}}{\partial y}\,. \tag{2.16}$$

To solve the flow Eq. (2.16) the constitutive law for Bingham plastic body is introduced:

$$\tau_{yx} = \tau_0 sgn(u) + \mu_p \frac{\mathrm{d}u}{\mathrm{d}y}\,. \tag{2.17}$$

Symbol τ_0 expresses a dynamic yield stress of the Bingham plastic material. When value of the shear stress of the considered material does not exceed the value of $|\tau_0|$, the flow is not developed. When the shear stress τ exceeds the $|\tau_0|$, the material begins to flow and velocity gradient starts to be greater than zero $\frac{\mathrm{d}u}{\mathrm{d}y} > 0$. The flow cross-section is then divided into three regions (Fig. 2.6): R_1, R_2, R_3. The viscous flow takes place in regions: R_1 and R_3, where the shear stress value is greater than τ_0. In the region R_2 the shear stress is lower than τ_0

and the shear rate observed in that region is equal zero $\frac{\mathrm{d}u}{\mathrm{d}y} = 0$. The relative velocity on the borders between the regions is described by function $u'(y)$.

Assuming that the analysed fluid is under the flow conditions $\tau_{yx} > \tau_0$, the constitutive law Eq. (2.17) can be substituted to the flow equation Eq. (2.16):

$$\frac{\mathrm{d}^2 u}{\mathrm{d}y^2} = \frac{1}{\mu_p}\frac{\mathrm{d}p}{\mathrm{d}x} \tag{2.18}$$

and after integration:

$$u_{R_1}(y) = \frac{1}{2\mu_p}\frac{\mathrm{d}p}{\mathrm{d}x}\, y^2 + C_1 y + C_2.$$

In the region R_1 boundary conditions for the flow are: $u_{R_1}(0) = 0$, $u'_{R_1}(y_{R_1}) = 0$, which leads to the following velocity profile:

$$u_{R_1}(y) = \frac{1}{2\mu_p}\frac{\mathrm{d}p}{\mathrm{d}x}\,(y^2 - 2y_{R_1} y). \tag{2.19}$$

In the region R_2 the shear stress is expressed as:

$$\tau_{yx} = \frac{\mathrm{d}p}{\mathrm{d}x}\, y + C_1. \tag{2.20}$$

Boundary conditions for the region are $\tau_{yx}(y_{R_1}) = \tau_0$, $\tau_{yx}(y_{R_2}) = -\tau_0$. Substitution of the conditions into Eq. (2.20) leads to the following system of equations:

$$\begin{cases} \tau_0 = \dfrac{\mathrm{d}p}{\mathrm{d}x}\, y_{R_1} + C_1, \\ -\tau_0 = \dfrac{\mathrm{d}p}{\mathrm{d}x}\, y_{R_2} + C_1. \end{cases} \tag{2.21}$$

Solution of the system is the thickness of the plug flow (R_2) in the duct denoted as δ:

$$y_{R_2} - y_{R_1} = \frac{2\tau_0}{\frac{\mathrm{d}p}{\mathrm{d}x}}, \qquad \delta = y_{R_2} - y_{R_1}.$$

Thus:

$$\delta = \frac{2\tau_0}{\frac{\mathrm{d}p}{\mathrm{d}x}}. \tag{2.22}$$

In the Region 3 (R_3) the shear stress value exceeds τ_0 and then:

$$u_{R_3}(y) = \frac{1}{2\mu_p}\frac{\mathrm{d}p}{\mathrm{d}x}\, y^2 + C_3 y + C_4. \tag{2.23}$$

Boundary conditions for the Region R_3 are $u_{R_3}(h) = 0$, $u'_{R_3}(y_{R_2}) = 0$, thus after substitution to Eq. (2.23) it leads to the velocity profile in the region:

$$u_{R_3}(y) = \frac{1}{2\mu_p}\frac{\mathrm{d}p}{\mathrm{d}x}\left(y^2 - h^2 + 2y_{R_2}(h-y)\right). \tag{2.24}$$

Because there is no flow across the plug flow region, the shear rate is equal zero, the velocity has the same value in whole the region , thus:

$$u_{R_1}(y_{R_1}) = u_{R_3}(y_{R_2}). \tag{2.25}$$

On the basis of Eq. (2.25) the following system of equations can be written:

$$\begin{aligned} y_{R_2} - y_{R_1} &= \delta, \\ y_{R_2} + y_{R_1} &= h, \end{aligned} \tag{2.26}$$

which in the solution leads to:

$$y_{R_1} = \frac{h}{2}\left(1 - \frac{\delta}{h}\right), \tag{2.27}$$

$$y_{R_2} = \frac{h}{2}\left(1 + \frac{\delta}{h}\right). \tag{2.28}$$

The Eq. (2.27) and Eq. (2.28) determine the position of the plug flow area in dependence on the yield stress τ_0 and in reference with the fluid duct dimension h.

For the analysed case we assume a linear drop of the pressure along the orifice. Writing the pressure drop Δp in the length L gives:

$$\frac{\Delta p}{L} = \frac{\mathrm{d}p}{\mathrm{d}x}. \tag{2.29}$$

Finally the velocity profiles in the particular regions can be expressed as:

$$\begin{aligned} u_{R_1}(y) &= \frac{\Delta p}{2\mu_p L}\left(y^2 - (h-\delta)y\right), \\ u_{R_2}(y) &= -\frac{\Delta p}{8\mu_p L}(h-\delta)^2, \\ u_{R_3}(y) &= \frac{\Delta p}{2\mu_p L}\left(y^2 - (h+\delta)y + h\delta\right). \end{aligned} \tag{2.30}$$

Since the fluid is assumed to be incompressible, the total volume flux through the annular orifice is equal to the volume flux displaced by the piston. The volumetric flow rates for the regions are:

$$\begin{aligned} Q_{R_1} &= b\int_0^{y_{R_1}} u_{R_1}(y)dy, \\ Q_{R_2} &= b\int_{y_{R_1}}^{y_{R_2}} u_{R_2}(y)dy, \\ Q_{R_3} &= b\int_{y_{R_2}}^{h} u_{R_3}(y)dy. \end{aligned} \tag{2.31}$$

Here b is the circumference of the middle circle of the annular orifice and is defined as:

$$b = \frac{D_{in} + D_{out}}{2}, \tag{2.32}$$

where D_{in} and D_{out} are respectively the inner and outer circumference of the annular orifice edges. The assumption introduced above makes the analysis not exact since the model was derived for a parallel plate flow case and applied to cylindrical geometry, what is an approximation. However, the experimental verification presented in the further part of the work shows that the approximation gives very good results and in fact does not affect the results of modelling.

Integration of Eq. (2.31) gives the direct formulation of the volumetric flow rate:

$$\begin{aligned} Q_{R_1} &= -\frac{bh^3\Delta p}{24\mu_p L}\left(1-\frac{\delta}{h}\right)^3, \\ Q_{R_2} &= -\frac{bh^3\Delta p}{8\mu_p L}\left(1-\frac{\delta}{h}\right)^2, \frac{\delta}{h} \\ Q_{R_3} &= -\frac{bh^3\Delta p}{24\mu_p L}\left(1-\frac{\delta}{h}\right)^3. \end{aligned} \tag{2.33}$$

In accordance to the assumption of the fluid incompressibility, the equation of continuity can be introduced to represent the total fluid flux:

$$\sum_{i=1}^{3} Q_{R_i} = A_p v_p. \tag{2.34}$$

Note that A_p is the damper piston area, v_p is the damper's shaft translational velocity. Substitution of Eq. (2.33) into Eq. (2.34) enables us to solve it for Δp in relation to the piston's velocity v_p.

Thus, the hydraulic resistance transmitted on the damper shaft F_h can be denoted as:

$$F_h = -\Delta p A_p, \tag{2.35}$$

which allows to implement this model into a more extended analysis of systems with MR dampers.

2.7 Influence of magnetic flux variations within the MR fluid's duct

2.7.1 Explanation of the phenomenon

This section presents an example where there is a significant magnetic flux density variation across the valve gap of magnetorheological devices. Consequently, the MR fluid yield stress distribution cannot be assumed as constant in numerical modelling. In this section, conventional MR fluid flow models are updated to account for quadratic yield stress distributions. The updated model is validated experimentally on a flow mode test rig that was designed for parallel flat plates flow. In general, it is shown that the effect of the yield stress variation is significant, and simplified models cannot predict the behaviour accurately. The presented model is shown to improve the numerical predictions of the experimental response.

In most papers devoted to the analysis of steady flow in MR fluids, authors assume invariable distribution of the magnetic flux across the valve gap [67, 65]. The assumption is valid for a significant number of the MR devices, in which the dimension of the gap is small and the field intensity is high. However, in the case when the flux density variation is significant and cannot be assumed as constant, conventional models will not predict the behavior accurately. Such cases are more likely to occur in devices where the gap size is large. The conventional models of quasi-steady MR fluid flow are derived on the basis of the Bingham plastic flow equation. Here, the yield stress in the fluid is often assumed as constant across the valve gap. This is shown schematically in Fig. 2.7, which depicts MR fluid flow between parallel flat plates of length l, and separated by distance h. The flow is excited by a pressure drop ΔP and magnetic flux ϕ. Assuming a one-dimensional steady flow and neglecting gravitational and compressibility effects, the following governing equation can be readily derived [61]:

$$\frac{\Delta P}{l} = \frac{\mathrm{d}\tau}{\mathrm{d}y}\,. \tag{2.36}$$

Here, τ is the shear stress, and y is the vertical displacement coordinate across the gap. As shown in Fig. 2.7, this implies a linear shear stress distribution, which is equal to zero at the centre of the channel. Due to the yield stress in the fluid, this leads to the development of a plug where the shear stress does not exceed this value. Outside of the plug, the fluid behaves in a viscous manner. In this section, the most important modification to the conventional model is the introduction of a variable yield stress across the valve gap. This is shown in Fig. 2.7(b), which

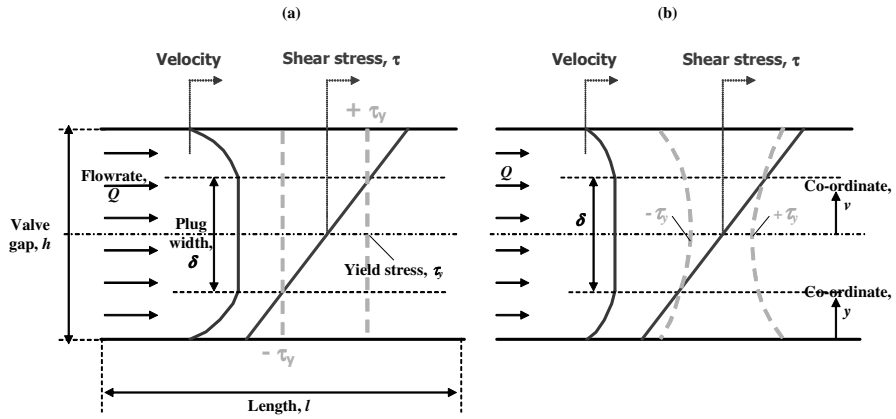

Figure 2.7: Schematic diagrams of MR fluid flow between parallel flat plates. (a) Constant yield stress distribution across the gap and (b) quadratic yield distribution across the gap.

indicates a quadratic distribution of the yield stress τ_y. This variation in τ_y can significantly reduce the flow rate for a given pressure drop. With reference to Fig. 2.7(b), this is because the difference between the shear and yield stress, and hence the strain rate, is lower. Consequently, the aim of this section is to compare conventional and modified MR flow models with an experimental test rig that has notable variations in yield stress.

2.7.2 Magnetic analysis

A finite element model of the magnetic circuit described in Section 2.3 was developed. This was built using FEMM [73] and the corresponding model is shown in Fig. 2.8. This is a planar model, which accounts for the fill factor of the steel laminations, and the flux leakage into the surrounding air. To first validate the model, the flux density in the centre of the fluid passage was measured using a Tesla meter. These measurements were obtained in air as it is not possible to place the Tesla meter's probe in the MR fluid once the device is assembled and sealed. The fluid gap in the model (see Fig. 2.8) was then substituted with an air gap so that the predicted flux density could be compared with the experimental readings. The results of this validation exercise are shown in Fig. 2.9, which compares the modelled and experimental flux density values for a range of currents. In general, the correlation between the model and experiment is good thus validating the FE model. There is some fluctuation in the experimental measurements although this may be attributed to the difficulties in positioning the Tesla meter's probe.

The next stage was to use this validated model to predict the flux density in the MR fluid. Here, the magnetic characteristics of Fraunhofers AD275 MR

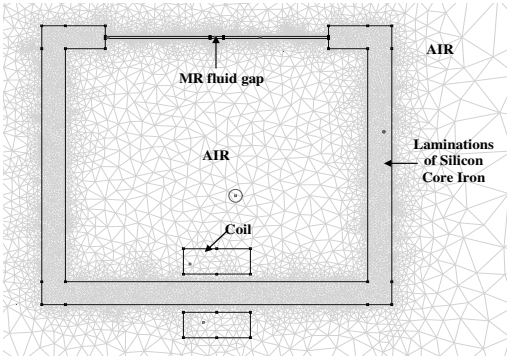

Figure 2.8: Finite element model of the magnetic circuit.

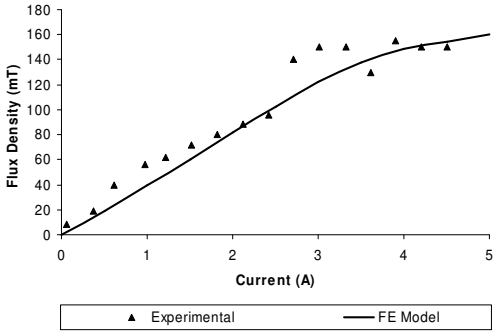

Figure 2.9: Experimental and theoretical flux density values in air.

fluid [74] (i.e. the magnetic flux density versus magnetic field strength curve) was used to model the fluid passage in the FEA. Fig. 2.10(a) shows the resulting flux density distribution, where the distance corresponds to the co-ordinate y in Fig. 2.7(b). Clearly, the quadratic nature of this response is fairly significant. The corresponding absolute yield stress distribution is shown in Fig. 2.10(b), which was calculated using the fluid manufacturers yield stress versus flux density data [74]. This response can be modelled using the following quadratic formula:

$$\tau_{yx} = ay^2 + by + c, \tag{2.37}$$

where a, b and c are fitting constants, which are given in Tab. 2.1 for the responses shown in Fig. 2.10(b). In the next section, MR fluid flow models are developed for the case where the MR fluid yield stress is assumed constant, and for the case where a quadratic yield stress distribution is assumed.

2.7.3 Derivation of the equation

In the following analysis the flow of MR fluid between parallel plates is discussed. There were assumed the following assumptions for the flow: laminar, steady,

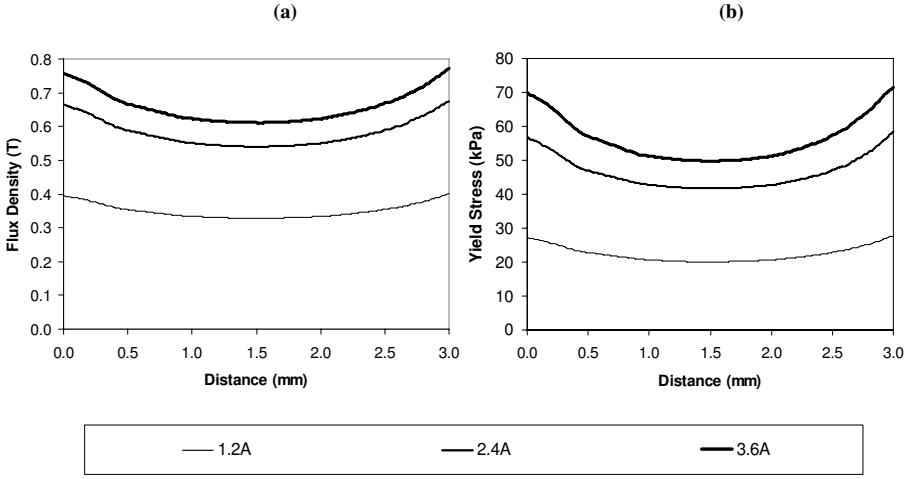

Figure 2.10: Predicted flux density and yield stress distributions across the valve gap. (a) Flux density and (b) yield stress.

Current (A)	Parameter a	Parameter b	Parameter c
1.2	3225436.0	-9689.0	27.2
2.4	6767665.4	-20314.0	56.3
3.6	9233561.7	-27721.5	69.8

Table 2.1: Constants for the quadratic yield stress equations.

uniform flow and incompressibility of the fluid. The following derivation takes advantage of the fact that the distribution of the magnetic flux intensity of the considered case is symmetrical in relation to the central axis of the experimental channel.

Then the flow of the fluid can be described as follows:

$$\frac{\partial p}{\partial x} = \frac{\partial \tau_{yx}}{\partial y} \,. \tag{2.38}$$

Since the flow is considered to be developed exclusively in the direction of x axis, the Eq. (2.38) will take form:

$$\frac{\mathrm{d}p}{\mathrm{d}x} = \frac{\partial \tau_{yx}}{\partial y} \,. \tag{2.39}$$

The flow of the fluid is described by the following constitutive relation:

$$\tau_{yx} = \tau_0(y, B) + \mu_p \frac{\mathrm{d}u}{\mathrm{d}y} \,. \tag{2.40}$$

The key point of the presented analysis is incorporation of the non linear characteristic of the yield stress distribution across the flow path of the fluid. The

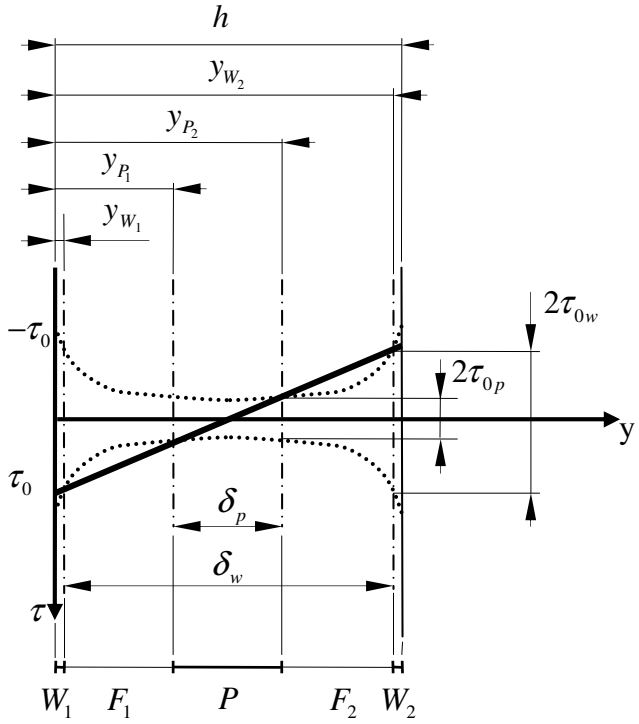

Figure 2.11: An example of quadratic field distribution between the magnetic poles.

yield stress $\tau_0(y, B)$ is non-uniformly distributed across the orifice and dependent on local magnetic field intensity and position between the magnetic poles (in this analysis it is assumed that the poles are plates).

As it is shown in the Fig. 2.11, the flow of the fluid is divided into 5 regions. The behaviour of the fluid in the particular regions depend on the relation between the actual shear rate in the fluid and the local value of the yield stress. A case where there is a significant fluctuation of the magnetic field intensity is shown in Fig. 2.11. In this case the shear stress exceeds the value of yield stress in the fluid in regions denoted by letters F_1 and F_2. Then the whole area of flow is divided into 5 regions in which the fluid exhibits various behaviours:

- W_1 and W_2 - $\tau_{yx} < \tau_0(y, B)$ - no flow region in the area next to the wall $\left(\frac{\mathrm{d}u}{\mathrm{d}y} = 0\right)$,
- P - plug flow region - $\tau_{yx} < \tau_0(y, B)$, $\left(\frac{\mathrm{d}u}{\mathrm{d}y} = 0\right)$,
- F_1 and F_2 - viscous flow regions - $\tau > \tau_0(y, B)$, $\left(\frac{\mathrm{d}u}{\mathrm{d}y} > 0\right)$.

The assumption of the quadratic distribution of the yield stress was based on the analysis of the magnetic flux distribution between the poles in the experiment. The yield stress depends proportionally on the magnetic field intensity and then it can be assumed to have similar character to the magnetic flux lines.

Analysis of flow in regions F_1 and F_2

It was assumed that in regions F_1 and F_2 the analysed fluid does exhibit the flow phenomenon as the developed shear stress exceeds the level of the yield stress value: $\tau_{yx} > \tau_0(B, y)$.

In the case when the analysis is devoted to the regions with developed flow, the flow can be described as:

$$\frac{\mathrm{d}^2 u}{\mathrm{d}y^2} = \frac{1}{\mu_p}\frac{\mathrm{d}p}{\mathrm{d}x}\,. \tag{2.41}$$

Double integration of the Eq. (2.41) leads to the following expression for velocity in the region F_1:

$$u_{F1}(y) = \frac{1}{2\mu_p}\frac{\mathrm{d}p}{\mathrm{d}x}\,y^2 + C_1 y + C_2. \tag{2.42}$$

In the analysed region F_1, the boundary conditions are defined as follows: $u_{F_1}(y_{W_1}) = 0$, $u'_{F_1}(y_{P_1}) = 0$ where $u'_{F_1}(y)$ describes the relative velocity on the borders between regions F_1 and P.

In the region F_2 the expression describing the velocity of the fluid can be written as follows:

$$u_{F_2}(y) = \frac{1}{2\mu_p}\frac{\mathrm{d}p}{\mathrm{d}x}\,y^2 + C_3 y + C_4 \tag{2.43}$$

and the boundary conditions for the region F_2 are: $u_{F_2}(y_{W_2}) = 0$, $u'_{F_2}(y_{P_2}) = 0$ where $u'_{F_2}(y)$ describes the relative velocity on the borders between regions F_2 and P.

Substitution of the relative boundary conditions to the Eq. (2.42) and Eq. (2.43) leads to the following solutions:

$$u_{F_1}(y) = \frac{1}{2\mu_p}\frac{\mathrm{d}p}{\mathrm{d}x}\left(y^2 - y_{W_1}^2 + 2y_{P_1}(y_{W_1} - y)\right) \tag{2.44}$$

and

$$u_{F_2}(y) = \frac{1}{2\mu_p}\frac{\mathrm{d}p}{\mathrm{d}x}\left(y^2 - y_{W_2}^2 + 2y_{P_2}(y_{W_2} - y)\right), \tag{2.45}$$

where $u_{F_1}(y)$ is velocity profile in region F_1 and $u_{F_2}(y)$ is velocity profile in region F_2.

Analysis of flow in regions: W_1, W_2 and P

As the shear stress in the analysed case does not exceed the value of yield stress in regions W_1, W_2 and P, the flow is assumed to be not developed in these areas.

The shear stress can be described as follows:

$$\tau_{yx}(y) = \frac{\mathrm{d}p}{\mathrm{d}x}\, y + C_5. \tag{2.46}$$

Boundary conditions for the shear stress in the regions W_1 and W_2 can be formulated as follows:

$$\tau_{yx}(y_{W_2}) = -\tau_{ow},$$
$$\tau_{yx}(y_{W_1}) = \tau_{ow}.$$

Boundary conditions for the plug flow region P can be formulated as:

$$\tau_{yx}(y_{P_2}) = -\tau_{op},$$
$$\tau_{yx}(y_{P_1}) = \tau_{op}.$$

Then the following systems of equations can be formulated:

$$\begin{cases} \tau_{ow} = \dfrac{\mathrm{d}p}{\mathrm{d}x}\, y_{W_1} + C_5, \\ -\tau_{ow} = \dfrac{\mathrm{d}p}{\mathrm{d}x}\, y_{W_2} + C_5 \end{cases} \tag{2.47}$$

and

$$\begin{cases} \tau_{op} = \dfrac{\mathrm{d}p}{\mathrm{d}x}\, y_{P_1} + C_5, \\ -\tau_{op} = \dfrac{\mathrm{d}p}{\mathrm{d}x}\, y_{P_2} + C_5. \end{cases} \tag{2.48}$$

Solution of the equation formulated above leads to:

$$y_{W_2} - y_{W_1} = \frac{2\tau_{ow}}{\frac{dp}{dx}} = \delta_w, \tag{2.49}$$

$$y_{P_2} - y_{P_1} = \frac{2\tau_{op}}{\frac{dp}{dx}} = \delta_p, \tag{2.50}$$

where δ_w is the normalised width of the flow region and δ_p is the normalised width of the plug flow region.

As there is no flow developed in the regions W_1 and W_2, the velocity conditions can be formulated:

$$\begin{aligned} u_{W_1}(0) &= 0, \\ u_{W_1}(y_{W_1}) &= 0, \\ u_{W_2}(y_{W_2}) &= 0, \\ u_{W_2}(h) &= 0, \end{aligned} \tag{2.51}$$

where h is width of the distance between the border plates.

Since the shear stress value within the plug flow does not exceed the yield stress, the velocity in the area is equal on the whole width:

$$u_P(y_{P_1}) = u_P(y_{P_2}). \tag{2.52}$$

The geometrical dimensions of the analysed case of flow can be calculated from the following systems of equations:

$$\begin{cases} y_{P_1} + y_{P_2} = h, \\ y_{P_2} - y_{P_1} = \delta_p \end{cases} \tag{2.53}$$

and

$$\begin{cases} y_{W_1} + y_{W_2} = h, \\ y_{W_2} - y_{W_1} = \delta_w, \end{cases} \tag{2.54}$$

which after solution lead to the following results:

$$\begin{cases} y_{P_1} = \dfrac{h}{2}\left(1 - \dfrac{\delta_p}{h}\right), \\ y_{P_2} = \dfrac{h}{2}\left(1 + \dfrac{\delta_p}{h}\right) \end{cases} \tag{2.55}$$

and

$$\begin{cases} y_{W_1} = \dfrac{h}{2}\left(1 - \dfrac{\delta_w}{h}\right), \\ y_{W_2} = \dfrac{h}{2}\left(1 + \dfrac{\delta_w}{h}\right). \end{cases} \tag{2.56}$$

The relations presented above enable us to predict the geometry of flow regions in the analysed case.

The last value to be determined is the velocity of the plug flow which can be formulated as:

$$u_p(y) = u_{F_1}(y_{P_1}) = u_{F_2}(y_{P_2}), \tag{2.57}$$

which leads to the following relation:

$$u_p = \frac{1}{2\mu_p}\frac{\mathrm{d}p}{\mathrm{d}x}\left(y_{P_1}^2 - y_{W_1}^2 + 2y_{P_1}(y_{W_1} - y_{P_1})\right). \tag{2.58}$$

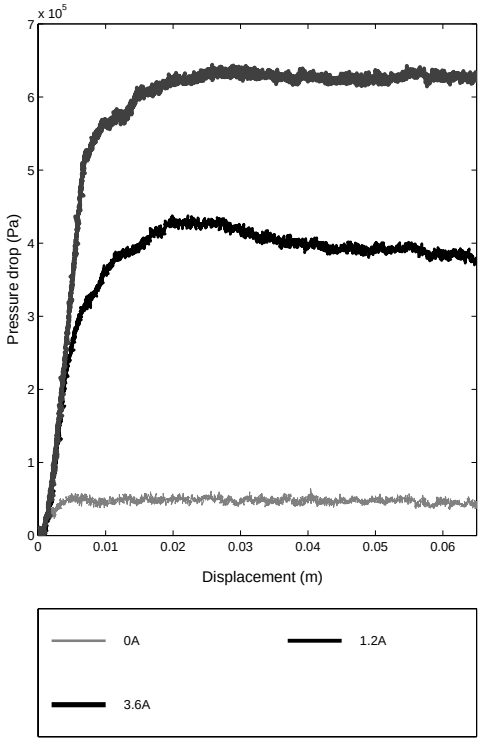

Figure 2.12: Pressure drop versus displacement characteristics of the MR valve.

Relations given by Eq. (2.44), Eq. (2.45) and Eq. (2.58) allow to calculate the resistance of the flow in the analysed MR device in the analogical way to the presented in Eq. (2.31) to Eq. (2.35).

2.7.4 Experimental results

In this section, the experimental quasi-steady pressure/flow rate characteristic of the MR valve is determined. The results are then compared to the quasi-steady flow models that were developed in Section 2.7.3.

A typical experimental result for one constant velocity excitation is shown in Fig. 2.12. This is shown in terms of the pressure drop versus displacement for a range of current excitations. Here, the aim is to achieve a steady-state pressure drop before the end of the damper's stroke. For each current excitation, this is clearly achieved after about 40mm of displacement. The mean pressure drop in this steady-state condition is then calculated and plotted against the corresponding steady-state flow rate. This process is then repeated for a range of piston velocities and current excitations in order to generate the experimental quasi-steady pressure/flow-rate curve.

The resulting experimental quasi-steady response is compared to the numeri-

cal models in Fig. 2.13. Fig. 2.13(a) first presents the numerical results obtained using the equation based on Bingham constitutive model, where the yield stress is assumed as constant across the valve gap (Eq. 2.33). The value of yield stress was taken as the mean of each curve shown in Fig. 2.10(b). Also, the viscosity used in the model was 0.7Pas, which provided a good fit with the slope of the zero-field response. This is actually higher than the value indicated by the manufacturers data sheet, where it is possible to extrapolate a value of around 0.2Pas at comparable shear rates [74]. This discrepancy is likely to be caused by the edge effects in the MR device. For example, the model assumes that the parallel flat plates are infinitely wide such that the edge effects are negligible. In the experiment, the width of the MR valve is very small, thus the edge effects will be more significant, which may give rise to a larger apparent viscosity.

As shown in Fig. 2.13(a), the Bingham model fails to accurately predict the experimental response throughout the range of flow rates. It should be noted that at volume flow rates below about $0.4 \cdot 10^{-5}$ $\mathrm{m^3 s^{-1}}$, there is a significant reduction in pressure that appears to converge towards the origin. This is due to leakage paths in the damper and so the low velocity characteristic of the MR valve cannot be accurately measured. However, this leakage does not significantly affect the results at higher velocities. This is because the resistance of the leakage paths will be significantly higher than the MR valve, thus the volume flow rate through them will be negligible. It is therefore reasonable to concentrate on comparing the model with the experiment at flow rates beyond $0.4 \cdot 10^{-5}$ $\mathrm{m^3 s^{-1}}$. Fig. 2.13(b) compares the experiment with the results obtained from the modified equation that accounts for the quadratic yield stress distribution - the solution given in Section 2.7.3. Clearly, the correlation between model and experiment is improved, particularly for higher applied currents. Comparing Fig. 2.13(a) with Fig. 2.13(b), the difference between the modified and the conventional Bingham model is particularly noticeable at higher voltages. Through inspection of Fig. 2.10(a), this is because the range of yield stress values across the channel is greater. In summary, the modified model will yield notable improvements in model accuracy if large variations in yield stress are anticipated.

2.8 Summary of Chapter 2

This chapter has investigated the performance of an MR fluid device that was found to exhibit significant variation of the magnetic flux density and hence the yield stress across the valve gap. In numerical modelling, authors often neglect this effect, although the assumption is usually valid when the valve gap is small. In the present study, the valve gap was fairly large and so, a more complex model that accounted for yield stress variation perpendicular to the valve gap was required.

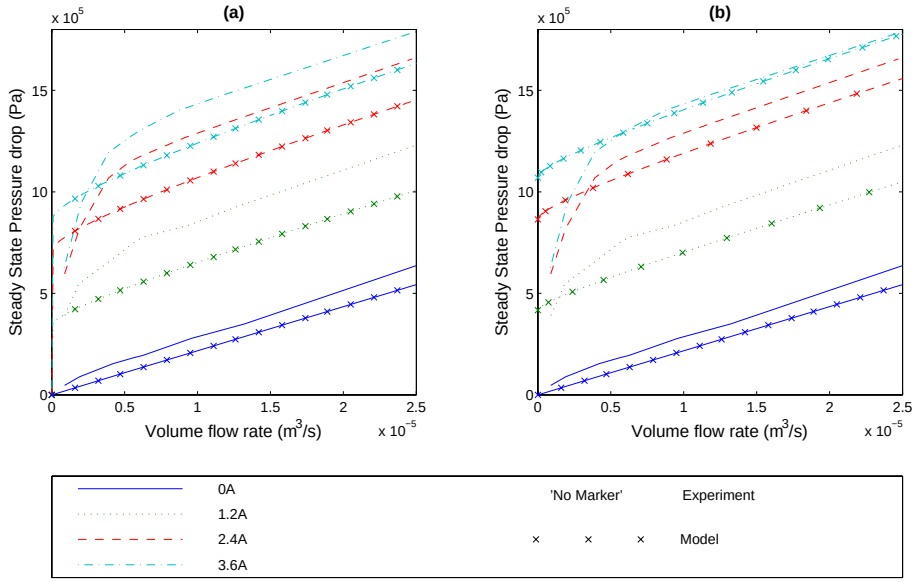

Figure 2.13: Comparison of the experimental quasi-steady damping function with (a) the Bingham equation and (b) the modified model.

To calculate the yield stress distribution, a finite element analysis of the magnetic circuit was performed. The FE model was first validated by using experimental flux density measurements taken in air, and then the yield stress distribution in the fluid was calculated. The FE results indicated a significant quadratic distribution of yield stress across the valve gap.

A numerical model that accounted for this quadratic yield stress behaviour was then derived for quasi-steady Bingham plastic flow between parallel flat plates. This model was compared to quasi-steady measurements taken from the experiment, along with a simplified model that assumes a constant yield stress across the gap.

It was shown that there was a significant influence of the quadratic yield stress variation on the valves pressure/flow-rate response, and that the modified model could better account for the experimental behaviour. The model was derived to predict the flow rate given a specified valve pressure drop. The inverse of this (to predict pressure drop given the flow rate) is significantly more difficult to solve and requires further work.

Chapter 3

Modelling of MRD

3.1 Introduction

During the last decade much attention was given to the problem of modelling of devices based on magnetorheological fluids and prediction of their behaviour. In general, the researchers were divided into two groups: the first one was studying the physics of the fluid and was discussing the problems of designing and scaling of the mentioned devices, and the second group of researchers was focused on utilisation of the unique properties of the MR devices. The key objective for the second group was to develop a control method for a variety of the MR actuators and to overcome their non-linearity [75, 76]. Researchers, who wanted to develop control systems for MR devices required models of the regulated object. Since the MR actuators were treated as only one part of larger controlled systems, then the most important feature of the required models was to predict a phenomenological behaviour of the devices in the presence of a variety of kinematic and electrical excitations [77, 78]. These models are useful for the design of control systems and validation of control strategies but are not devoted to the task of design of the MR actuators geometry.

Then the first group of researchers, who were mentioned at the beginning, focused on methods of prediction of the MR fluid's behaviour inside of the devices [66, 79, 64, 48]. Their analyses were devoted to scaling of the internal parts of the MR devices [61, 80, 81]. Most of the researchers who were studying this problem focused mainly on mechanics of the MR fluid and its interaction with the fluid paths [82]. The effects of the MR fluids reactions were assumed to be the only reactions to be taken into account in modelling of MR devices.

However, the effects that take place in MR devices are multi-physical in nature. Most often the reactions which are provoked by MR fluid are accompanied by significant influence of other forces generated in the devices. For that reason,

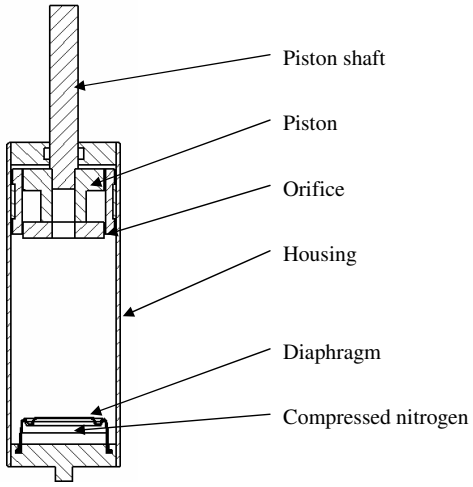

Figure 3.1: Schematic cross-section of the considered MR damper.

in this chapter an MR damper is analysed as an example of device in which the reactions are multi-physical in nature.

This chapter presents analytical modeling of an MR damper behaviour with results of experimental verification. The damper was investigated as an example of a device based on MR fluid. The investigation's objective was validation of the methods of modelling of the MR fluid's flow (presented in Chapter 2) for prediction of an application's behaviour. Moreover, the model of the damper presented in the following chapter has a new character where it was derived directly from the analysis of the device's design. The damper was modelled analytically in a multi-physical routine, which allowed to take into account all types of reactions generated in the damper during its operation. The model was verified versus tests results obtained on experimental stands, which were designed by the author and developed in the laboratories of IPPT PAN.

3.2 Analysis of the MR damper's design

An MR Damper type 1005-3 manufactured by LORD Company was taken under consideration as an example of translational dissipative device based on the MR technology. The damper was analysed from the point of view of its design, in order to identify the main forces contributing to the total force on the piston shaft and in order to formulate their definitions. On the basis of this analysis an analytical model of the complete damper was synthesised. Particular forces contributing to the total force being generated by the damper, were identified in a series of intentionally designed experimental tests. Finally, the model of the damper was verified versus the experimental results obtained under various

regimes of the damper's excitation. The damper was experimentally tested in three series:

1. Under intentionally designed testing regimes in order to identify the parameters of particular contributing forces.

2. Under continuous excitation of constant velocity in order to confirm correctness of the proposed model of complete device.

3. Under impact excitation in order to confirm applicability of the model for dynamic modelling.

A schematic cross-section of the damper is depicted in Fig. 3.1. The main parts are piston with a shaft and cylindrical housing. The magnetic actuator (coil) is placed in the piston and the material of piston plays the role of the magnetic circuit. During operation of the damper, fluid flows between chambers of the damper through an annular orifice in the piston. Properties of the fluid are influenced locally by the magnetic flux when it is pressed through the orifice. In the bottom part of the cylinder housing a diaphragm divides a volume of compressed gas from the fluid. Presence of the pressurised gas chamber increases the initial pressure in the cylinder and therefore ensures avoiding of the cavitation effects in fluid during flow through the orifice.

The dominant force generated by the damper is obviously the damping force being the result of MR fluid's flow resistance via annular orifice positioned in the piston. Except for the damping force, the device generates also some friction and stiffness reactions. It is significant in this case that the damping force is the only one,the value of which depends on velocity of the fluid's flow. The ratio of the hydraulic force value to the rest of the acting forces differs for particular phases of the damper's operation. The most common operation mode of damper is oscillatory motion. Under this excitation the device operates during each period in the range of high velocities and in the range of velocities, their values being close to zero. In the case of phases, when the velocity of the piston is high, the dominant force generated by the damper is the hydraulic one, but in the phases when the sign of velocity is changed (value of velocity is close to zero), the friction and pneumatic forces give a significant contribution to the total force, which can not be neglected when one needs an exact model of the damper's operation.

The elements acting as force contributors in the damper are defined as follows. The hydraulic orifice equipped with a magnetic valve that suppresses the MR fluid flow in a controllable way during operation of the damper. The compressed gas, separated from the MR fluid by a cylindrical diaphragm, acting as a pneumatic spring. The sealing on the piston and the piston shaft which generate the friction force.

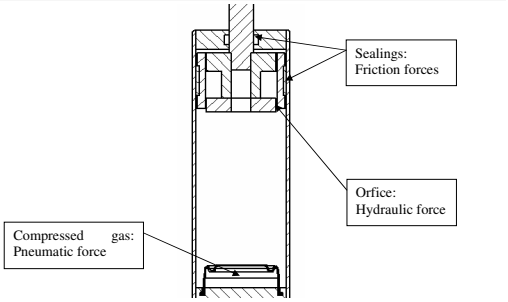

Figure 3.2: Elements responsible for contributing to the shaft force in the MR damper.

The total force generated by the considered MR device during compression mode is interpreted as a combination of three groups of forces acting in the process (Fig. 3.2):

1. Hydraulic force that is a result of fluid pressure's drop between chambers above and underneath the piston.

2. Pneumatic force that is generated due to compression of the gas chamber placed in the lowest part of the housing.

3. Friction force that is generated on the sealing surface of the piston shaft and on the surface between the piston and the inner surface of the cylindrical part of the housing.

3.3 Analytical model of the MR damper

On the basis of the analysis of the forces acting in the damper presented in Sec. 3.2, a 2DoF model of the system was proposed. The model presented in Fig. 3.3 contains a set of simple mechanical elements that reflect all reactions of the damper as defined in Sec. 3.2. The DoFs described by the model are displacement of the piston shaft x_2 and displacement of the diaphragm in the cylinder x_3.

The following types of forces were taken under consideration during formulation of the diagram (Fig. 3.3):

F_f - friction force dependent on $sgn(\dot{x}_2)$. The force is the reaction generated on the contact surfaces between piston shaft and sealing and between the piston and cylinder housing.

$F_{p1}(x_2)$ - pneumatic force dependent on x_2 . The force is generated by the gas spring due to decreasing of the cumulative volume in the housing as an

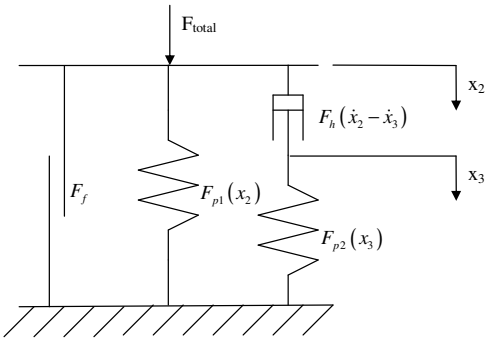

Figure 3.3: Model of the MR damper.

effect of moving the piston shaft inside the cylinder. The effective reduction of the gas volume results in increase of the contribution to the total force.

$F_{p2}(x_3)$ - pneumatic force dependent on relative displacement x_3. The force is generated due to compression of the gas spring by the pressurised fluid above the diaphragm during fast cycles of the damper.

$F_h(\dot{x}_2 - \dot{x}_3)$ - hydraulic force dependent on relative velocity $\dot{x}_2 - \dot{x}_3$. The force is generated due to resistance of the MR fluid flow through the orifice in the piston.

In order to analyse the MR damper, the following set of equations of motion was formulated:

$$\begin{aligned} F_{total} = F_f(sgn(\dot{x}_2)) + F_{p1}(x_2) + F_h(\dot{x}_2 - \dot{x}_3), \\ F_h(\dot{x}_2 - \dot{x}_3) = F_{p2}(x_3). \end{aligned} \tag{3.1}$$

It was assumed for the analysis that the damper is weightless. The model formulated above was identified using results of experiments where the MR damper was excited with constant velocities. For further tests during which the MR damper was excited with an impact loading, another dynamic scheme and set of equations of motion were formulated.

Fig. 3.4 depicts the dynamic scheme of the MR damper on a drop machine. Additionally to the model formulated for the MR damper, an inertial elements: M_1 and M_2 were added. M_1 represents a drop mass used in the experiment. M_2 represents concentrated mass of the MRDs piston head. The force F_r acting between elements M_1 and M_2 is generated by a rubber bumper placed on the impact interface.

Equations of motion for the model are formulated as follows:

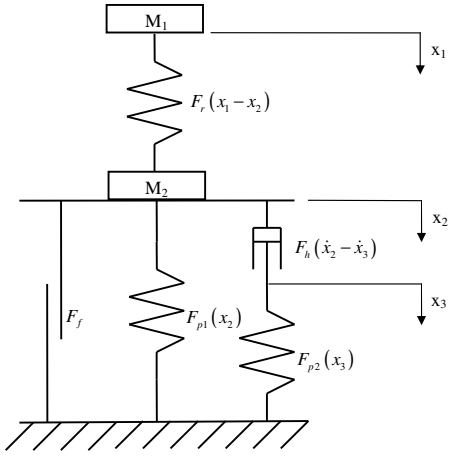

Figure 3.4: Model of the MR damper under impact loading.

$$\begin{aligned} M_1\ddot{x}_1 &= M_1 g - F_r(x_1 - x_2), \\ M_2\ddot{x}_2 &= M_2 g + F_r(x_1 - x_2) - F_h(\dot{x}_2 - \dot{x}_3) - F_{p1}(x_2) - F_f, \\ F_h(\dot{x}_2 - \dot{x}_3) &= F_{p2}(x_3). \end{aligned} \tag{3.2}$$

In order to keep consistency of assignment with the previously formulated model Eq. (3.1) the additional degree of freedom representing motion of the mass M_1 was stated as x_1. All of the contributing forces are formulated in accordance to physical laws for the phenomenon they represent and are presented in the following sections of the work.

3.4 Formulation of pneumatic force F_{p1}

The pneumatic force F_{p1} depicted in Fig. 3.3 represents the force that is generated as an effect of gas compression inside the MR damper's cylinder. The force F_{p1} exclusively depicts the reaction for the reduction of the gas volume inside the cylinder due to motion of the piston shaft inside the cylindrical housing. The exact value of the gas volume reduction is calculated on the basis of the shaft geometry and its position.

Fig. 3.5 represents a schematic cross-section of the MR damper where movement of the piston shaft is denoted with variable x_2, in consistency with the models formulated in Sec. 3.3 . The spring gas was modelled with an isothermal polytropic law of gas compression [17] :

$$pV^n = const. \tag{3.3}$$

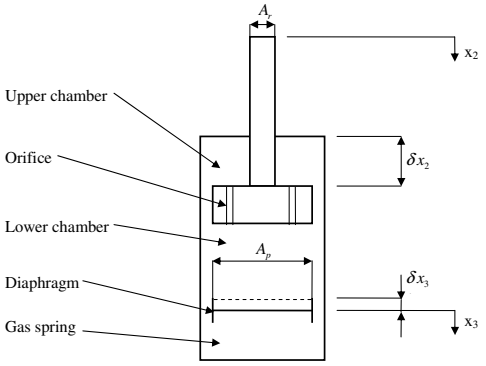

Figure 3.5: Compression scheme of the MR damper.

The force generated by the compressed gas on the piston shaft is caused by the pressure acting on the area that is equal to the cross-section of the piston shaft. The equation of force equilibrium is formulated as follows:

$$F_{p1} = \left(p_1 + \frac{\partial p_1}{\partial x_2} \delta x_2 \right) A_r. \tag{3.4}$$

p_1 is the initial gas pressure in the gas chamber, A_r – area of the piston shaft cross section. When we define:

$$p_{21} = p_1 + \frac{\partial p_1}{\partial x_2} \delta x_2 \tag{3.5}$$

and substitute to Eq. (3.4), then:

$$F_{p1} = p_{21} \cdot A_r. \tag{3.6}$$

Here: p_{21} - actual gas pressure increased as an effect of the volume reduction due to the piston shaft insertion.

On the basis of the assumed gas law Eq. (3.3) one can derive:

$$p_{21} = p_1 \left(\frac{V_1}{V_2} \right)^n = p_1 \left(\frac{V_1}{V_1 - A_r \delta x_2} \right)^n. \tag{3.7}$$

V_1 denotes initial volume of the gas and V_2 is an actual volume of the gas.

Thus, the force generated on the piston shaft equals:

$$F_{p1} = p_1 A_r \left(\frac{V_1}{V_1 - A_r \delta x_2} \right)^n, \tag{3.8}$$

where: F_{p1} - pneumatic force 1, p_1 - intial gas pressure, δx_2 - piston shaft displacement, n - polytropic coefficient.

3.5 Formulation of pneumatic force F_{p2}

During compression mode of the MR damper's operation the fluid is pressed through the orifices in the piston from the lower chamber to the upper chamber. The process provokes a rise of the oil pressure gradient between upper and lower chamber. In the case where velocity of the piston reaches a critical value, the fluid's flow through the orifices is so limited that the pressure of the oil in the lower chamber equalises and starts to exceed the pressure of the gas below the diaphragm. In consequence, the gas starts to be compressed and changes its volume. The movement of the diaphragm between oil and the gas is described in the model depicted in Fig. 3.5 by the variable x_3. The resultant force generated on the piston shaft is denoted F_{p2}. The gas state is defined in a similar way as it was defined in case of pneumatic force F_{p1} (formulated in Eq. (3.8)). The force generated on the piston shaft in this process can be stated as follows:

$$F_{p2} = \left(p_1 + \frac{\partial p_1}{\partial x_3} \delta x_3 \right) A_p. \tag{3.9}$$

When we define:

$$p_{22} = p_1 + \frac{\partial p_1}{\partial x_3} \delta x_3, \tag{3.10}$$

then:

$$F_{p2} = p_{22} A_p, \tag{3.11}$$

where: p_{22} – actual gas pressure increased as an effect of the volume reduction due to the diaphragm motion, A_p – area of the piston cross-section equal to the effective diaphragm area.

On the basis of the assumed gas state law Eq. (3.3) the following relation can be derived as follows:

$$p_{22} = p_1 \left(\frac{V_1}{V_2} \right)^n = p_1 \left(\frac{V_1}{V_1 - A_p \delta x_3} \right)^n, \tag{3.12}$$

thus:

$$F_{p2} = p_1 A_p \left(\frac{V_1}{V_1 - A_p \delta x_3} \right)^n, \tag{3.13}$$

where: F_{p2} - pneumatic force 2, p_1 - initial gas pressure, V_1 - initial gas volume, x_3 - displacement of the diaphragm, n - polytrophic coefficient.

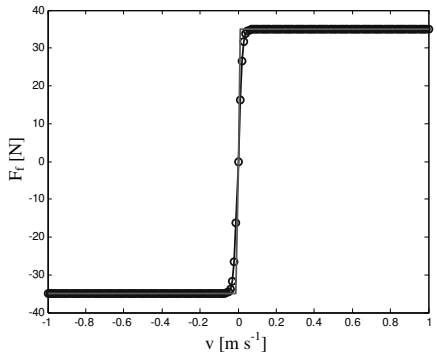

Figure 3.6: Friction force characteristics.

3.6 Formulation of friction force

The friction surfaces that were taken under consideration during analysis of the damper were: surface of contact between the piston shaft and sealing as well as contact surface between the piston and inner cylinder surface. Due to the fact that the damper was assumed to be excited in the axial direction exclusively, the friction forces were decided to be modeled by Coulomb friction law as described in Eq. (3.14) and depicted in Fig. 3.6,

$$F_f = F_{cf} sgn(\dot{x}_1). \tag{3.14}$$

For the purpose of numerical implementation the friction force model Eq. (3.14) was modified and an approximated form of the model was formulated in the following way:

$$F_f = F_{cf} \tanh(s\dot{x}_1), \tag{3.15}$$

noting that F_{cf} - friction force coefficient, $\dot{x}_2$ - velocity of the piston, s - factor determining the model's approximation.

Fig. 3.6 presents two curves, the first of which depicts Coulomb friction (solid line) and the another (circled line) represents the approximation in the form of continuous function formulated in Eq. (3.15).

3.7 Formulation of the hydraulic force

Hydraulic force is generated in the damper because of the fluid flow resistance through the annular orifice in the piston. The hydraulic force measured on the shaft results from the fluid pressure gradient between lower and upper chamber (see Fig. 3.5). The pressure gradient depends on the character of the fluid flow through the orifice. In the considered damper the MR fluid is utilised in order to

obtain a possibility of influencing of the character of the flow and then to have a controllable damping force.

The MR fluid flow phenomenon was the topic of investigation presented in Chapter 2. It was shown that depending on the distribution of the magnetic flux across the orifice, the fluid's flow modelling should be conducted in the appropriate way. The key aspect that should be considered is the assumption of linear or nonlinear distribution of the magnetic flux lines across the orifice. As it was stated in the previous chapter, this aspect can significantly influence the resultant flow rate in the analysed problems.

For that reason the first analysis given in this section concerns magnetic properties of the magnetic circuit in the MR damper. On the basis of the result, the decision will be taken if the magnetic flux lines can be assumed to be linearly distributed across the orifice or not. The following steps are devoted to the topic of prediction of the phenomenon with the chosen model.

3.7.1 Analysis of the magnetic circuit in MRD

A finite element model of the damper's magnetic circuit was developed. This was built using FEMM [40] and the corresponding model is shown in Fig. 3.7. This is an axisymmetric model, which accounts for the magnetic circuit made of pure iron, and the flux leakage into the surrounding air. The housing and the piston rod were assumed to be made of steel. The geometry of the damper's parts were taken from an analysis of the real object performed in the Warsaw University of Technology [83]. The coil was assumed to have 66 turns of copper wire with diameter 1 mm on the basis of geometrical analysis. According to the results presented in Fig. 3.7, the lines of magnetic field are closed in the piston and do not interfere with the surroundings.

Fig. 3.8 presents magnetic flux density distribution in magnified region of the piston. The flux density distribution within the orifices in the piston is constant and uniform.

In accordance to the analysis given in Chapter 2, important factor that influences the flow rate of MR fluid through magnetic valves is the distribution of flux density across the orifices. In order to discuss this parameter in the case of the considered MR damper, two geometrical points were chosen (A and B depicted in Fig. 3.8) on the borders of the orifice. On the line connecting these points the magnetic flux density distribution was plotted for several values of current excitation as depicted in Fig. 3.9.

As it is presented in Fig. 3.9, the flux density distribution along the distance limited by points A and B is linear. Moreover, fluctuation in the values between the chosen points is of the order of thousand parts of Tesla and does not exceed 2% of the average value for a chosen current excitation level. This result allows to assume that the magnetic flux density within the orifice is constant across the

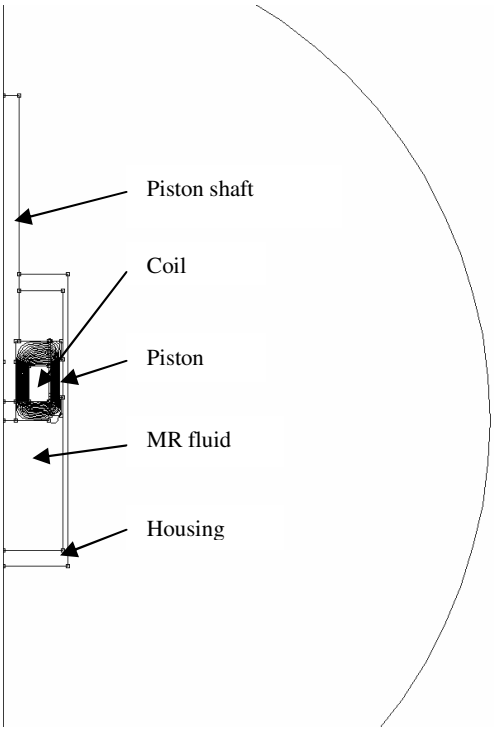

Figure 3.7: Magnetic flux lines analysis in the MR damper.

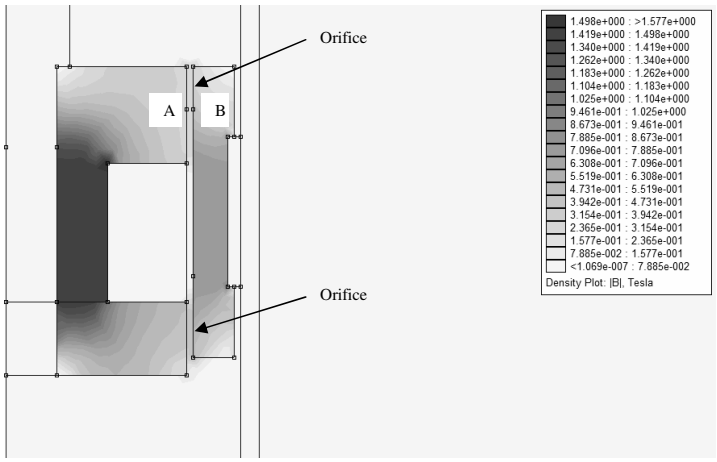

Figure 3.8: Flux density analysis in the MR damper.

gap in the analysed MR damper.

In consequence it is justified to apply the Bingham constitutive model of the MR fluid behaviour for prediction of the MR damper's response.

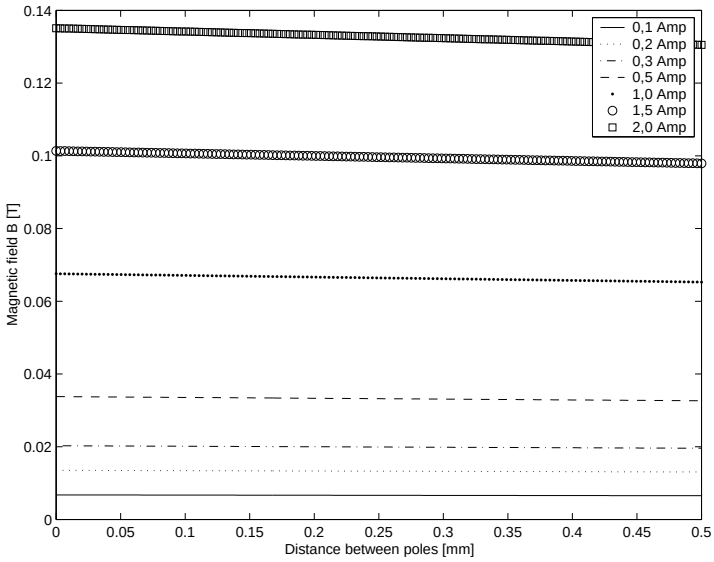

Figure 3.9: Distribution of the flux intensity in the cross-section of the orifice.

3.7.2 Flow of MR fluid through the annular orifice

The previous section was devoted to the analysis of the magnetic flux distribution across the orifice in the analysed damper. It is now proved that the Bingham constitutive relation can be adopted for modelling of the MR fluid behaviour in the analysed device. This section is devoted to the analysis of MR fluid flow through annular orifice that is present in the considered device.

As presented in Sec. 2.6.2, equation predicting the behaviour of the MR fluid under steady flow conditions between parallel plates can be derived and it has analytical solution Eq. (2.33) for the assumed conditions. An important assumption here is that the fluid's flow takes place between two plane surfaces only and it is not affected by any borders. In the case of the considered MR damper, the orifice of the magnetic valve is annular. It means that the flow of the fluid can be considered as developed between two surfaces. In comparison to the model presented in Sec. 2.6.2, it is assumed here that the inner and outer surfaces of the magnetic poles in the piston can be treated as parallel and have equal areas. The approximation is justified by the fact that the difference between the inner diameters of the poles and consequently – the difference between the considered areas of the poles, is less than 1%.

In accordance to the presented discussion, the behaviour of MR fluid within the considered damper was decided to be predicted with equation derived on the basis of the Bingham constitutive relation for the case of steady excitations, as derived in Sec. 2.6.2.

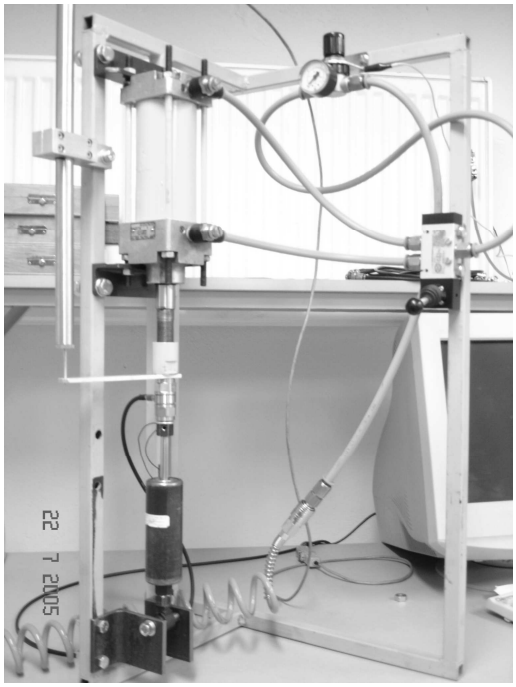

Figure 3.10: Constant velocity excitation stand.

3.8 Experimental verification of the MRD model

There were two general objectives for the experimental tests and therefore, the tests were divided into two parts.

The first one aimed at identification of parameters of the models of the contributing forces, which were formulated in the Sections 3.4, 3.5, and 3.6. The parameters were identified in a series of intentionally designed experiments.

The objective of the second part of the experimental tests was to prove that the proposed model is able to predict the behaviour of the considered MR device. Within this stage of testing two types of experiments were conducted: steady loading of the MR damper with a series of predefined velocities and second, impact loading of the damper on a drop test rig. The experiments with the steady loading were conducted in order to prove that the proposed model responds correctly in a range of velocities and in a range of magnetic excitations values. The experiments with the impact loading were conducted in the passive mode of the damper's operation. Here, the aim was to verify the model in dynamic predictions. That test was conducted only for the passive mode because the used model of the MR fluid flow was derived for steady flows and does not respond appropriately in the dynamic analysis. However, the test of passive mode of operation can validate the model for preliminary modelling of dynamic cases of operation.

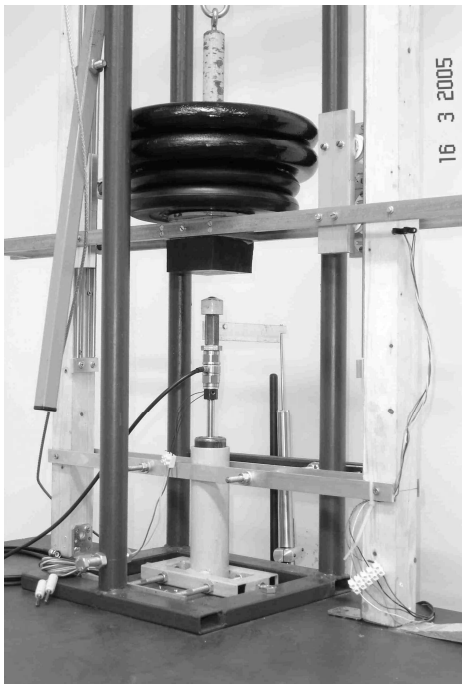

Figure 3.11: Drop test stand.

3.8.1 Identification of the model parameters

The following sections demonstrate the methods used for identification of the model's parameters.

Friction forces

The friction forces, formulated in Sec. 3.6, were established on the basis of the damper's force measurement on the stand that allows to excite the damper with a constant velocity (Fig. 3.10). The result of the measurement is shown in Fig. 3.12. It presents a time history of the force measured on the damper's shaft during changing of the movement direction from compression to decompression. In the figure, a double value of the friction force can be read as the difference between the force levels before and after the turn. As a result, the friction coefficient's value was established for $35N$.

Pneumatic spring

The full design details of the analysed damper are not published by the manufacturer, so parameters concerning the gas spring must have been estimated on the basis of especially designed tests. In order to determine the gas pressure of the pneumatic spring, the damper was subjected to a set of compression tests with constant velocity close to zero. The procedure included compression of the

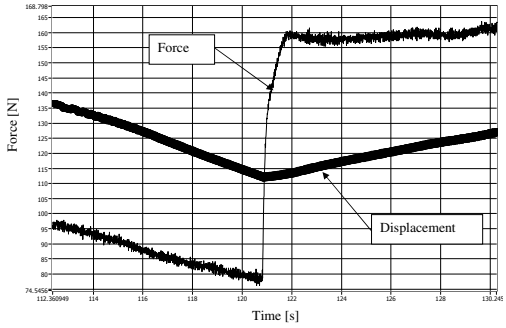

Figure 3.12: Friction force measurement results.

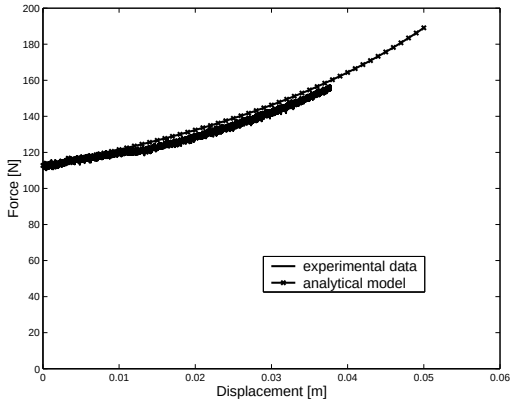

Figure 3.13: Pneumatic spring characteristic.

damper in a quasi-steady routine and measure the force on the damper's shaft. The low value of velocity in the test allowed to eliminate the influence of the viscous reactions from the force measurement. The aim of the experiment was the determination of a pneumatic force value F_{p1} in the domain of displacement of the piston rod, and identification of the gas spring model parameters on the basis of the experimental results.

The result of the experiment is presented in Fig. 3.13. The graph depicts the force measured on the damper's shaft in the domain of the shaft's displacement. Since the velocity of excitation was very close to zero it was assumed that viscous force can be neglected and the force measured can be interpreted as a sum of pneumatic force F_{p1} and friction forces F_f. On the basis of the assumed models of the respective forces and taking into account the identified value of the friction forces as well as inner geometry of the damper, the initial pressure of the gas was identified as 1 MPa. The polytrophic coefficient was chosen to have the value $n = 1.1$ on the basis of experimental analysis of a similar case reported in [15].

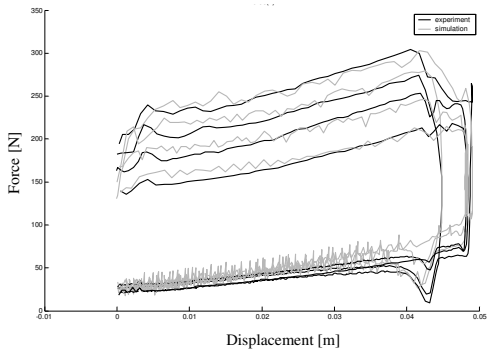

Figure 3.14: MR damper modeling - passive mode of operation.

Hydraulic resistance

The hydraulic force (resulting from flow resistance through the orifice) model was defined in Sec. 3.7. The experiment's aim was to establish the fluid base viscosity by means of comparison between the modelled values and the experimental data. The fluid was assumed to be Newtonian and the damper was assumed to be passive. The experiment contained an excitation of the damper with a cycle of full compressions and decompressions of the device in steady conditions. The compression phase of the test was executed for four velocities of the piston shaft: 0.1 mm s^{-1}, 0.5 mm s^{-1}, 1 mm s^{-1}, 1.5 mm s^{-1}. During the decompression phase of the test the velocity was always kept on the same level of 0.5 mm s^{-1}. The base viscosity of the fluid in the analysed damper was identified in this experiment as 0.025 Ns m^{-1}.

The results of modeling of the damper in the passive mode of operation is depicted in Fig. 3.14. This plot compares the results obtained in the experiment to the results of numerical modelling. Four levels of depicted forces relate to the four velocities of the damper's shaft executed in the test. The line that depicts numerical simulation reflects disturbances that resulted from the fact that for the simulation purpose, an experimentally obtained unprocessed data were used as the model input. It was on purpose of having the most accurate result of the numerical modelling. The experimental data used were the displacement and force measured on the damper's shaft in time. Thanks to taking advantage of using the experimental data in the identification process, it was more accurate since it was possible to avoid any inexactness that may have appeared in the case of simulation of the excitation path.

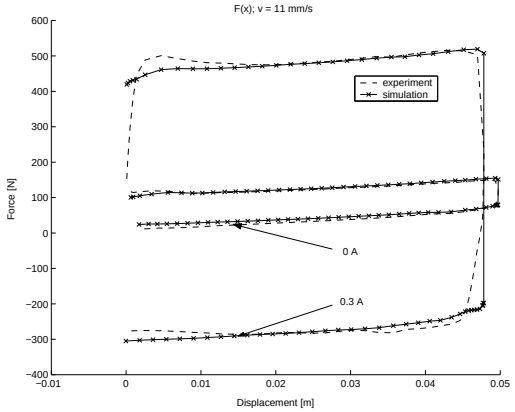

Figure 3.15: Force vs displacement with a constant velocity 11 mm/s, control current 0A, 0.3A.

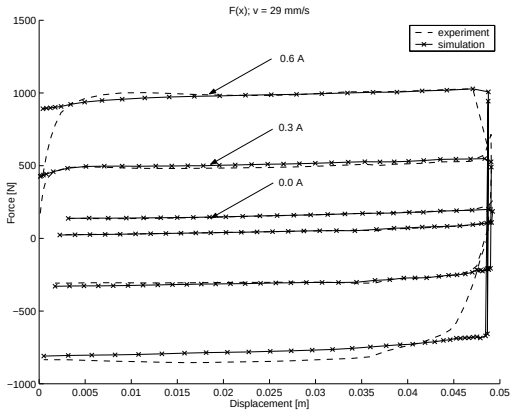

Figure 3.16: Force vs displacement with a constant velocity 29 mm/s, control current 0A, 0.3A, 0.6A.

3.9 Results and discussion

3.9.1 MR damper modelled as an adaptive device

Results of the experimental tests that aimed at checking the MR damper's modelling in the active mode of operation, contained excitation of the device with several constant velocities for a series of various intensities of the magnetic field excitations.

The results of comparison between the data obtained experimentally and the data from modelling are presented in Fig. 3.15, 3.16, 3.17.

In the experiments the damper was compressed and fully extended with the following velocities of the piston shaft: 11 mm s^{-1}, 29 mm s^{-1}, 65 mm s^{-1}. The velocities of the excitations are in the range that executes a steady flow of the MR fluid in the device. This range of velocities was executed in accordance with

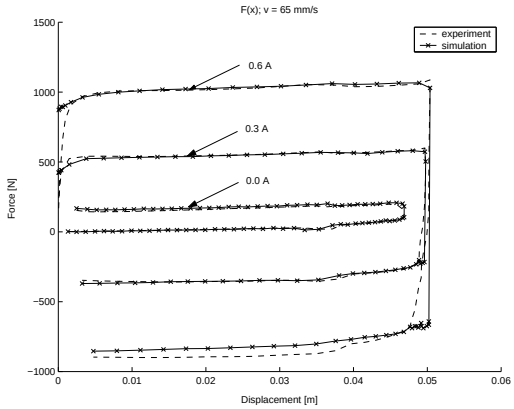

Figure 3.17: Force vs displacement with a constant velocity 65 mm/s, control current 0A, 0.3A, 0.6A.

the limitations that were assumed for the model of MR fluid's flow in Sec. 2.6.2. The control current was changed in the test in the range from 0 Amp to 0.6 Amp. The plots presented in Fig. 3.15, 3.16, 3.17 prove that the proposed model reflects the MR damper behaviour under steady excitation very well. The model predicts the behaviour of the damper properly for the range of velocities and magnetic field intensities.

3.9.2 MR damper under impact loading (passive mode)

The last performed test on the MR damper was subjecting it to an impact loading. The objective of this test was to validate the correctness of the dynamic model of MR damper formulated in the set of Eq. (3.2). During the experiment the damper was mounted in a small drop test rig and loaded by dropped weight. The parameters of the experiment were: drop mass M_1=17 kg, mass of the piston shaft and piston M_2=0.5 kg, impact velocity v_0=1.5 ms^{-1}. The schematic view of the rig is presented in Fig. 3.18. Comparison between the results of numerical modeling against the measured force and acceleration are presented in Fig. 3.19 and 3.20.

The plot in Fig. 3.19 presents axial force measured on the piston shaft in comparison with the data obtained via numerical simulation. The plot in Fig. 3.20 presents vertical acceleration measured on the piston shaft of the tested damper. Exact positions of the mentioned sensors are depicted on scheme in Fig. 3.18. The results of the test proved the capability of the model to predict the damper's behaviour properly in conditions of impact. Due to the fact that the implemented model of the MR fluid's flow was derived for situation of steady flow, the damper's behaviour was validated here only for the passive mode of operation. The result of the validation has shown that the proposed model can be successfully exploited in the initial phase of the designing process.

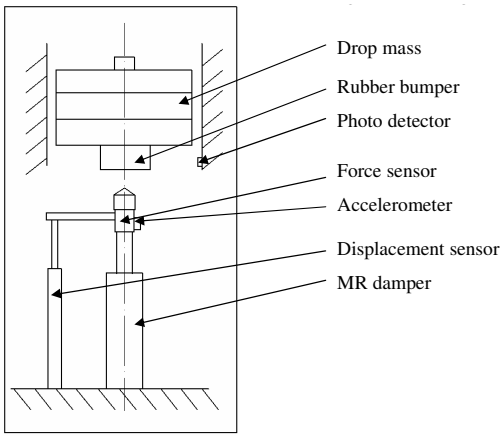

Figure 3.18: Drop test stand scheme.

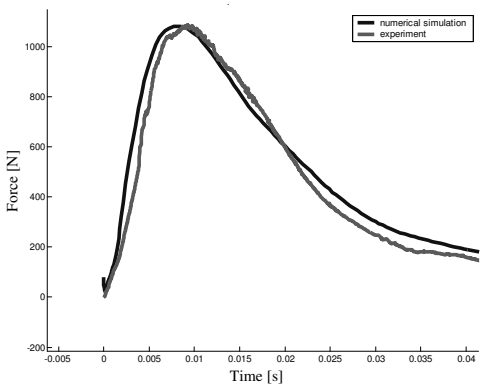

Figure 3.19: Force on the damper shaft in time domain.

3.10 Summary of Chapter 3

An analysis of the MR damper's design was presented in this chapter and an analytical model was proposed. The model accounts for multi-physical nature of the device's operation and takes into consideration fluid mechanics, pneumatic mechanics and friction mechanics that take part in the total force generation in the damper.

The fluid flow analysis was based on the Bingham plastic body flow in accordance with the presented discussion of applicability. The formulated model was implemented numerically in a programmatic engineering environment and simulated. The results of the simulation were verified against the experimental data obtained from two laboratory stands developed during the project activities. The first stand allowed to excite the damper in a steady velocity conditions and the second stand enabled testing of the damper under impact loading. The results presented prove that the proposed model can be used for the purpose of initial

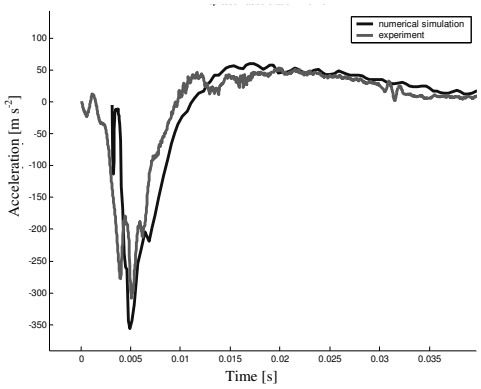

Figure 3.20: Acceleration of the damper shaft in time domain.

scaling and design of an MR device. The proposed model's new feature lies in the new multi-physical approach that was adapted and original interpretation of the reactions interacting in the device.

Chapter 4

Fast execution of MR devices

4.1 Introduction

As it was stated in Chapter 1, introduction of an active system of energy absorption in the aircraft landing gears can be an efficient method for reduction of the value of maximal loadings transferred on the fuselages during the touchdown moment. The statistical gain coming from introduction of controlled LGs was calculated as 16 % [13], which can be translated into significant elongation of the service life of the aircraft.

The phenomenon to be under control in the landing gears is impact, which lasts up to 200 ms in the case of military fighters [84]. For that reason the time delay of the control system for active landing gears must be optimized to meet the restrictions defined by the character of the impact.

In this chapter a discussion is presented in the field of fast actuation of adaptive shock absorbers, based on magnetorheological fluids and their potential applicability in the adaptive landing gears.

4.2 Execution time delays of MR shock absorbers

Active adaptation systems that are intended to operate in the conditions of impact, must respond faster than the duration of the controlled phenomenon. The actuation time delay should be at least 10 times shorter than the total duration of the physical phenomenon. One of the potential actuation systems considered for the case of adaptive impact absorbers is magnetorheological fluid (MRF). The medium gives a unique opportunity of designing compact dampers (MRD) with possibility of smooth changing of its damping force. The fluid changes its properties when it is affected by an external magnetic field. However, the devices require very careful design in order to withstand all the demands. The

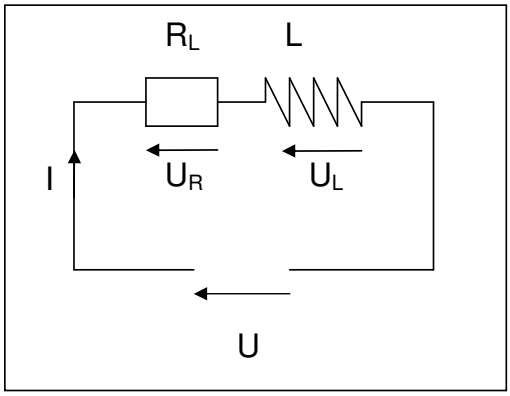

Figure 4.1: RL circuit of electromagnet.

main aspects, which have important influence on the MRD, are: (1) the design of mechanical structure, (2) the design of magnetic circuit that should provide magnetic flux on the required level, (3) selection of the adequate MR fluid which should ensure necessary yield stress, (4) selection of the proper size and shape of the housing in order to find the proper thermal balance and (5) – the total response time of the MR device should satisfy the dynamic requirement of the system under control. The total response time of MR devices depends on the operation of the magnetic actuator. The actuating element in such a system is a compact electromagnet. Intensity of the magnetic field is the factor, which influences the behaviour of MRF. At the same time, the response time of the electromagnet is the parameter that determines the time delay of operation of the complete actuation system. Fig. 4.1 presents the simplest electrical circuit that describes the electromagnet. Two parameters are crucial for the element: resistance of coil R and inductance of coil L. The magnetic field's density generated by the coil is proportional to the value of current in the circuit. In the case of step response of the RL circuit (Fig. 4.1), the process of current rise has the character depicted in the Fig. 4.2. The time of response of this system is defined as reaching by the circuit 95% of the required current value. The governing equation for the considered RL circuit can be written as follows:

$$L\frac{di}{dt} + Ri(t) = U, \tag{4.1}$$

and the solution can be found as:

$$i(t) = \frac{U}{R}(1 - e^{-\frac{R}{L}t}). \tag{4.2}$$

The ratio $\frac{L}{R}$ is called the time constant of the circuit and it is proportional to the time required by the system to reach the steady-state value of the current:

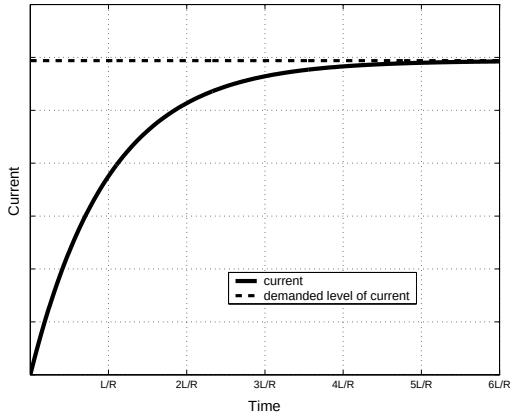

Figure 4.2: Step response of RL circuit.

$$\tau = \frac{L}{R}. \tag{4.3}$$

As it is presented in Fig. 4.2, the response time of the RL circuits can be determined by the time constant. After a period equal to three time constants, the current reaches the level of 95% of the required value.

The time response of the circuit can be influenced by the designer in the following ways: reduction of the inductance L by limiting of the turns on the coil in the electromagnet or by increasing of the resistance of the coil R. However, the inductance L has by two orders of magnitude lower values in comparison to the values of resistance R, which causes that adjusting of the resistance gives more flexibility in optimisation of the circuit. The resistance of the coil can be increased via reduction of its wire's diameter, but the resistance of the whole circuit can be also increased by adding an external resistance in series to the coil. In this way the response time of the coil can be reduced. The consequence of higher resistance of the circuit is higher voltage that must be provided to keep the necessary level of current and induction.

In the case of fast systems, which require the time delays not longer than 1 ms, the increase of the resistance would lead to voltages of the order of hundreds of volts. Such high voltages eliminate this solution from many practical applications. Other possible way of solving the problem of fast operation of the electromagnets is application of a closed loop controller of the current level. The reduction of the time response can be obtained via a method of adapting a temporal over-voltage in the circuit [85, 86]. The RL circuits driven by higher voltage, approach the adequately higher steady-state level of current with the same time delay as at the level of lower voltage. It is the consequence of the fact that the time constant does not depend on the voltage. As shown in Fig. 4.3, the current rate is higher in the case of application of higher voltage. This feature can be utilised by adaptation

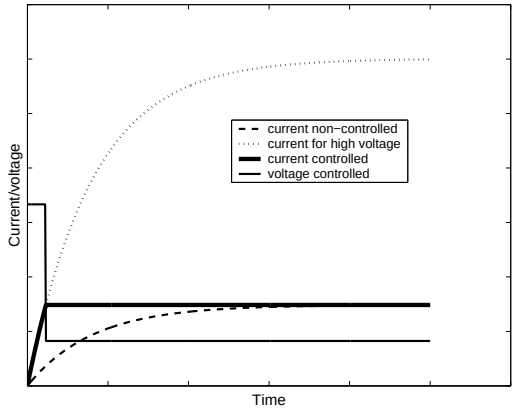

Figure 4.3: Performance of improved RL circuit.

of the current level controller. The basic idea of the controller's logical operation is to perform the algorithm as follows:

$$U(t) = \begin{cases} U_{high} & \text{if } I < I_{demand}, \\ U_{demand} & \text{if } I \geq I_{demand}. \end{cases} \tag{4.4}$$

An example of the controller operation is presented in Fig. 4.3. Voltage increased 4 times in the preliminary period gave the reduction of time response of the order of 15.

4.3 Example of controller

Practical example of the concept presented above was realised in laboratory conditions as a part of the full control system for adaptive impact absorber. The conceptual adaptive impact absorbing system was considered to consist of three essential components: a set of sensors for recognition of the initial impact energy, a micro-controller for executing the established control sequence in real time and the adaptive actuator based on MR fluid [6]. The set of photo-sensors determined the velocity of the structure and specified its mass before the instant of the impact. On the basis of the readings from the sensors, the micro-controller was able to recognise the magnitude of the impact energy. The objective of the control algorithm was then to adapt the actuator to the recognised impact energy. The adaptation of the absorption system was realised by taking advantage of the features of a magnetoreological fluid. In the case of systems devoted to absorption of the impact energy, an important fact was that the full period of the phenomenon was not longer than 50ms (in severe cases), which specified that the update rate of the integrated system (sensors, control unit and actuators) should not exceed 4ms. For this reason, the closed-loop controller for the current

circuit was introduced. The controller was developed on the basis of Field Programmable Gate Array (FPGA) - programmable hardware processing unit and configured with the voltage type of power source. Using of the FPGA processing unit allowed to decrease the period of execution of the logic operations to 5 μs per operation, which allowed to introduce a feedback regulation of the current source. Fig. 4.4 and 4.5 depict two examples of operation of the developed controller with and without the current regulation unit. The graphs present an exemplary time histories of the velocity sensor input and the generated control signals. The tasks for the controller were: identification of the vertical velocity on the basis of the signal from a photo-sensor, determination of the proper control signal sequence, and application of the signal after minimal time delay. The cases on both the graphs are characterised by an identical initial input of velocity photo-sensor, which are represented by the channel number 1 in the Fig. 4.4 and 4.5. A dedicated numerical algorithm recalculated the signal readings in order to determine the impact velocity in the time between the end of the velocity signal and the beginning of the control signal - depicted as channel 2. The controller performed the required logic operations and generated the output signal after 40μs from receiving the velocity input signal (Fig. 4.4 and 4.5). The channel 2 in both graphs in Fig. 4.4 and 4.5, depicts the time history of the control current generation by the developed system. The response time of the current generation circuit determines the dominant time delays of the actuation system. In the case presented in the both Fig. 4.4 and 4.5, the desired current magnitude to generate was 0.5 Amp. The plot in Fig. 4.4 represents the current generation process (channel 2), which is not regulated by the additional fast current generation unit, which effects in time delay being equal ca. 15ms. In the graph in Fig. 4.5 the regulated generation process is presented, which allowed to reduce the current generation time delay to ca. 0.5 ms. The minimisation of the response time made it possible to implement the MR device for the impact application, as the original response time 15 ms gave no practical possibilities to control the process that lasts 50 ms in total.

4.4 Summary of Chapter 4

An efficient method was presented in this chapter for reducing the time delays of execution of MR devices. The physical analysis of the problem was presented and example of a dedicated controller was demonstrated. It was shown in this chapter that it is feasible to utilise the MR fluid in active landing gears from the point of view of time of actuation. The controller presented in this chapter will serve as one of the key devices in the analysis of control system for adaptive shock absorber presented in the following chapter.

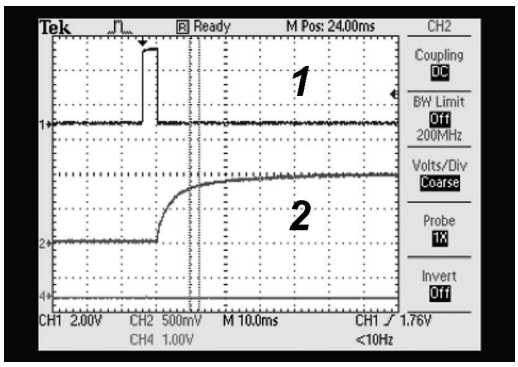

Figure 4.4: Performance of a standard controller in time domain.

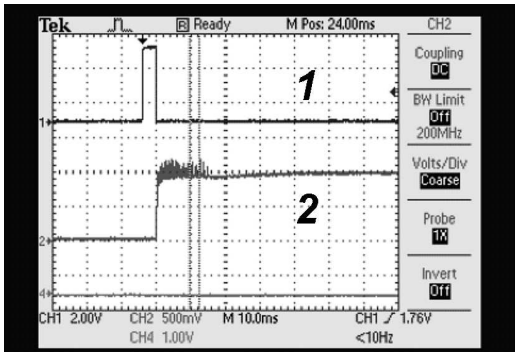

Figure 4.5: Performance of the improved controller in time domain.

Chapter 5

Control of AIA - feedback control validation

The objective of this chapter is to present an integrated feedback control concept for adaptive landing gears (ALG) and its experimental validation. The most important aim here is to prove experimentally the feasibility of the AIA concept on the example of MRF device.

5.1 Introduction

The control system for the adaptation of a landing gear is a challenging task to design. The designer must take into account a series of aspects that cannot be neglected, which are a result of the specificity of aircraft ground operations. The control system design must consider the following three important problems.

The first problem is related to the duration of the phenomenon. In general, the landing impact lasts between 50 and 200 ms, depending on the size of the landing gear and the landing conditions. This short time period makes it difficult to implement control strategies effectively as present actuators are not able to respond fast enough. High response valves currently available on the market offer the best time performance on the level of 10 – 12 ms operational delay in the case of hydraulic valves, directly operated, with electrical position feedback [87]. When it comes to the pneumatic solutions, the fastest designs for valves give the possibility of operation with the time delay equal to 12 ms in the version with an additional pressure accumulator [88]. An important disadvantage of the mentioned solutions is the fact that the standard valve weights are around 2.5 kg. These were strong limitations in the field of application of the active solutions to the adaptive impact absorbers. The proposed actuating system collaborating with the designed hardware controllers is able to execute one control loop with

approximately 4 ms delay. This means that the system is able to update the control signal around 13 times in the case of 50 ms impact duration. If it is assumed that 4 or 5 loops would be consumed for recognition of the process conditions, then the remaining period would be insufficient for execution of an efficient control process. Another important factor is that the impact is random in nature. In contrast to a harmonic process, it is not possible to characterise an impact on the basis of one period and to implement the proper control law for the following periods of the process duration. In these circumstances it is necessary to apply a control system in which the feedback control strategy is assisted by an impact energy prediction unit. The energy prediction unit would process the sink speed, position and the actual weight of the aircraft in order to provide an estimate of the coming impact.

Estimation of the aircraft's sink speed is presently achieved by using pressure-based altimeters. However, much higher accuracy is required for the above purpose. For this vertical velocity measurement (sink speed), the following instruments are considered to be feasible: photo laser, low-power radars or ultrasound sensors. The measurements of the actual mass of the aircraft can be conducted in a passive or an active routine. The passive routine consists of storing data about the aircraft's take-off mass and its centre of gravity. This requires an estimation of the fuel consumption before landing. The active method of mass estimation can be realised via introduction of the real time mass identification system [89], which enables identification of the actual weight loading of each landing gear strut. When real-time mass identification is used with an integrated sink speed measurement, it is possible to assess precisely the energy of the coming impact for each wheel. This configuration would make it possible to establish the optimal strategy for active energy dissipation of the whole structure.

The second problem to be considered for the design of the active landing gear is calculation of the exact position of the aircraft during landing in relation to the runway. The position is important since the impact energy dissipation process must be significantly different, depending on whether the plane lands on one or both main landing gears. The position of the aeroplane is continuously monitored during flight by gyroscopic sensors but the measurements give the absolute outcome, and it is not possible to calculate the exact position of the aeroplane in relation to the surface of the runway. One method of conducting these measurements is to integrate the height sensors with sink speed sensors on each landing gear. This would enable monitoring of the 6 DoF position of the aeroplane so that the landing gears could adapt more effectively to the coming impact.

The third problem that must be considered in the design of active landing gears is the spring-back forces that occur during touchdown. Spring-back forces come from the acceleration of the wheels after contact with the runway surface.

The circumferential velocity of the wheels must be equalised with the horizontal velocity of the aircraft. The horizontal component of the load vector acting on the landing gear causes bending of the strut. The deflected strut springs back rapidly and increases seal friction within telescopic oleo-pneumatic landing gears. This phenomenon introduces significant friction damping, which acts parallel to the oleo-damping generated by the orifice. The influence of friction damping is very difficult to predict since it varies with each landing and is dependent on the horizontal speed of the aeroplane, the sink speed of the aeroplane, runway adhesion, temperature and the exact 6 DoF position of the aeroplane. Prediction of the exact value of friction is a very complex task and the result can be estimated with significant error. In the case of a control system for which the damping force would be treated as an input, the safest and most convenient solution is to use a sensor that measures the total force generated by the landing strut, and to modify it with the adaptive component. Control systems used in such a routine were analysed and tested in the laboratory [58] but the measurement of the total axial force in the strut is a challenging problem due to technological limitations in real applications.

According to the presented discussion, the preliminary requirements for the active landing gear control system are as follows. In connection with the fact that the impact process duration does not exceed 50 ms in the most severe cases, the control system must have the capability of recognising the impact energy in advance in order to adapt the system before the process starts. The second requirement is that the system (actuator + sensors + control hardware) must have the capability to update its state within 4 ms in order to keep the control system performance efficient. The third established requirement for the control system refers to the feedback signal on which the control is based. The signal must describe the total reaction of the landing gear during the process. One of the possible signals can be the total interface force between the strut and the aircraft structure [58], but the force sensor is difficult to assemble from a technological point of view. In the case of landing gear shock absorbers it is possible to mount a pressure sensor of the hydraulic fluid inside the chambers. However, the pressure signal can give only information about the hydraulic shock absorbing force acting on the structure. The signal does not give information about the frictional forces, tyre forces or the spring back phenomenon. The parameter which gives absolute information over the reactions of the fuselage and landing gear is the acceleration measured at the top of each landing gear. This signal was chosen as the input signal for the developed control system.

This chapter presents a proposition for the control algorithm for an active landing gear and an algorithm for an integrated control system. The results were obtained on a laboratory system integrated on the basis of an FPGA hardware platform.

5.2 Methodology

The conceptual adaptive landing gear system was considered to consist of three essential components: a set of sensors for recognition of the initial impact energy (detection of: vertical velocity, the position of the aircraft with reference to the surface of the runway, the mass of the aircraft [89]), a micro-controller for executing the established control sequence in real time, and the adaptive actuator based on MR fluid [47]. The set of photo sensors determined the velocity of the structure in 6 DoF and specified its mass before the touchdown. On the basis of the readings from the sensors, the micro-controller was able to recognise the magnitude of the impact energy. The objective of the control algorithm was then to adapt the actuator to the recognised impact energy. The adaptation of the absorption system was realised by taking advantage of the features of a magnetorheological fluid, which changed its effective viscosity according to the subjected external magnetic field and was different to the previous approaches for shock isolation [90]. This solution made it possible to control the resistance of the fluid flow in the device and to execute the control algorithms by means of adaptation of damping magnitude. In the case of systems devoted to absorption of the impact energy, an important fact was that the full period of the phenomenon was not longer than 50 ms (in severe cases), which specified that the update rate of the integrated system (sensors, control unit and actuators) must not exceed 4 ms. For this reason, a special control loop for the actuation circuit was introduced — fast current generation subsystem.

The typical features of the control systems are controllability and observability. Since the system considered in the experiment can be classified as Single-Input-Single-Output (SISO) both of the conditions for controllability and observability are definitely satisfied [91].

5.3 Control objective

The objective of the considered control system is to minimise the transfer of acceleration to the protected structure during impact. The optimal solution requires analysis of the complete process in order to determine the lowest level of force, which is optimal for dissipation of the impact energy of the recognised magnitude.

Let us analyse the impact energy absorption process in a 1 DoF system by the momentum transfer principle. Let us consider the process of impact energy absorption as a structure that possess a certain linear momentum that must be stopped. The process can be analysed as a transfer of momentum of the structure. It is assumed that the initial velocity of the structure is known, the final velocity is zero and the mass of the structure is invariant.

The motion of a structure of mass m subjected to a force $\bar{F}$ can be described

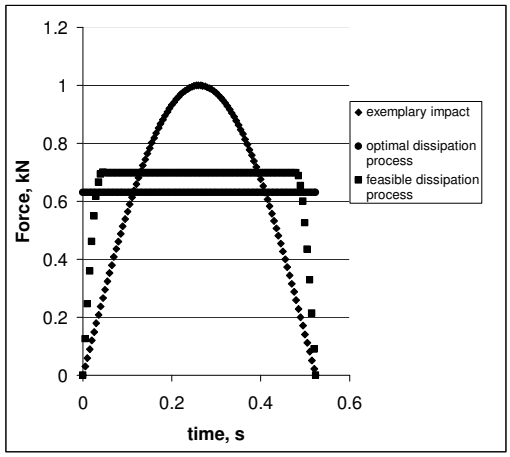

Figure 5.1: Optimization of an exemplary case of impact force distribution.

as

$$\bar{F} = m\frac{d\bar{v}}{dt}, \tag{5.1}$$

where $\frac{d\bar{v}}{dt}$ is the acceleration experienced by the structure.

The equation gives

$$\int_{t_1}^{t_2} \bar{F}dt = m(\bar{v}(t_1) - \bar{v}(t_2)). \tag{5.2}$$

The time integral of force represents the impulse of force and it describes the transfer of the linear momentum $m\bar{v}(t)$ [92].

If we assume that the initial velocity of the structure $\bar{v}(t_1)$ is known, and the final velocity $\bar{v}(t_2) = 0$, then it is possible to derive the force required to stop the structure in the assumed time interval $t_2 - t_1$:

$$\int_{t_1}^{t_2} \bar{F}dt = -m\bar{v}(t_1). \tag{5.3}$$

Let us analyse an exemplary force impulse acting on a 1 DoF system (Fig. 4.5) as a time history of an impact with a maximum force value of 1 kN. Having assumed that the complete process for the analysed impact energy has to satisfy Eq. (5.3), the optimal process of the momentum transfer is depicted as the "optimal dissipation process" in Fig. 5.1. The maximal force level in the considered example was decreased by over 36%.

However, in practice it is not feasible to obtain a constant level of the force acting on the structure during the impact if we take into account the beginning and end of the process. Fig. 5.1 also shows a feasible force/time path ('feasible dissipation process') that satisfies the physical limitations of a real system. Here,

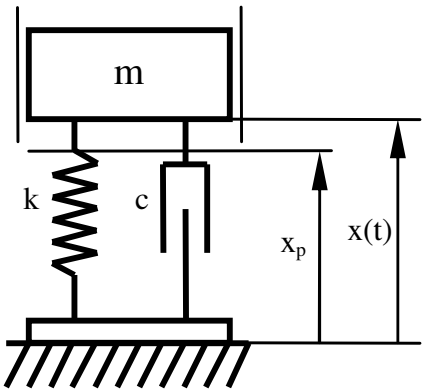

Figure 5.2: Configuration of the damped oscillator at the instant of impact.

the same amount of momentum as for the exemplary case is transferred and the maximum force is reduced by 30%.

As the force is directly related to the acceleration, it is possible to derive the structure's optimal acceleration path during the impact absorption process. When the considered objective is to minimise the maximum load transferred to the structure, a constant acceleration level is most desirable.

5.3.1 Control methodology

The control methodology was based on an energy balance of the system. The assumption was that the total mechanical energy of the falling structure must be transferred to the shock absorber during its first stroke. This requirement is valid since we assume that by the end of the first stroke, the structure must change the sign of velocity in the vertical direction, which is equivalent to a complete transfer of energy.

Let us consider a non-conservative one-degree of freedom system in which the stroke is limited by x_p, which is analogous to the structural limitation existing in the real design (Fig. 5.2). Let us assume that the mass of the structure is known and invariable in time and that the initial impact velocity of the structure is known (measured). The initial mechanical energy of the system can be described as a sum of the kinetic and potential energies within the structure, which it stores at the moment of beginning the dissipating device deflection:

$$E_m = E_k + E_t. \tag{5.4}$$

The potential energy contribution must be considered in the total energy to be dissipated as the energy is not transferred instantaneously. The following analysis will demonstrate the influence of the potential energy of the system. In the case of the invariable mass (e.g. 60 kg used in the experiments) the contribution of

No	Impact velocity (ms^{-1})	Mass (kg)	Stroke (mm)	E_k(J)	E_p(J)	E_m(J)	E_p energy contribution %
1	0.5	60	50	7.5	29.4	36.9	79.0
2	1.5	60	50	67.5	29.4	96.9	30.0
3	3.0	60	50	270.0	29.4	299.4	10.0
4	4.5	60	50	607.5	29.4	636.9	4.6

Table 5.1: Influence of impact velocity on the energy balance of the structure.

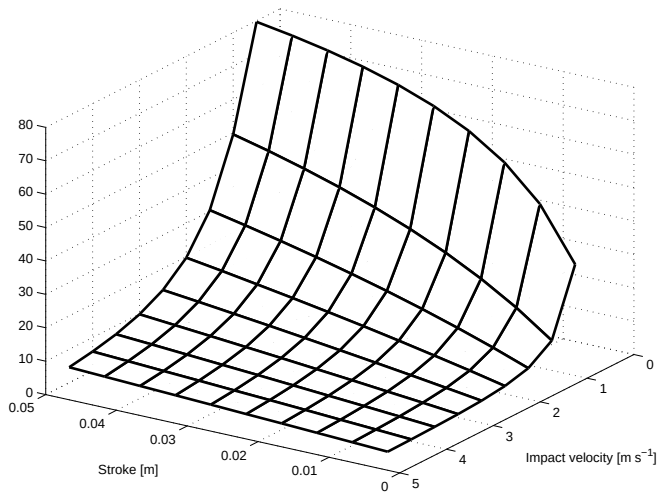

Figure 5.3: Potential energy contributions in the initial impact energy in relation to the total stroke of the shock absorber and initial impact velocity.

the potential energy in the total mechanical energy of the structure before the impact depends strongly on the initial velocity of impact. The contribution is more significant in the range of lower impact velocities. An example of the total mechanical energy of the system for a fixed stroke of absorber and invariable mass of structure is presented in Tab. 5.1.

The potential energy contribution to the total mechanical energy balance decreases with an increase in the initial impact velocity and with a decrease in the absorber's stroke. The maximum contribution of the energy can reach 80% for small impact velocities (Fig. 5.3). In the case of the lowest stroke assumed (5 mm), the contribution for the highest velocity was 0.46%, but in the case of a small impact velocity, the contribution was up to 26%. The analysis shows that, even for small effective strokes of the absorber, the contribution of the potential energy to the total energy is significant and can reach 26%.

In the experimental part of this study the effective stroke was 50 mm, which gave a significant variation in the potential energy contribution: 4.6 – 7.9% as presented in Tab. 5.1. This discussion proves that the potential energy is not a negligible contributor to the total mechanical energy of the considered system.

The total mechanical energy of the structure is intended to be transferred to the shock absorbing device. In the considered case of damped oscillator, the mechanical energy is transferred in two ways: dissipation via the viscous damper c and accumulation via the spring k. The transformed energy can then be denoted as

$$E_t = E_s + E_t. \tag{5.5}$$

It is assumed that the entire mechanical energy is transformed by the shock absorber in order to make the absorption process efficient:

$$E_m \equiv E_t. \tag{5.6}$$

According to that condition the entire impact energy is dissipated or accumulated during the process.

In accordance with the conservation of energy principle, the energy can be transferred into other forms by means of work done on the system, which gives the following result:

$$E_m \equiv W_i = (F_d(\dot{x}) + F_s(x))\cdot x(t)). \tag{5.7}$$

The work W is done by the forces: $F_d(\dot{x})$ (damping force) and $F_s(x)$ (spring force) on the displacement $x(t)$.

Consequently, we assume that all the mechanical energy of the system is lost due to the dissipative action of the shock absorber and stored due to accumulative action of the shock absorber. The objective is then to consume this mechanical energy on the assumed effective stroke s_{eff}.

The optimal situation is when the force is constant during the impact and we can calculate this optimal dissipation path as follows:

The transfer of energy is equivalent to the work done by the impact system:

$$W_i = \int_{x1}^{x2} \bar{F} dx, \tag{5.8}$$

where $\bar{F} = \bar{F}_d + \bar{F}_s$.

Since the whole mechanical energy of the structure must be transferred,

$$W_i \equiv E_k + E_p. \tag{5.9}$$

After integration of the above relations, the optimal force level for the 1 DoF impact system can be defined as:

$$\begin{aligned} F_{opt} &= F_d(\dot{x}) + F_s(x), \\ F_{opt} &= \frac{E_k + E_p}{s_{eff}}. \end{aligned} \tag{5.10}$$

This force level can be used as a reference for the active landing gear control algorithm.

The effective stroke s_{eff} can be calculated from the assumption that by the end of the stroke, the force in the strut can be formulated as follows:

$$F_{opt} = F_s(s_{eff}). \tag{5.11}$$

Then, after substitution of Eq. (5.11) into Eq. (5.10) the s_{eff} can be calculated from the following equation:

$$F_s(s_{eff}) = \frac{E_k(v_0) + E_p(s_{eff})}{s_{eff}}, \tag{5.12}$$

where v_0 is the structure's velocity at the moment of impact.

5.3.2 Control algorithm

A feedback control algorithm was developed for the 1 DoF adaptive shock absorber, which can operate with two input signals: axial force value and acceleration value. The algorithm is divided into two phases — first before and second after the instant of impact. During phase I, parameters of the impact are recognized, and during phase II, the control of the process is performed.

Algorithm details:

Phase I — before impact

(1) Determination of the initial impact velocity v_0 of the falling structure.

(2) Determination of s_{eff}:

$$F_{opt} = \frac{E_k(v_0) + E_p(s_{eff})}{s_{eff}},$$
$$F_{opt} = F_s(s_{eff}).$$

Taking into account the following constraint:

$$F_s(s_{eff}) > mg,$$

where: m – mass of the structure and g – gravitational acceleration.

(3) Determination of the optimal required level of the absorption force on the considered effective stroke:

$$F_{opt} = \begin{cases} \dfrac{E_k(v_0) + E_p(s_l)}{s_l} & \text{if } s_{eff} > s_l, \\ \dfrac{E_k(v_0) + E_p(s_{eff})}{s_{eff}} & \text{if } s_{eff} > s_l, \end{cases}$$

where s_l is the maximum stroke permissible by the structural limits.

(4) Determination of the desired deceleration value for the considered mass of the structure:

$$a_d = \frac{F_{opt}}{m}.$$

(5) Determination of the desired reference level of deceleration during the process:

$$a_C = a_d - g.$$

Phase II — after impact

(6) At the instant of impact, start control of the adaptive damper in order to develop the desired level of deceleration and in the feedback routine (on-off control)

$$Ctrl(t) = \begin{cases} C_{High} & \text{if } a_m(t) < a_C, \\ C_{Low} & \text{if } a_m(t) > a_C, \end{cases}$$

where $a_m(t)$ is the actual measured value of the structure's acceleration.

5.4 Laboratory control system configuration

The feedback control system was designed in order to execute the sequence of tasks presented in Fig. 5.4. These were: recognition of the impact energy on the basis of the initial velocity and mass of the falling structure (velocity sensor), determination of the optimal acceleration value for the adaptive impact absorber and execution of the control signal in the closed loop during the process (acceleration sensor feedback). The objective of the feedback control loop was to regulate the damping of the actuator in order to maintain the optimal acceleration level with reference to the identified impact energy and the stroke of the adaptive absorber. The feedback signal was acceleration of the structure. The designed and realised controller was implemented on an FPGA platform, which executed the on-off controller. Execution of the feedback loop was accelerated via introduction of an additional current control loop. This monitored the actual control current level and regulated it in order to shorten the response delay of the system (fast current generation — Fig. 5.4). This current control loop reduced the current generation time to 500 μs (for 1 A level).

The proposed control algorithm was implemented on the FPGA hardware platform (cRIO) and verified experimentally on a small laboratory drop test bench (Fig. 5.5). A lab-scale model of an adaptive impact absorber was designed and fabricated by making use of an MR Damper manufactured by LORD Corporation [47].

In the experiment the mass of the structure was assumed to be known and invariable. The first component of the control system was a photo-logic switch,

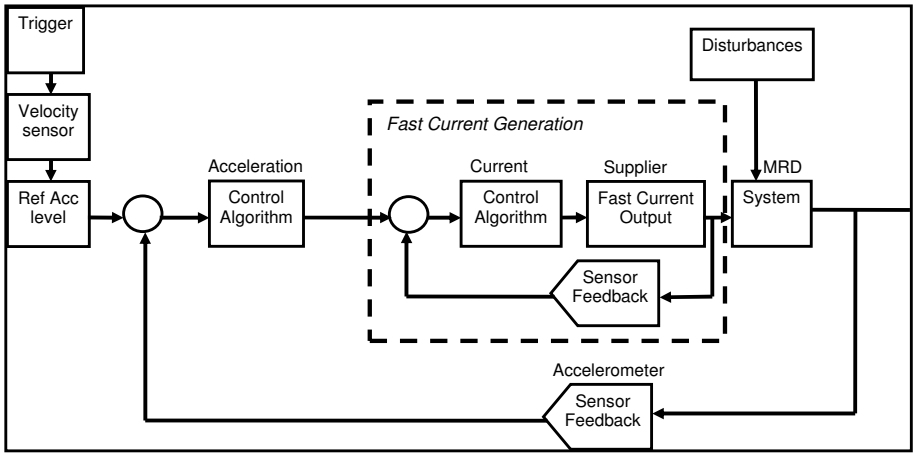

Figure 5.4: Feedback control system based on acceleration signal.

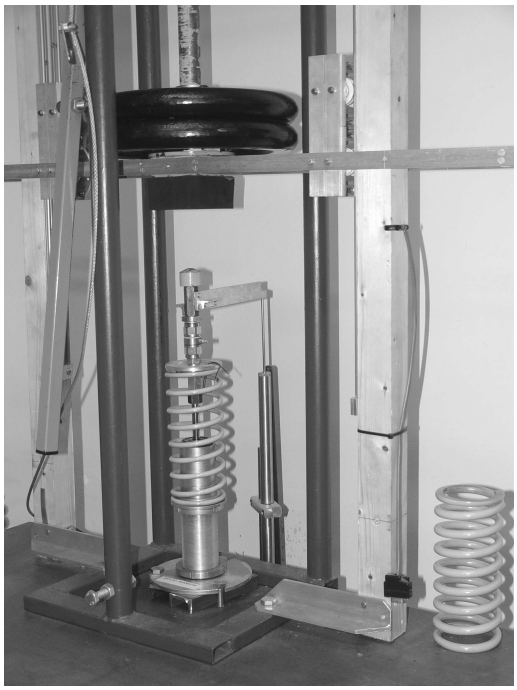

Figure 5.5: AIA test bench.

which was adapted to detect the approaching drop-mass and its corresponding velocity. In the considered case, the direction of the velocity vector was invariant due to the guidance rails used in the laboratory stand (Fig. 5.5). The data from the photo-sensor was fed forward to the FPGA electronic control unit, which was the second component in the system. The FPGA control unit executed the proposed on-off control algorithm and the fast current generation subsystem. The signals characterising the performance of the adaptive shock absorber and the

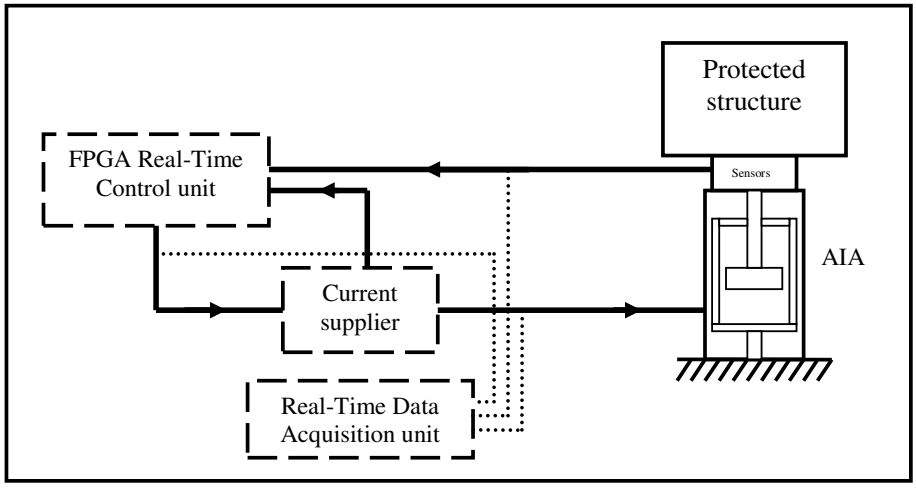

Figure 5.6: Control system configuration.

course of the events were monitored and acquired via a separate system operating in a real-time routine (Fig. 5.6).

5.5 Results

Results of the conducted experimental verification depict two algorithms that were validated. The first part of the section consists of graphs characterising the execution of the acceleration feedback control on the experimental stand. The second part of the section presents the second control algorithm, which is a modified version of the acceleration feedback control. The modification was introduced in order to perform control of the recoil stage of the impact absorption.

Fig. 5.7 shows a typical result that was acquired on the drop test stand, which illustrates the operational principle of the developed controller. The graph depicts the time history of acceleration of the falling 1 DoF structure as well as the time history of the control signal that was fed forward to the MR adaptive shock absorber. The reference signal for the controller was an acceleration of the mass equal to 5 ms^{-2} (dash dot line, Fig. 5.7). The controller signal was switched any time the acceleration signal crossed the reference level. The lower graph (Fig. 5.7) gives an overview of the controller's execution. It is shown that the acceleration of the structure was successfully modified by the controlled MR damper every 5 ms, which gives the control frequency rate as 0.2 kHz. It is worth noting that 0.2 kHz is the operational frequency of the complete integrated control system. In order to reach the result, the total time delays of the actuator, sensors and the amplifier must have been minimized to rates below 1 ms.

Fig. 5.8 presents acceleration and velocity of the falling structure in time domain. The acceleration plots were obtained from the acquired data and the

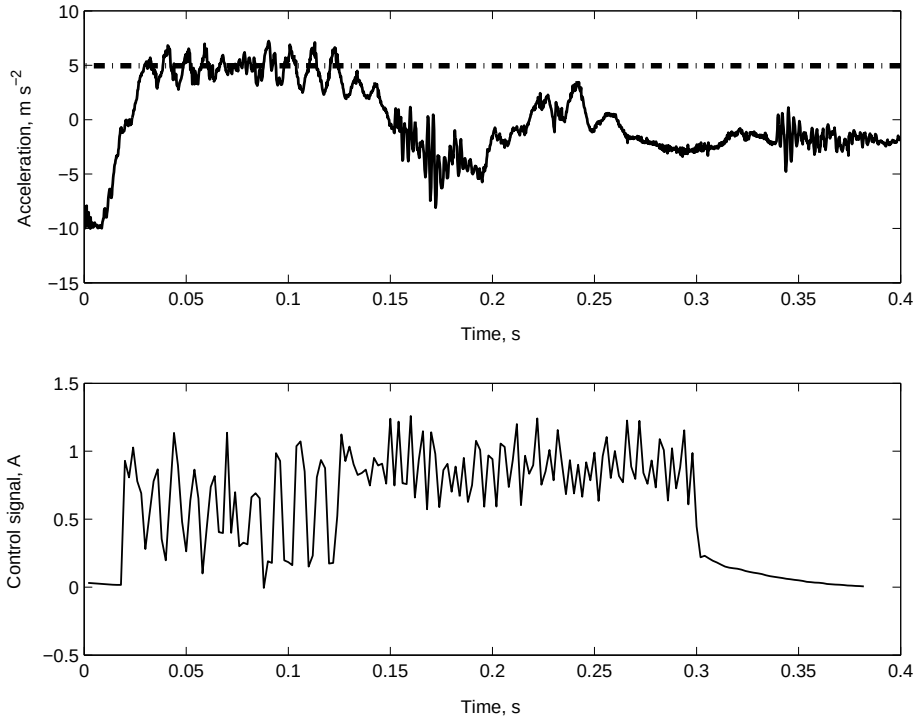

Figure 5.7: Example of the control execution for the reference acceleration level equal to 5 ms^{-2}.

velocity plots were obtained via numerical integration of the acceleration signal in the time domain. The third graph shown in Fig. 5.8 represents the measured displacement of the shock absorber's piston. All graphs depict the same phenomena recorded by different sensors and for that reason these are presented in the same time plot. However, the data measured from the piston can be inconsistent with the signal acquired on the falling mass due to kinetic incompatibility — the structures were not connected by a stiff joint. Nonetheless, the characteristic time points of the process can still be analysed even though the measurements are not strictly consistent.

Each plot compares the results obtained for two cases: without active control (control–off) and with active control activated (control–on). The control–off case is representative of the behaviour of a classical passive device with linear spring and viscous damper. The impact energy was higher than it was possible for the passive shock absorber to absorb, which resulted in a structure-housing collision.

The data acquisition was triggered 5 ms before the moment of impact. The acceleration of the free falling mass was around -10 ms^{-2} and the velocity was reaching the initial level of 0.95 ms^{-1}. The denoted time instant t_1 (also illustrated in Fig. 5.9) corresponds to the moment when the falling structure first contacted the shock absorbing device. In accordance with the previously derived

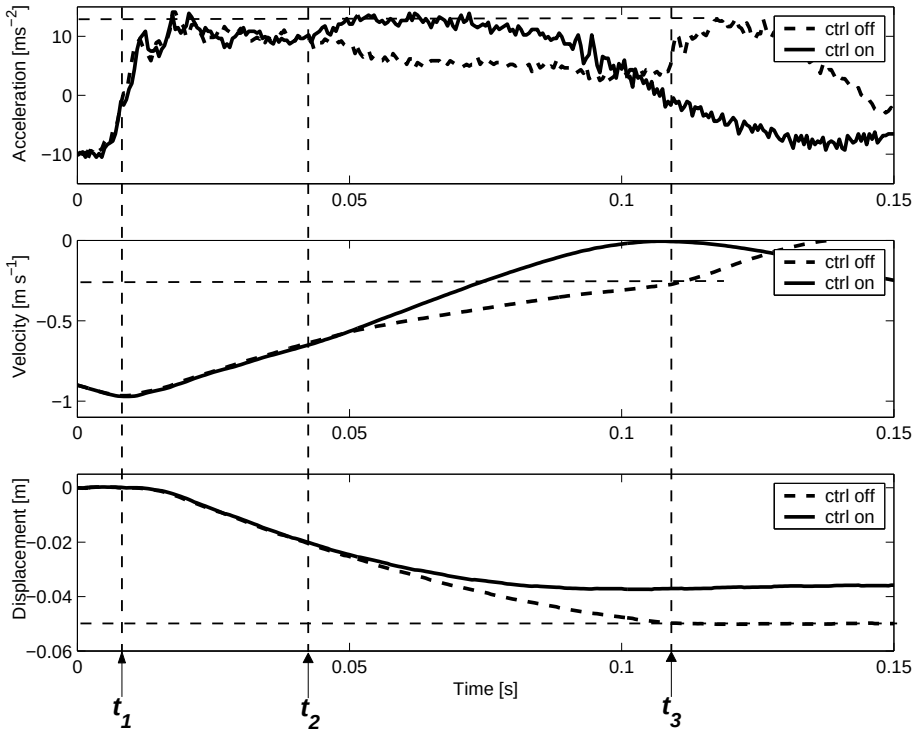

Figure 5.8: Kinetics of the analysed 1 DoF system in time domain.

control strategy, the reference acceleration of the structure was set to 12 ms^{-2}. The process of the passive and active energy dissipation was similar up to the time instant t_2 at which the non–controlled acceleration started to decrease (t_2, Fig. 5.8). After time t_2, operation of the control system is visible by the path of the solid line. Between the time instants t_2 and t_3, the acceleration is kept close to the determined reference level 12 ms^{-2}. The difference in the acceleration paths allowed the structure to be stopped after 36 mm of displacement without crossing of the maximal admissible acceleration level. For the non-controlled structure the acceleration level was decreasing throughout the duration of the impact. The result was that, at time instant $t_3 = 0.11$ s (illustrated also in Fig. 5.9), a collision occurred between the structure and the housing because the displacement of the piston reached the maximal value -0.05 m. The collision with the housing resulted in an unfavourable rapid increase of the acceleration. This sudden impact did not immediately reduce the velocity to zero because of the protection assured by the rubber bumper mounted in the system.

c

The graphs in Fig. 5.8 show that the implemented control system can dissipate the previously defined impact energy without exceeding the permissible acceleration, whilst maintaining a 30% lower stroke than the limit value. The results illustrate that it is feasible to develop an effective feedback control system

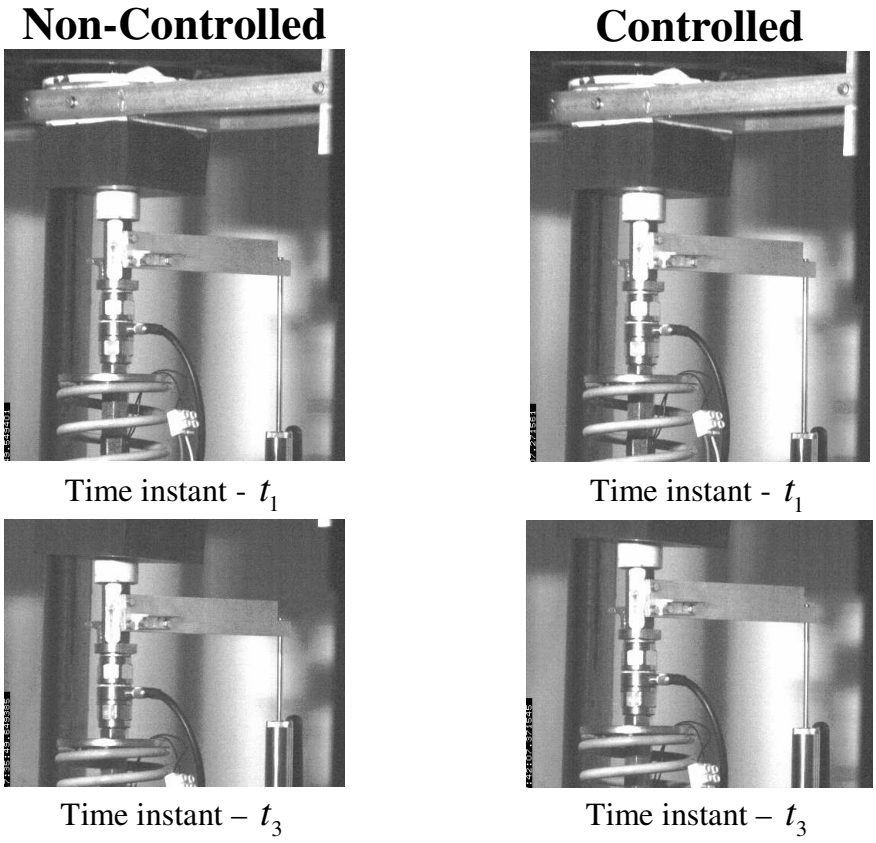

Figure 5.9: Pictures of the experimental set-up taken with a fast digital camera.

for adaptive impact absorbers based on MRF.

Fig. 5.10 illustrates the difference in the falling structure kinematics which was obtained thanks to the introduction of the control system. The passive case is depicted by the dotted line. The initial velocity 0.95 ms^{-1} was reduced linearly in the domain of displacement. The non-optimal design of the shock absorber for the tested impact energy resulted in the collision of the structure with the housing, which took place at the limit displacement of 0.05 m. The dashed line in the graph denotes the velocity of the structure at the moment of collision with the housing: -0.28 ms^{-1}.

The solid line in Fig. 5.10 depicts the process of the controlled impact energy absorption in which the acceleration of the protected structure was kept around the referenced level 12 ms^{-2}. It is shown that the introduction of the acceleration control feedback reduces the velocity of the structure to zero within 37 mm of the total stroke and without exceeding the maximum acceleration of 14 ms^{-2} (visible also in Fig. 5.11).

It is proved that 1 DoF impact absorption systems can be controlled using force feedback control systems [58]. During the experiments conducted in the

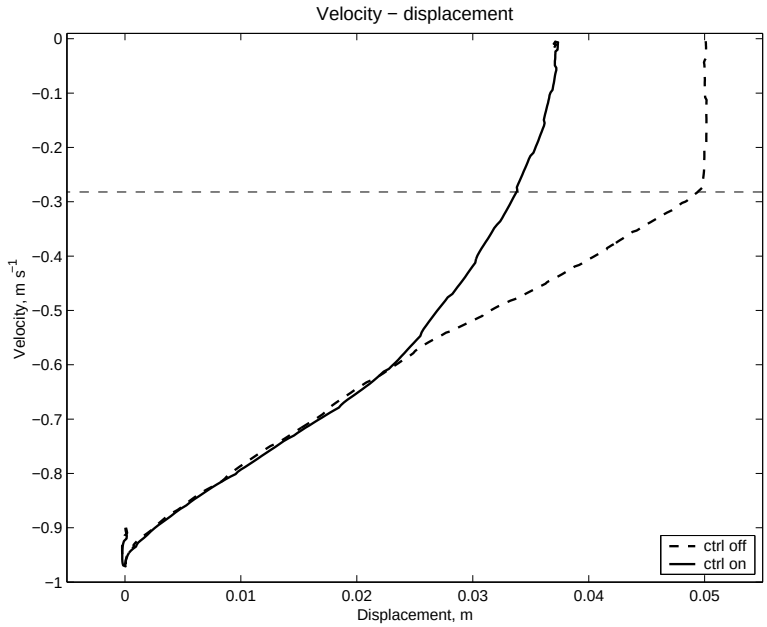

Figure 5.10: Phase plot of the falling structure for the cases 'control–off' and 'control–on'.

present research, the force and acceleration signals were measured and compared. In the theory, the signals should be proportional in accordance to Newton's basic laws of dynamics. However, due to the kinetic incompatibility between the structure and the piston of the shock absorber (existence of the bumper on the interface), the proportionality was disturbed at the moments when the acceleration was changing its sign. As shown in Fig. 5.11, the interface force and acceleration are proportional for most of the process's duration. The measured acceleration has a particularly stable value and gives a more reliable overview of the structure's kinematics. Since the objective of the control system is to prevent the loads transferred to the falling structure from exceeding the admissible level, it is more valuable to monitor the acceleration signal of the structure. This gives accurate information throughout the impact process and can therefore be used as an effective signal for the control input. In Fig. 5.11, it can be seen that the acceleration profile is free from rapid disturbances that are visible in the force profile in the same periods (without taking into account the acquisition noise). It is also very important that the acceleration signal relates to the absolute value of the structure's kinematics. In contradiction, the force signal represents always a resultant of two reactions: the structure and the interface material, which is placed on the impact surface (in this case, the rubber bumper).

So far, the considered control algorithm focused on the first compression stroke that occurred right after the impact instant. In what follows, the control of the recoil phase of the impact absorption is analysed. The original control

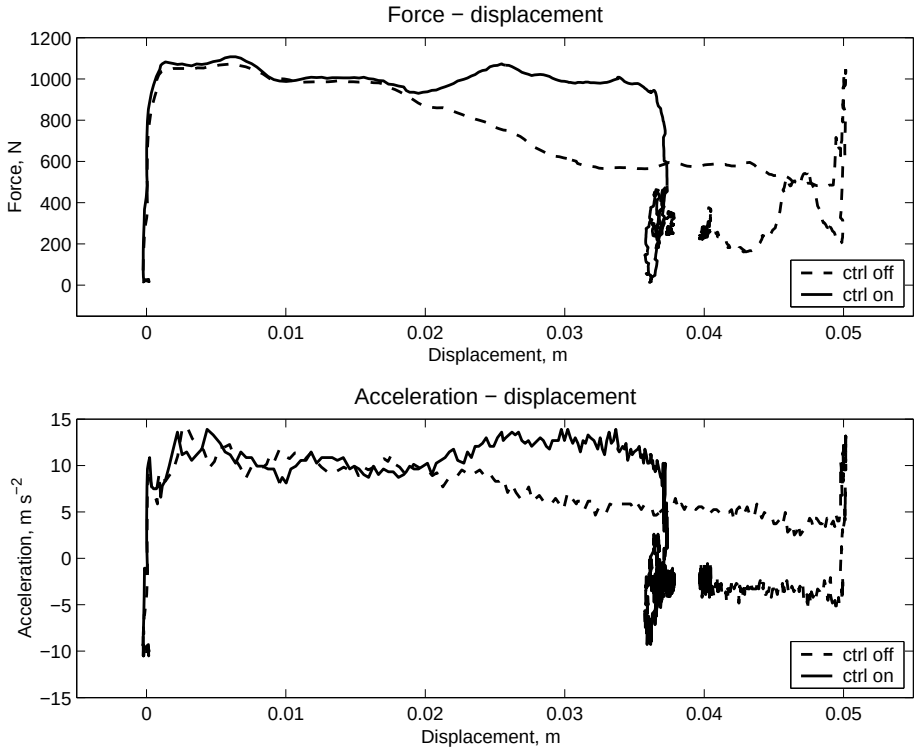

Figure 5.11: Acceleration and force comparison.

algorithm assumed that the piston would start the recoil move smoothly after the first period of energy absorption. However, energy is stored due to compression of the rubber bumper, and at the moment when the piston stops, this stored energy is released. Consequently, the structure is lifted rapidly and starts to oscillate in an undesirable manner. The objective of the proposed control algorithm is to mitigate these oscillations.

Since the energy stored in the rubber bumper can only be released by extending the element, it was proposed to direct the process towards the shock absorber in order to dissipate it. The heuristic algorithm assumed that, after the monitored acceleration crosses level zero, it determines that the spring in the system is maximally compressed and it supports the fallen structure. At the same period the energy stored in the rubber bumper must be released. To do this in a controlled routine, it was proposed to decrease the viscous resistance of the damper below the inertial force of the structure, so that the bumper can compress the shock absorber and dissipate the stored energy.

Fig. 5.12 presents a comparison of the system response under the original and modified control algorithms. The analysis was conducted on the basis of differences in the piston displacements, structure accelerations and the interface forces occurring during the recoil phase. The first and second graphs (Fig. 5.12)

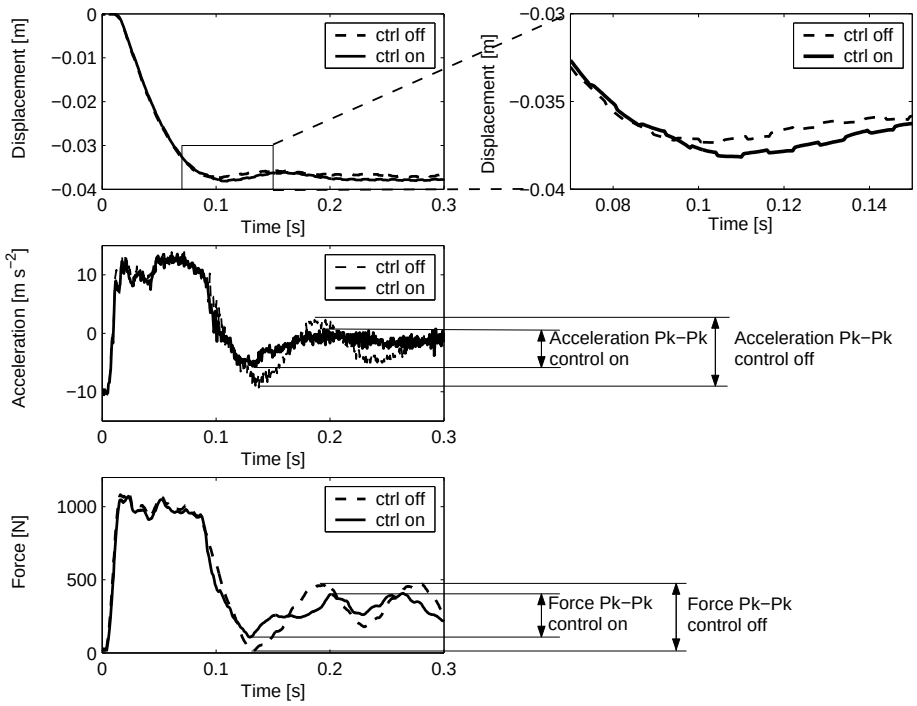

Figure 5.12: Results of the recoil stage control.

depict the difference in displacements after introduction of the modified control algorithm. In the considered case, the effect was to increase the compression of the AIA by 1 mm. In the case of a landing gear, it would be slightly more than this but it would never exceed 3% of the total stroke of the landing strut. The third graph illustrates the improvement in the acceleration response of the oscillating mass. Here, the peak-to-peak acceleration level has been mitigated by 40%. The fourth graph (Fig. 5.12) illustrates the minimisation of the force oscillations. As shown, the peak to peak force has been decreased by 40%.

The operational principle and results of the control system implementation are the same for the acceleration input signal and for the total axial force input signal to the control unit. However, acceleration measurements are easier to conduct in real applications. The effect of the introduction of the control system upon the shock absorber was presented in [58] in the example of minimisation of the transferred loads.

Fig. 5.13 illustrates experimental results of the operation of the adaptive impact absorber integrated with the developed control system (for axial force input signal [58]) and its influence on the energy dissipation process. The plot depicts the impact forces' history on the device presented in the domain of the displacement of the piston. The figure presents a comparison between three cases of the equal energy impact absorption events: non-adapted, adapted and

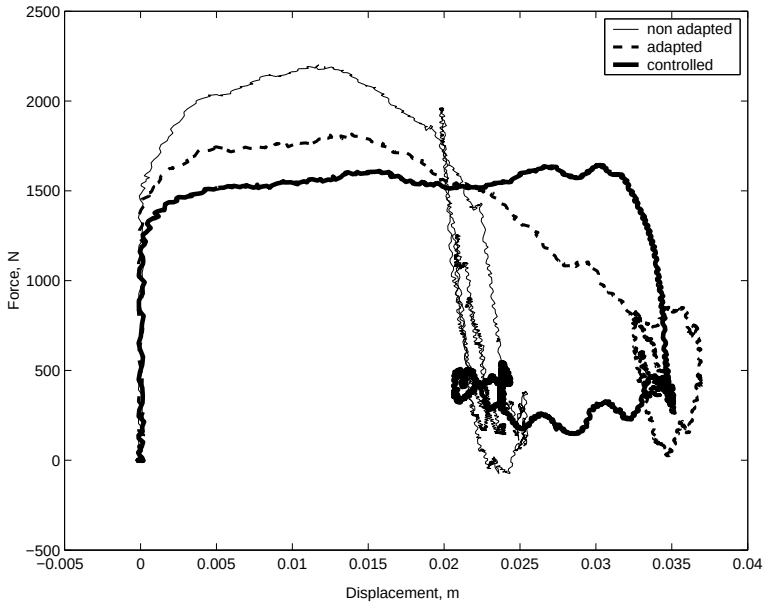

Figure 5.13: Comparison of three experimental energy dissipation processes [58].

controlled. The non-adapted case represents the situation when a passive impact absorber was optimized only for the high critical energies and then loaded with impact of lower energy. Initially the process had a non-desirable character from several point of views. Because of high viscous resistance of the system, the piston moved on a shorter distance than available and a large portion of the energy was stored in the elastic bumper. The energy was released in an undesirable way after stopping the device (high force peaks visible on the 'non-adapted' curve between 20 and 25 mm of displacement). The adapted case represents a situation when the impact absorber was adapted and realised the control strategy, in which the AIA's damping force was held on a pre-selected constant level during the whole duration of the dissipation process [58]. The controlled case represents the situation, when the adaptive impact absorber realized the feedback control strategy. The gain, reached thanks to introduction of the adaptive strategy, was reduction of 20% of the maximal dynamic forces level. However, the process of the energy dissipation was not performed optimally as the dynamic forces fluctuated significantly during the process. The effect of the forces' variation was further reduced by introduction of the feedback control strategy, which resulted in a further 10% reduction of the maximal dynamic forces transferred on the protected structure.

5.6 Summary of Chapter 5

The chapter was focused on the problem of damping force control in the landing struts and experimental validation of its feasibility. The following points conclude the results:

(1) The proposed feedback control algorithm was shown to be valid for the adaptive impact absorber and was proved to reduce the impact forces by 30%.

(2) It was proved to be feasible to have the actuation of the MR devices in a period shorter than 5 ms. The developed control system was validated by controlling the MR device with a 200 Hz update rate.

(3) The proposed methodology of the damping force adaptation in shock absorbers was proved to be an efficient method of increase of the energy absorbing capability. Acceleration feedback control of the AIA reduced the required stroke of the shock absorber by approximately 30%, which effectively improved its energy-consuming.

(4) Acceleration of the falling structure was shown to be an effective input signal for the control system of AIA.

(5) Introduction of the double-stage control strategy to the algorithm resulted in a 40% reduction in the after-process oscillations, as the effect of intelligent dissipation of energy stored in the elastic elements of the mechanical system.

The objective of the presented chapter was to answer the question whether it is possible to control effectively and fast enough the damping force of a shock absorber. The time limitation here was an important factor as the total time of the impact was shorter than 100 ms. Such durations are a strong limitation for many actuation systems. The analysed case did not take into account the flexibility of the aircraft's structure but with the obtained dynamics of the actuation the proper strategy is possible to be implemented.

Chapter 6

AIA's potential for improvement

6.1 Introduction

This chapter is devoted to the numerical and experimental analysis of potential improvement that could be obtained on aeroplanes thanks to employment of the adaptive impact absorber based on the magnetorheological fluid. The analysis was performed on the example of an existing small passenger aircraft I-23 Manager designed by Institute of Aviation in Warsaw. As the reference, a performance of presently utilised nose landing gear was employed. The performance of the landing gear with employed the control methodology introduced in the previous chapter, was compared to passive shock absorber's model and to feed forward control strategy based on the existing landing gear. As a result, an assessment of relative improvement for the aeroplane was obtained.

The following section states the numerical model used for reflection of the aeroplane's passive behaviour and validates it against measured data obtained during testing sessions conducted in Institute of Aviation. Next, the control strategies used to minimise the peak strut force are discussed. Finally, the potential for improvement is estimated and compared to the experimental results.

6.2 Numerical model

For the purposes of this analysis, the adaptive landing gear (ALG) is represented by a 2 DOF system, shown schematically in Fig. 6.1, and modelled by the following set of equations (a modified version of the equations derived by Milwitzky

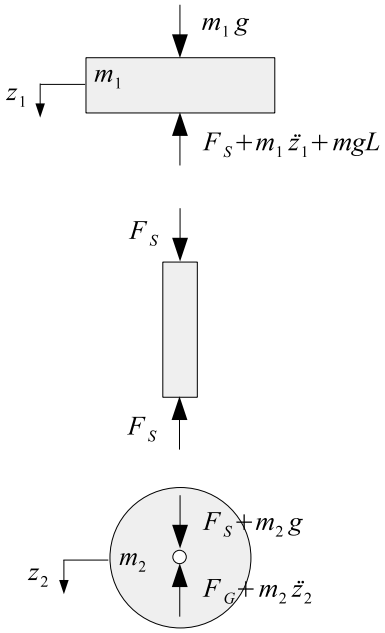

Figure 6.1: Free-body diagram of landing gear (aircraft, strut and wheel).

and Cook in [15]):

$$\begin{aligned} m_1 \ddot{z}_1 &= m_1 g - F_S - mgL, \\ m_2 \ddot{z}_2 &= m_2 g + F_S - F_G, \\ z_1(0) = z_2(0) &= 0, \\ \dot{z}_1(0) = \dot{z}_2(0) &= v_0, \end{aligned} \tag{6.1}$$

where m, m_1 and m_2 are respectively total, upper (aircraft) and lower (wheel) masses ($m = m_1 + m_2$, $m_2 = 8.71$ kg); z_1 and z_2 denote their vertical displacements from initial contact; L denotes the lift factor ($L = 0.667$ [12]); F_G is the vertical force acting on tire at the ground; F_S is the total axial strut force, and v_0 denotes the initial landing sinking velocity.

The mass m and the sinking velocity v_0 are limited [93] by

$$\begin{aligned} 288 \text{ kg} &= m_{min} \leq m \leq m_{max} = 422 \text{ kg}, \\ 0 \text{ m/s} &= v_{0(max)} \leq v_0 \leq v_{0(max)} = 2.93 \text{ m/s}. \end{aligned} \tag{6.2}$$

For the assumed detailed statistics of the landing mass m and the sinking velocity v_0, see Section 4. The mass m is the *reduced* mass (mass per landing gear) and is less than the *total* landing mass of the aircraft. The upper bound of 422 kg corresponds to the maximum I-23 design landing mass of 1117 kg and the lower bound of 288 kg was chosen to be proportional to the mass of an empty aircraft with a pilot [93].

The dynamic tire force–deflection characteristics of the I-23 nose LG, denoted in Eq. 6.1 by F_G, has been obtained by fitting experimental data measured in

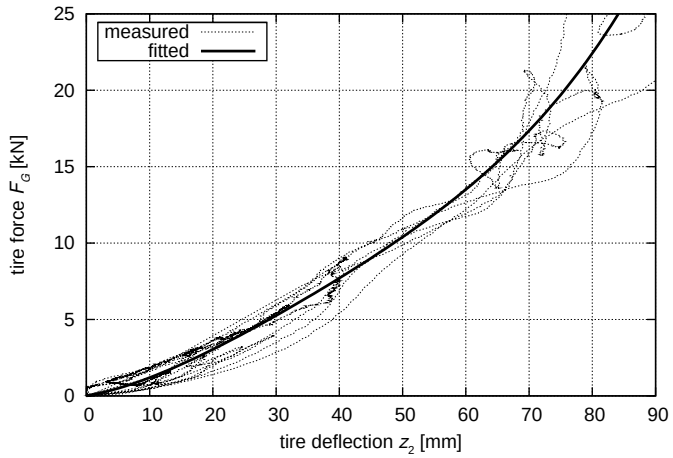

Figure 6.2: Measured and fitted tire force–deflection characteristics (I-23 nose LG).

three dynamic tests (see Fig. 6.2). The least squares fit is a fourth-order polynomial:

$$F_G(z_2) \approx (7.3\,10^4 + 5.4\,10^6 z_2 - 8.6\,10^7 z_2^2 + 6.4\,10^8 z_2^3)\max(z_2, 0),$$

where the last multiplier denotes symbolically that F_G vanishes when the tire hovers above the ground.

The total axial strut force F_S is modeled as a sum of four forces:

$$F_S = F_a + F_h + F_f + F_d, \tag{6.3}$$

which are respectively strut pneumatic, hydraulic and friction forces, denoted by F_a, F_h and F_f, and the delimiting force F_d, which prevents excessive strut elongation. Notice that introduction of the actually occurring delimiting force F_d greatly simplifies modeling of the landing process, as compared to the approach of Milwitzky and Cook [15], since the LG can be uniformly modeled as a 2 DOF system throughout the whole landing, including its initial stage and — if necessary — rebounds. The total strut force and the component forces depend directly on the strut axial stroke s,

$$s = z_1 - z_2.$$

The pneumatic force F_a in Eq. 6.3 is modeled in accordance with the polytropic law for compression of gases,

$$F_a(s) = p_0 A_a \left(\frac{V_0}{V_0 - sA_a}\right)^n, \tag{6.4}$$

while the hydraulic force F_h is modeled in the standard way [15] as

$$F_h(\dot{s}) = \mathrm{sign}(\dot{s})\frac{1}{2}\frac{\rho A_h^3}{C_d^2 A_o^2}\dot{s}^2. \tag{6.5}$$

symbol	numerical value	explanation
A_a	$1.385\ 10^{-3}$ m^2	pneumatic area
p_0	1.028 MPa	initial air pressure in the upper chamber
V_0	$171\ 10^{-6}$ m^3	initial air volume in the upper chamber
n	1.1	polytropic exponent for the air compression process
ρ	872.6 kg/m^3	density of hydraulic fluid (Aeroshell 41)
A_h	$1.018\ 10^{-3}$ m^2	hydraulic area
A_o	$A_{o(min)} \leq A_o$ $A_o \leq A_{o(max)}$	cross-sectional area of the discharge orifice
$A_{o(min)}$	5 mm^2	technological lower bound on A_o
$A_{o(max)}$	40 mm^2	technological upper bound on A_o
C_d	0.6	orifice discharge coefficient
C_f	559 N	dry friction coefficient
l_d	$500\ 10^{-6}$ m	delimiting force acting interval

Table 6.1: Symbols used in Eq. 6.4 to Eq. 6.7 [93, 15, 94].

The friction occurring in the strut is assumed to be dry friction only [15] and is modeled by

$$F_f(\dot{s}) = C_f \frac{2}{\pi} \arctan(10^4 \dot{s}), \tag{6.6}$$

where the inverse tangent function was used to assure smooth variations of the friction force at the turning points and to enable numerical integrations of the equations of motion. The delimiting force F_d prevents excessive elongation of the strut and attempts to model the actual force occurring on the strut delimiter. It acts within the last l_d of the fully elongated strut and is modeled by a simple spring force as

$$F_d(s) = p_0 A_a \min\left(\frac{s - l_d}{l_d}, 0\right), \tag{6.7}$$

where the coefficient $p_0 A_a$ has been chosen to obtain equilibrium at full elongation: $F_d(0) + F_a(0) = 0$. Possible oscillations of a fully elongated strut are damped directly by the hydraulic force F_h.

The symbols used in Eq. 6.4 to Eq. 6.7 are explained in Tab. 6.1. The numerical values of p_0, V_0 and of the dry friction coefficient C_f have been obtained by numerical fitting of LG quasi-static compression data. The trimming bounds on A_o, which is the controlling parameter, are chosen arbitrarily to model real technological constraints. Notice that the following simplifying assumptions concerning the friction have been made:

- The dynamic friction equals the quasi-static friction.
- The strut friction is not considerably affected by the normal loading occurring due to tire friction in the first milliseconds of the landing process at

the wheel axle. This is an oversimplification in the case of a cantilever-type LG but can be legitimate in the case of levered trailing arm gears.

Accuracy of the model can be partly verified by comparison of calculated forces and displacements with the forces and displacements measured in tests of a real I-23 nose LG, passive version. Institute of Aviation (Warsaw, Poland) has made available two sets of measurement data suitable for the comparison:

1. mass $m = 422$ kg, sinking velocity $v_0 = 2.93$ m/s, lift factor $L = 0.667$;
2. mass $m = 422$ kg, sinking velocity $v_0 = 3.52$ m/s, lift factor $L = 1$.

The first case corresponds to the highest-energy design landing conditions, see Eq. 6.2, while the second is even more demanding. Fig. 6.3 compares the calculated and measured tire forces F_G, while Fig. 6.4 and Fig. 6.5 compare the calculated and measured aircraft and tire displacements (z_1 and z_2). The discharge orifice area A_o was assumed to equal 17.43 mm^2, which is the optimum value in the case of a passive LG (see Section 6.3.1). Simulations and measurements agree well in the case of the tire force F_G, the first 150 ms of tire displacement z_2 and the first 100 ms of aircraft displacement z_1, which corresponds to the strut compression phase. However, there is an increasing discrepancy between the displacements calculated and measured in the strut decompression phase, which starts approx. 100 ms after the impact. The discrepancy suggests additional factors coming into play during the strut decompression phase (possibly recoil orifices and hydraulic oil foaming), which cannot be thus modeled using a constant recoil orifice area. Nevertheless, the strut compression phase seems to be modeled reliably; hence all considerations of this paper concerning the peak strut force F_{peak} and the proposed control strategies are valid.

6.3 Control strategies

It is assumed that the landing scenario is fully defined by two basic parameters: (1) total landing mass per strut m, (2) initial strut sinking velocity v_0. Their ranges are given in Eq. 6.2, their distributions in Section 6.4.2. The common objective of all the investigated control strategies is to minimise the peak strut force F_{peak} occurring during the landing. The evolution of the total strut force F_S is fully determined by the control parameter, which is area A_o of the discharge orifice. Essentially, there are three control strategies possible:

- *Passive LG* (PLG), i.e. no control. the orifice area A_o is constant and cannot be adjusted to particular landing conditions. Nevertheless, its preset constant value is optimized to mitigate the peak strut force occurring at the highest-energy landing conditions (maximum design landing mass and sinking velocity).

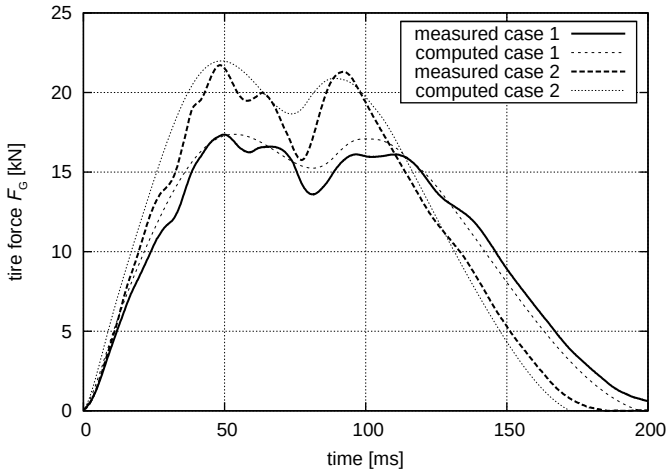

Figure 6.3: Measured and computed tire force F_G, passive LG: test case 1 ($m = 422$ kg, $v_0 = 2.93$ m/s, $L = 0.667$); test case 2 ($m = 422$ kg, $v_0 = 3.52$ m/s, $L = 1$).

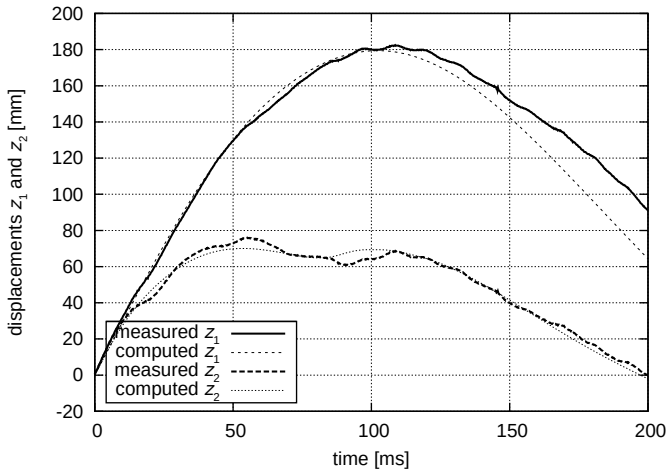

Figure 6.4: Measured and computed displacements of aircraft z_1 and tire z_2, passive LG, test case 1 ($m = 422$ kg, $v_0 = 2.93$ m/s, $L = 0.667$).

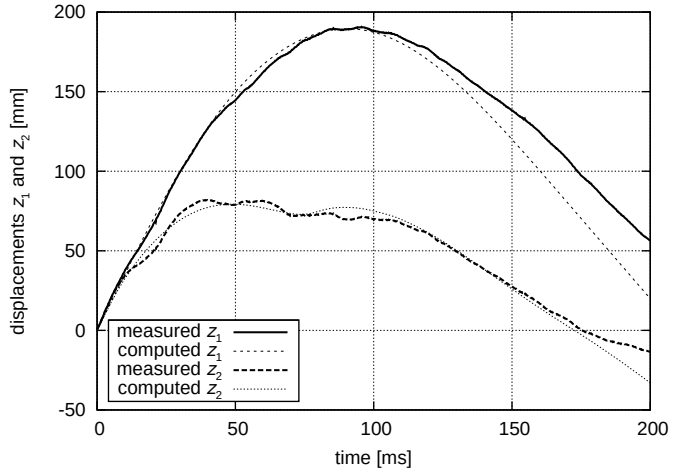

Figure 6.5: Measured and computed displacements of aircraft z_1 and tire z_2, passive LG, test case 2 ($m = 422$ kg, $v_0 = 3.52$ m/s, $L = 1$).

- *Semi-active LG* (SLG). The orifice area A_o is optimally set directly before each landing, based on the actual sinking velocity v_0 and/or mass m, which have to be measured or known in advance. A_o remains constant during the landing process, which makes the strategy relatively easy to implement, since no quick closed control loops are necessary.

- *Active LG* (ALG). The orifice area A_o changes continuously during the landing process, according to a strategy defined by the actual values of the initial sinking velocity v_0 and/or mass m, which have to be measured or known in advance. This strategy potentially yields the highest improvement, but requires quick closed control loops and accurate real-time measurement data, which may result in instabilities.

The strategies apply to the strut compression phase only. During the decompression phase, recoil orifices take effect instead of the main discharge orifice, the numerical model has thus to be modified and the optimization goal redefined. However, as the (to-be-minimized) peak strut force F_{peak} occurs within the strut compression phase, modeling of the decompression phase is outside the scope of this paper.

To apply the active or the semi-active control strategy, as defined above, the actual landing scenario has to be at least partially known in advance. In real conditions, the sinking velocity v_0 can be relatively easy measured just before the touchdown by a dedicated sensor (e.g. ultrasonic, one per LG). However, it may not be possible to know the exact actual value of the total landing mass per strut m. Therefore, to asses the importance of the knowledge of the mass, altogether five cases have been considered:

1. Passive LG (PLG);
2. Semi-active LG (SLG): both v_0 and m are known before landing;
3. Velocity-driven semi-active LG (VD-SLG): only v_0 is known before landing;
4. Active LG (ALG): both v_0 and m are known before landing;
5. Velocity-driven active LG (VD-ALG): only v_0 is known before landing.

To investigate and assess the strategies, the equations of motion Eq. 6.1 had to be solved numerically, which was done with explicit methods and the time step 5 μs or 50 μs (active strategies). The peak strut forces computed at 5 μs and 50 μs differed by approx. 0.1 % – 0.2 %, which is acceptable to compare the strategies reliably.

6.3.1 Passive LG

The pre-set constant discharge orifice area A_o^{PLG} has to be chosen to minimize the peak force occurring during the highest-energy design landing scenario. Fig. 6.6 shows the dependence of the peak strut force $F_{peak}^{PLG}(m_{max}, v_{0(max)}, A_o)$ on the discharge orifice area A_o. The left slope corresponds to the decreasing peak of the hydraulic force, while the right slope corresponds to the increasing peak of the pneumatic force. The minimum value of 17 021 N has been found at $A_o^{PLG} = 17.43$ mm^2, where both peaks are equal. The corresponding computed tire peak force equals 17 374 N, which is relatively very close to the measured value of 17 400 N (see Fig. 6.3). Thus, the maximum design strut force was assumed to be $F_{max} = 17\ 021$ N. The optimum discharge orifice area for a passive LG is $A_o^{PLG} = 17.43$ mm^2.

$$\begin{array}{rcl} F_{max} & = & 17\ 021 \text{ N}, \\ A_o^{PLG} & = & 17.43 \text{ mm}^2. \end{array} \tag{6.8}$$

6.3.2 Semi-active LG

A graph of F_{peak} in dependence on the orifice area A_o (similar to that shown in Fig. 6.6) can be drawn for each combination of the landing mass m and the vertical velocity v_0. Therefore, if both m and v_0 are known or measured just before the touchdown, the discharge orifice area A_o can be set to the optimum value $A_o^{SLG}(m, v_0)$, within the technological bounds $A_{o(min)}$ and $A_{o(max)}$ (Tab. 6.1), which yields the *technologically attainable* minimum peak force

$$F_{peak}^{SLG}(m, v_0) := F_{peak}(m, v_0, A_o^{SLG}(m, v_0)).$$

This is substantially advantageous to the passive LG, which is optimized only for the highest-energy design landing scenario.

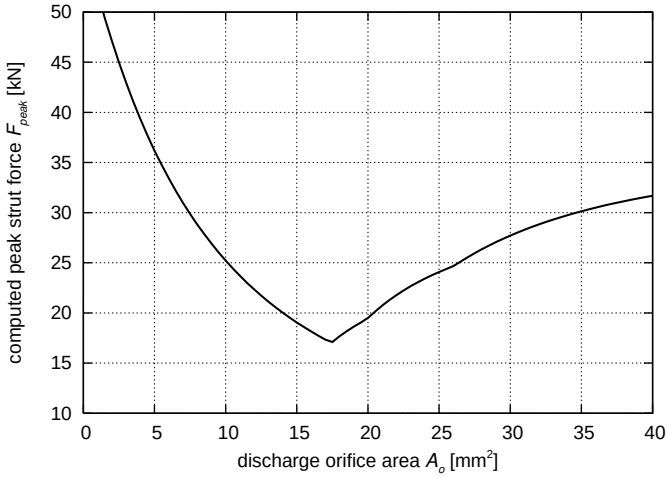

Figure 6.6: Passive LG: Computed dependence of the peak strut force F_{peak} on the discharge orifice area A_o at the highest-energy design landing scenario ($m = 422$ kg and $v_0 = 2.93$ m/s).

Fig. 6.7 shows the dependence of the computed optimum discharge orifice area $A_o^{SLG}(m, v_0)$ on the landing conditions. At standard landing conditions (low sinking velocity), the optimum orifice area A_o^{SLG} considerably exceeds the constant value A_o^{PLG} used in the passive LG, Eq. 6.8. Hence, at the same landing conditions, the peak strut force in the semi-active LG can be expected to be considerably lower than in the passive LG. The relative improvement is shown in Fig. 6.8, which plots the ratio of the peak force in SLG to the peak force in PLG at the same landing conditions. There is obviously no improvement in the highest-energy landing scenario, since the SLG amounts then to the PLG. The effect of the semi-active control becomes apparent as the mass or sinking velocity decreases. However, at low sinking velocities, the advantage of the SLG over the PLG tends to diminish, which is due to the effect of the initial stiffness of the air spring and the lift force: the landing energy is too low to compress considerably the strut and trigger the hydraulic force. Thus most of the vertical displacement is the tire deflection, and it is not possible to take advantage of the semi-active control scheme.

6.3.3 Velocity-driven semi-active LG

The semi-active control strategy requires both the landing mass m and the sinking velocity v_0 to be known before landing. However, in practice only the velocity v_0 can be relatively easy measured and the mass m has to be estimated. To asses the importance of the exact knowledge of the mass, the limiting case of no mass knowledge can be tested. The discharge orifice area A_o has then to be chosen to minimize the peak strut force in the corresponding highest-energy landing

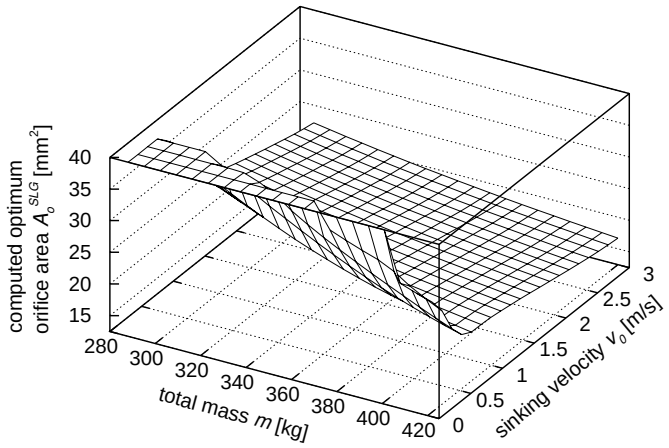

Figure 6.7: Semi-active LG: Computed dependence of the optimum discharge orifice area on the total mass m and sinking velocity v_0.

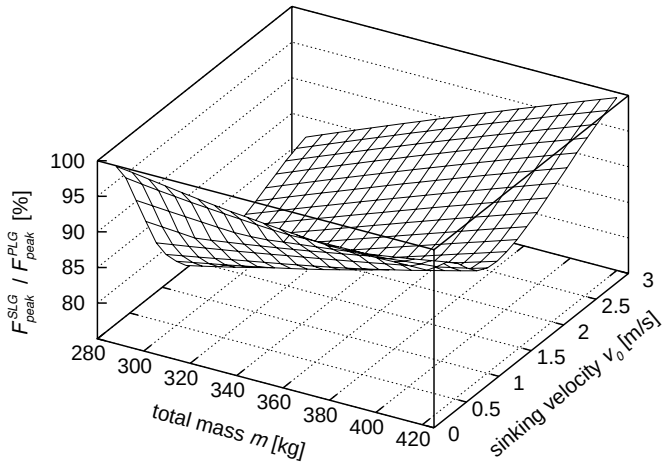

Figure 6.8: SLG compared to PLG, relative improvement: Computed ratio of the peak strut force in the optimally controlled SLG to the peak strut force in PLG at the same landing conditions, in dependence on the total mass m and sinking velocity v_0.

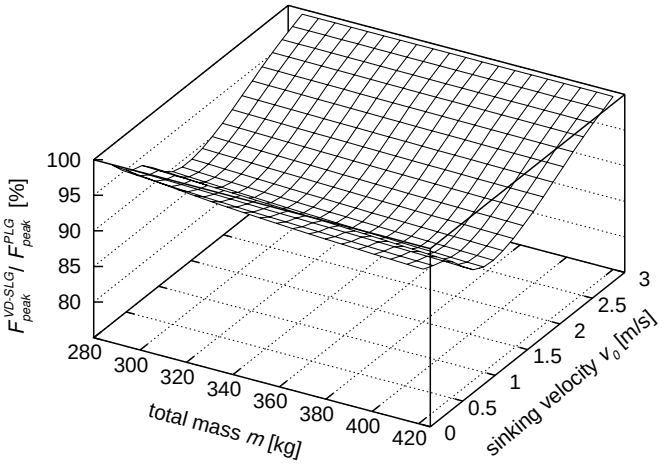

Figure 6.9: VD-SLG compared to PLG, relative improvement: Computed ratio of the peak strut forces in the optimally controlled VD-SLG and PLG at the same landing conditions, in dependence on the total mass m and sinking velocity v_0.

scenario (i.e. at the highest mass m_{max}),

$$A_o^{VD\text{-}SLG}(v_0) := A_o^{SLG}(m_{max}, v_0).$$

The performance of the VD-SLG must thus suffer, compared to the SLG. However, as Fig. 6.7 shows, the optimum orifice area is influenced more by the landing velocity than by the mass. A comparison of the performances of the VD-SLG and PLG is shown in Fig. 6.9, which may be compared with Fig. 6.8. At low sinking velocities the same effect of the initial stiffness of the air spring occurs.

6.3.4 Active LG

In an actively controlled LG the discharge orifice area A_o is actively modified during the strut compression phase. The equations in Section 6.2 directly relate the total strut force F_S to A_o by:

$$F_S = F_a + F_f + F_d + \frac{1}{2}\text{sign}(\dot{s})\frac{\rho A_h^3}{C_d^2 A_o^2}\dot{s}^2.$$

Hence, if instantaneous control is assumed, an obvious method to keep the total strut force F_S at a desired limit value F_{limit} is to actively set A_o during the compression phase according to

$$A_o^2 = \begin{cases} A_{o(max)}^2 & \text{if } F_{limit} \le F_a + F_f + F_d \\ \max\left(A_{o(min)}^2, \min\left(A_{o(max)}^2, \frac{\rho}{2}\frac{A_h^3}{C_d^2}\frac{\dot{s}^2\,\text{sign}(\dot{s})}{F_{limit}-F_a-F_f-F_d}\right)\right) & \text{otherwise,} \end{cases} \tag{6.9}$$

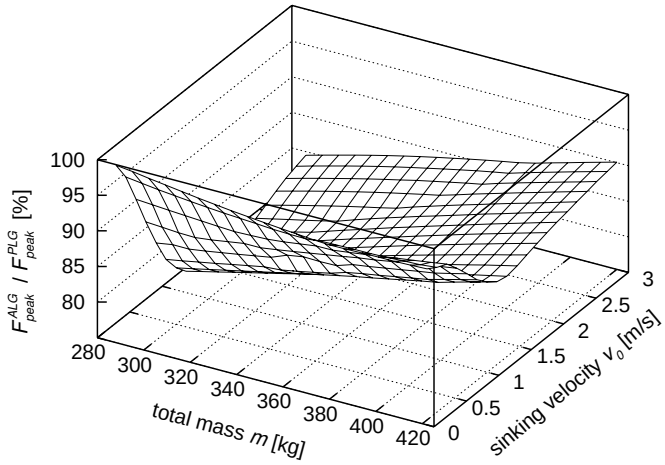

Figure 6.10: ALG compared to PLG, relative improvement: Computed ratio of the peak strut forces in the optimally controlled ALG and PLG at the same landing conditions, in dependence on the total mass m and sinking velocity v_0.

where the first value serves the instantaneous minimization of F_S in case it inevitably exceeds F_{limit}. According to Eq. 6.9, at the very beginning of the strut motion, when the total strut force F_S is still low, the discharge orifice area A_o is set to $A_{o(min)}$ and stay so until F_S attains F_{limit}. Thereafter A_o is actively controlled within the given limits until the decompression phase begins. Therefore, the active approach of Eq. 6.9 requires optimization of the peak force with respect to only one parameter F_{limit}, which has to be performed for each landing conditions defined by m and v_0.

However, Eq. 6.9 is only an approximation to the optimum active control. A finer control strategy applied at the beginning of the compression phase, before attaining F_{limit}, could further increase the efficiency of the strut and reduce the peak force. To come closer to the optimum strategy, the strut can be softened at the beginning of the impact by setting the initial discharge orifice area to a given value $A_{o(ini)}$. The active control of Eq. 6.9 begins first when the force limit F_{limit} has been attained. In a real LG it will also reduce the initial tire–runway friction, allow for a gradual wheel spin-up and reduce the spring-back effects. This resulted in optimization with respect to two parameters: (1) initial area of the discharge orifice $A_{o(ini)}$; (2) desired strut force limit F_{limit}, which triggers and controls the phase of active control according to Eq. 6.9.

Fig. 6.10 shows the relative improvement in comparison to the PLG. The advantage of the ALG over SLG (Fig. 6.8) at standard landing conditions (low sinking speed) amounts to not more than 3 % and is rather insignificant. However, at the highest-energy landing conditions it attains the maximum of approx. 9 %, which is significantly better than the semi-active strategy.

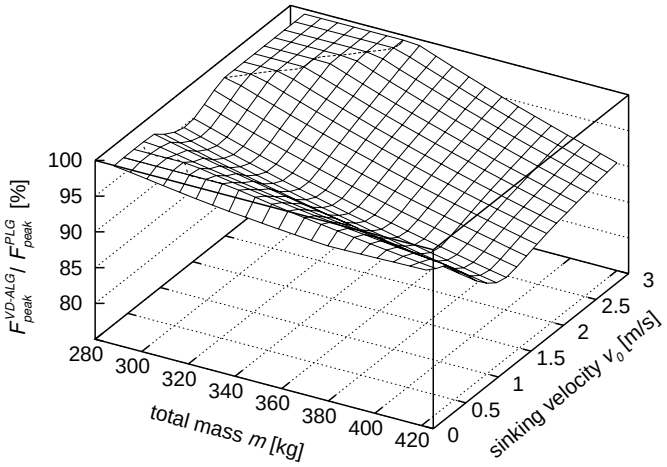

Figure 6.11: VD-ALG compared to PLG, relative change: Computed ratio of the peak strut forces in the optimally controlled VD-ALG and PLG at the same landing conditions, in dependence on the total mass m and sinking velocity v_0; the contour line marks the 100 % level.

6.3.5 Velocity-driven active LG

Similarly to VD-SLG, a VD-ALG can be considered to study the limiting case of the practical scenarios when the mass m is not known before the landing and should be thus assumed to be the maximum m_{max}:

$$\begin{aligned} A_{o(ini)}^{VD\text{-}ALG}(v_0) &:= A_{o(ini)}^{ALG}(m_{max}, v_0), \\ F_{limit}^{VD\text{-}ALG}(v_0) &:= F_{limit}^{ALG}(m_{max}, v_0). \end{aligned}$$

Fig. 6.11 compares the performances of the VD-ALG and PLG. At low landing mass the peak force can be even *higher* than in the standard PLG, which renders the pure VD-ALG strategy useless.

6.3.6 Example simulations

All sample simulations presented in this section are based on the landing conditions $m = 350$ kg and $v_0 = 1.5$ m/s, which are taken as examples and lie approximately in the middle of the design range (see Eq. 6.2).

Fig. 6.12 compares the computed strut forces in the PLG and SLG during the first 200 ms of the landing process. Fig. 6.13 shows the forces in the ALG along with the details of the applied active control. Two small temporary decreases of the total strut force at approx. 60 ms and 100 ms are results of attaining the lower limit $A_{o(min)}$ imposed on the orifice area (see the bottom plot of the active control). Notice how the pneumatic and hydraulic force peaks, which are unequal in the PLG, are made equal in the SLG and additionally leveled in the

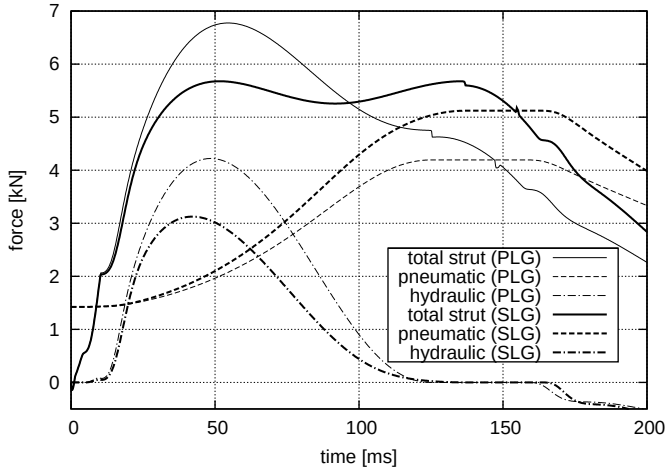

Figure 6.12: Comparison of computed pneumatic, hydraulic and total strut forces in PLG and SLG for $m = 350$ kg and $v_0 = 1.5$ m/s.

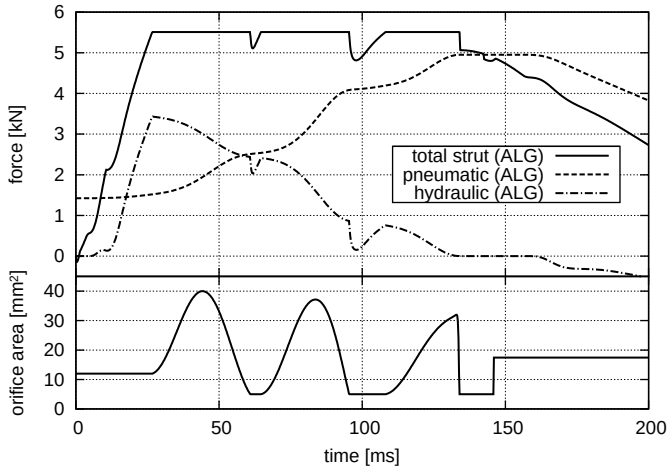

Figure 6.13: Computed pneumatic, hydraulic and total strut forces in ALG, and active control for $m = 350$ kg and $v_0 = 1.5$ m/s.

ALG. Further reduction of the peak strut force is possible only by increasing the force growth rate in the first 25 ms by decreasing the initial orifice area $A_{o(ini)}$. However, in a real LG this would considerably increase the tire–runway friction and the spring-back effect. It would also require a substantial increase of the orifice area upper limit $A_{o(max)}$ to maintain the constant force level in the subsequent 25 ms (see the first peak of the active control in Fig. 6.13). The plots of the strut force versus strut deflection for the four considered control strategies are compared in Fig. 6.14.

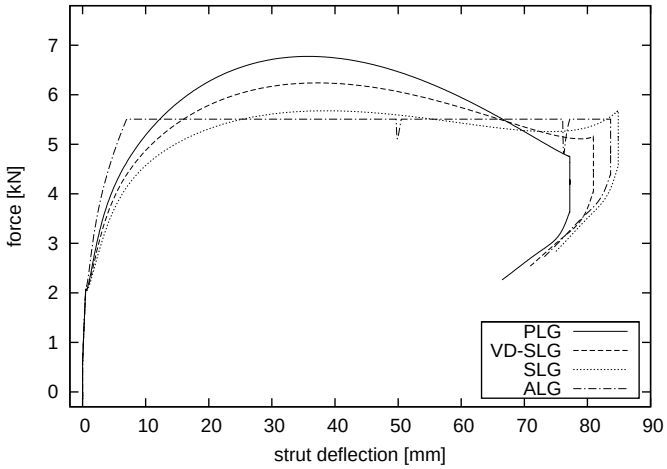

Figure 6.14: Strut force versus deflection in PLG, VD-SLG, SLG and ALG for $m = 350$ kg and $v_0 = 1.5$ m/s.

6.4 Potential for improvement

6.4.1 Air spring influence

A typical landing scenario involves a low sinking velocity, see Fig. 6.15. However, the investigated control strategies reveal improvements only for medium-to-high sinking velocities, see Fig. 6.8, 6.9 and 6.10. This is due to the effect of the pre-stressed air spring and the lift force: to compress the strut further than the delimiting force acting range $l_d = 0.5$ mm, the strut force has to overcome the joint effect of the pneumatic and friction forces, which amounts to 1983 N and is comparable to the peak force at $v_0 = 0$ m/s, which was computed to be 1993 N – 2179 N, depending on the mass. Therefore, at low sinking velocities the strut is being barely compressed and there is practically no hydraulic force to be controlled. As a result no strategy based on hydraulic force control can yield improvement at low sinking velocities. This is, however, not necessary, since the static runway loading is considerably higher than the landing peak force at low sinking velocities. This is due to the lift factor $L = 0.667$, which occurs in Eq. 6.1 and disappears in static or taxiing conditions. Therefore, the (semi)-active control strategies can in fact be considered necessary only in the cases when the peak force in the PLG is *significant*, i.e. exceeds the static loading, $F_{peak}^{PLG}(m, v_0) > mg$. This occurs at higher sinking velocities only; the limiting velocity ranges from 0.54 m/s to 0.85 m/s, depending on the landing mass m.

6.4.2 Mean and median peak strut force

Fig. 6.8 to Fig. 6.11 compare the performance of the discussed LG types for each design landing condition separately. An overall comparison is possible by sta-

sinking velocity v_0 [m/s]	cumulative occurrences	sinking velocity v_0 [m/s]	cumulative occurrences
0.00	1000.0	1.54	63.0
0.15	994.6	1.70	33.8
0.31	925.6	1.85	17.7
0.46	811.3	2.00	9.7
0.62	669.6	2.16	4.7
0.77	518.8	2.31	2.5
0.93	380.2	2.47	1.6
1.08	260.3	2.62	1.0
1.23	172.9	2.78	0.6
1.39	108.4	2.93	0.3

Table 6.2: Assumed cumulative occurrences of sinking velocities per 1000 landings.

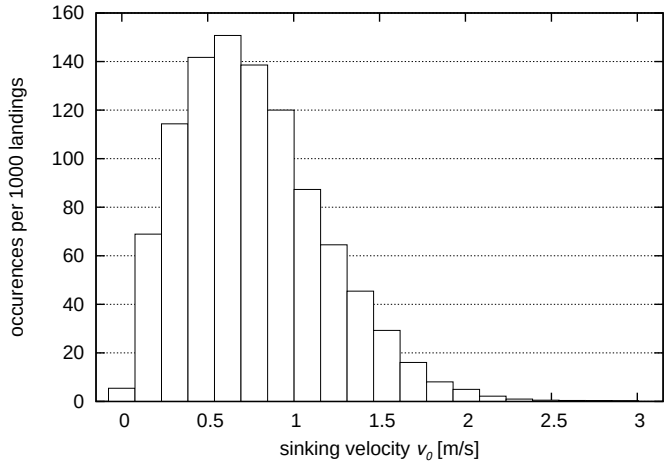

Figure 6.15: Assumed occurrences of sinking velocities per 1000 landings.

tistical means if the probability distributions of landing conditions are defined. The initial sinking velocity v_0 and the total mass m are assumed to be independent. To ease the statistical computations, their ranges Eq. 6.2 have been discretized into 20 equally spaced values. The distribution of the landing mass has been assumed to be uniform in the whole range of 288 kg – 422 kg. The assumed discretized distribution of the initial sinking velocity v_0 is listed in Tab. 6.2 (cumulative occurrences) and illustrated in Fig. 6.15 (occurrences).

Tab. 6.3 compares the performances of the four LG types in terms of the expected and median peak strut forces. Two cases have been considered, unconditional and conditional:

1. All landing conditions have been taken into accounts, *unconditional* $E\left[F_{peak}\right]$

LG type	peak strut force		relative improvement	
	expected value [kN]	median value [kN]	expected value [%]	median value [%]
Case 1: unconditional (all landing scenarios)				
PLG	3.890	3.527	—	—
VD-SLG	3.618	3.284	7.0	6.9
SLG	3.386	2.992	12.9	15.2
ALG	3.331	2.959	14.4	16.1
Case 2: conditional ($F_{peak}^{PLG} > mg$)				
PLG	4.962	4.613	—	—
VD-SLG	4.565	4.232	8.0	8.3
SLG	4.202	3.878	15.3	15.9
ALG	4.106	3.790	17.2	17.8

Table 6.3: Performance of four LG control strategies, a statistical comparison. Case 1: unconditional values (all landing scenarios); Case 2: conditional values (landings with the PLG peak strut force exceeding the static load.

and median $\left[F_{peak}\right]$ have been computed for the four control strategies considered.

2. Only landings with the PLG peak strut force exceeding the static load have been taken into account. This case reports on the statistical reduction of *significant* peaks and leads to *conditional* probability distributions, expected values and medians

$$E\left[F_{peak} \mid F_{peak}^{PLG} > mg\right], \quad \text{median}\left[F_{peak} \mid F_{peak}^{PLG} > mg\right].$$

6.4.3 Safe sinking velocity range

The described control strategies decrease the peak strut force, hence allow the sinking velocity range to be extended even beyond $v_{0(max)} = 2.93$ m/s without exceeding the peak strut force limit F_{max}. Fig. 6.16 compares, in terms of the landing mass m at three control strategies (PLG, SLG, ALG), the maximum safe sinking velocities $\hat{v}$, which are defined by an implicit relation $F_{peak}(\hat{v}, m) = F_{max}$. The velocity-driven semi-active strategy (VD-SLG) has been skipped, since it assumes no information about the landing mass m and is hence bound by $v_{0(max)} = 2.93$ m/s, which occurs at m_{max}.

6.5 Experiment

The obtained results of numerical simulation were verified experimentally by means of a small laboratory demonstrator. The objective was a comparative

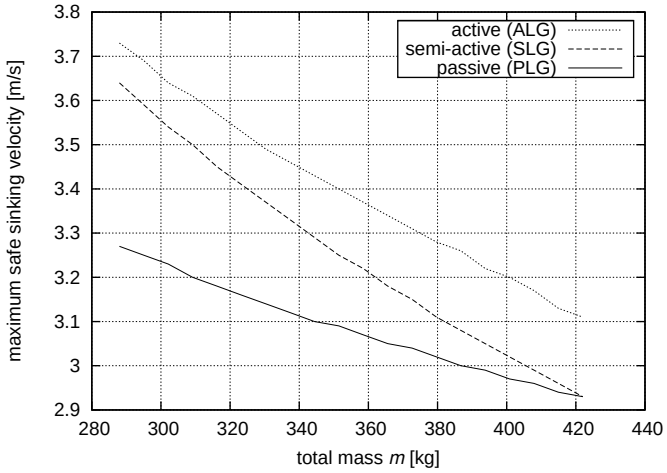

Figure 6.16: Maximum safe sinking velocity at three control strategies in terms of the total landing mass.

study of operation of the adaptive landing gear model in the *passive*, *semi-active* and *active* control modes, in order to:

1. prove feasibility of the proposed control strategies and
2. assess experimentally the potential reduction of the peak force, which can be achieved thanks to the introduction of adaptive landing gears.

6.5.1 Testing stand

The adaptive landing gear was substituted in the experiment with an intentionally designed, lab-scale Adaptive Impact Absorber (AIA). The adaptability of the AIA was realised by means of a variable viscous damping force, obtained via introduction of magnetorheological (MR) fluid. The AIA was composed of a magnetorheological damper and a coil spring, see Fig. 6.17 (left). A dedicated control unit, developed in the FPGA technology, allowed generation of the desired level of the damping force (500 N – 2000 N) within rigorous time restrictions: the time delay was less than 4 ms.

The tests were performed on a small drop test device, designed and developed in laboratory, see Fig. 6.17 (right). The idea behind the stand was to realise the same scheme of impact excitation and thus to ensure its compatibility with full-scale testing stands being in use in large laboratories dedicated to testing of landing gears. Full-scale testing stands fix the landing gears under a drop mass, which simulates a respective part of the weight of an aircraft. The test procedure includes free falling drops from various heights to simulate different sinking velocities. In order to make the laboratory landing conditions more close to reality, struts are usually tested with variable circumferential speed of the

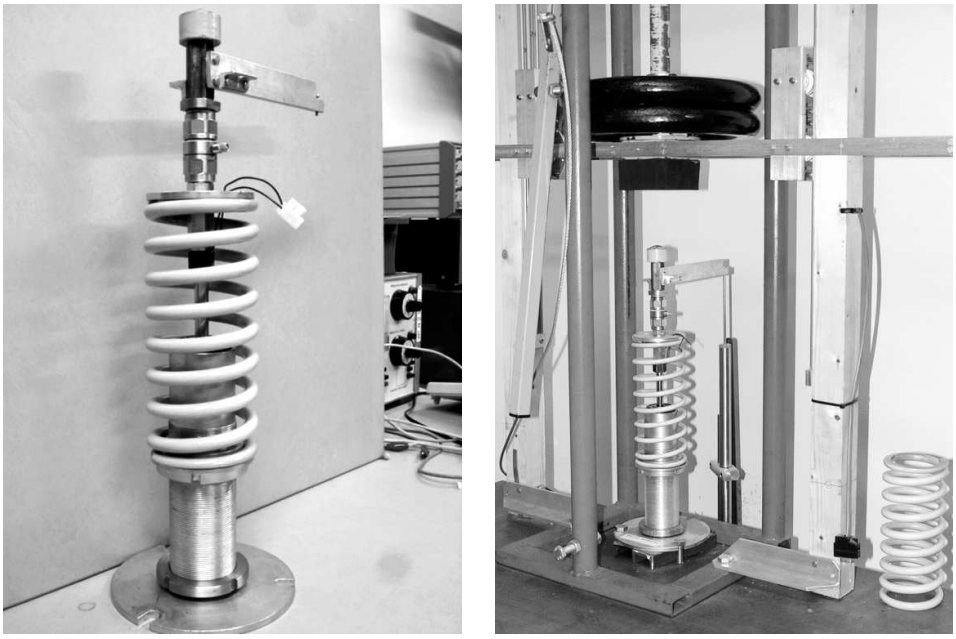

Figure 6.17: (left) Laboratory model of Adaptive Impact Absorber (AIA); (right) AIA mounted on the laboratory drop test rig.

wheel and, in the case of main landing gears, with various attitude angles (up to 15 degrees). Moreover, full-scale testing stands are equipped with a simulator of the lift force, which is able to generate the wing lift contribution to the landing process. For the purpose of the small, lab-scale experiment, the testing procedure was simplified in the following points:

1. The tests were conducted only in the vertical position of the adaptive impact absorber;
2. The tire of the landing gear was substituted by a bumper made of solid rubber;
3. The absorbing element was not mounted to the free falling mass but fixed in the vertical position on the foundation plate;
4. The lift force occurring during landing of aircraft was not simulated.

Due to the introduced simplifications, the friction forces generated on the sliding surfaces of the damper were much lower (and invariant) compared to real-world landing phenomenon, and the introduced rubber element had relatively stiffer characteristic in comparison to the characteristic of a pneumatic tire. Neglecting of the lift force had an influence on the inertial balance of the system. However, from mechanical point of view both systems were analogical (Fig. 6.18) and the time limitations for the control and actuation systems were the same.

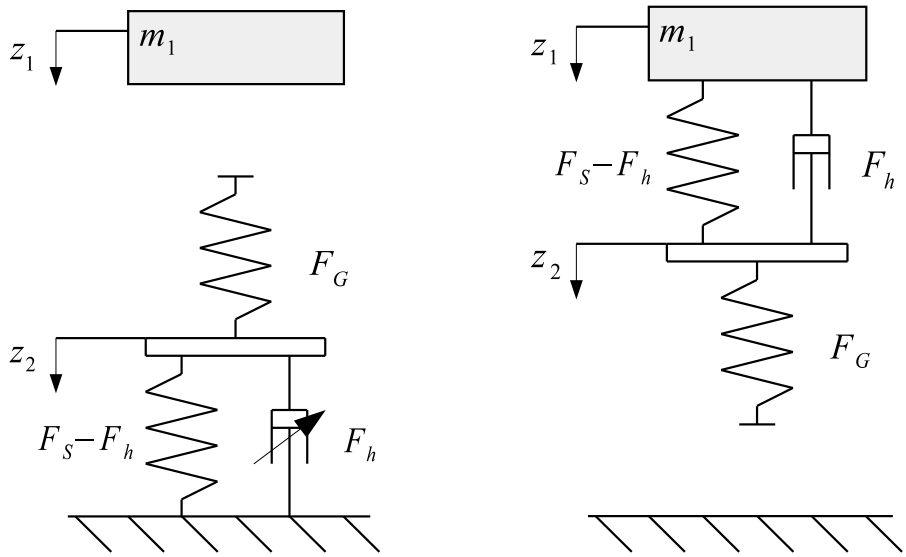

Figure 6.18: Comparison of schemes of testing stands: (left) lab-scale; (right) full-scale.

Therefore, it was assumed that the effectiveness of the proposed control strategies could be successfully tested and assessed.

The test program consisted of 567 drop tests. The procedure included drop tests in 63 cases of impact energy (0.6 J – 70 J), which are listed in Tab. 6.4. For each case the drops were conducted for three tested modes of operation and repeated treble in order to guarantee proper repeatability.

kinetic		sinking velocity [m/s]								
energy [J]		1.46	1.30	1.10	1.00	0.95	0.85	0.79	0.58	0.40
	67	71.41	56.62	40.54	33.50	30.23	24.20	20.91	11.27	5.36
	57	60.75	48.17	34.49	28.50	25.72	20.59	17.79	9.59	4.56
mass	47	50.09	39.72	28.44	23.50	21.21	16.98	14.67	7.91	3.76
[kg]	37	39.43	31.27	22.39	18.50	16.70	13.37	11.55	6.22	2.96
	27	28.78	22.82	16.34	13.50	12.18	9.75	8.43	4.54	2.16
	17	18.12	14.37	10.29	8.50	7.67	6.14	5.30	2.86	1.36
	7	7.46	5.92	4.24	3.50	3.16	2.53	2.18	1.18	0.56

Table 6.4: Kinetic energies used in tests.

6.5.2 Passive control strategy

Because of safety reasons, each conventional landing gear is designed to withstand touchdown impacts with critical energies (seven to ten knots sinking velocity and maximal weight for civil aviation [12]) without loosing its integrity and function-

ality. In order to satisfy this requirement, the optimisation process of the shock absorber must be focused on the landing scenarios with maximum impact energies instead of the most frequently occurring cases. An adequate methodology was chosen for the series of experimental tests of the AIA in the passive mode of operation.

As the first step of the experimental session, the model of adaptive landing gear was assumed to behave as a conventional, passive landing gear, and optimised to operate properly under the conditions of the maximum impact energy considered in this study. A constant level of the control signal was determined, which allowed to obtain the minimum magnitude of vertical dynamic force and to avoid collision between the structure and housing of the AIA device. Further on, the impact absorber was tested for the full range of the impact energies with the damping characteristics established for the passive mode. The dynamic force was measured and the peak value was stored to serve as a reference for assessment of the effectiveness of the proposed adaptive control strategies.

6.5.3 Semi-active control strategy

The semi-active control strategy was verified experimentally to asses the potential given by introduction of a simple adaptability scheme to landing gears. The control method was to adjust the damping characteristic of the AIA in each particular case of the impact. The optimal damping level was determined in dependence on the kinetic energy of the impact and the corresponding constant control signal was applied on the MR device in the AIA. The feed forward control of the system was thus defined as using an open loop the control only, and the control procedure included:

1. Determination of the sinking velocity and the mass of the falling object;
2. Automatic determination of the appropriate control signal on the basis of an implemented look-up table system;
3. Generation of the control signal and adaptation of the system.

Fig. 6.18 depicts the relative value of the measured peak dynamic force at the semi-active strategy in comparison with the peak force at the passive strategy. The improvement is the most significant at small impact velocities. An overall peak force reduction is approx. 20%.

6.5.4 Active control strategy

The active control strategy was realised in a closed loop control with the vertical acceleration of the structure as the feedback signal. The control sequence had three main stages of operation:

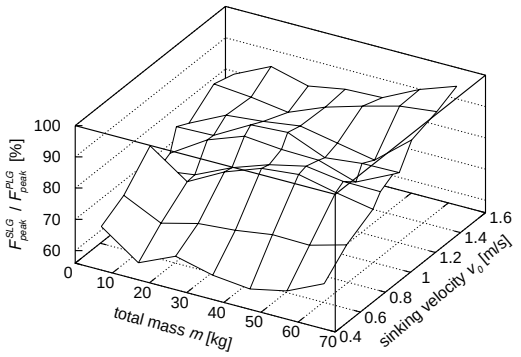

Figure 6.19: Semi-active control experimentally compared to passive control: ratio of measured peak dynamic forces.

1. Recognition of the energy of the impact;

2. Initial adaptation of the system;

3. Execution of the active control strategy.

The recognition of the impact energy was realised within 2 ms before the impact moment. To measure the sinking velocity a photo sensor was used, while the drop mass was assumed to be known. The objective of the closed loop control strategy was to adhere to a predefined value of the deceleration of the structure, which was determined in accordance to the recognised impact energy.

Fig. 6.20 depicts the relative value of the measured peak dynamic force in comparison with the peak force at the semi-active strategy. The approximate gain is on the level of 5%. The relative improvement increases with the impact energy, which is similar to the results obtained via numerical simulation [13, 95].

6.5.5 Example

Fig. 6.21 and 6.21 compare two measured hystereses (dynamic force F_S versus strut deflection s), which clearly illustrate the effects of the tested control strategies. The advantage of the semi-active and active modes over the passive is clear in both cases: the peak dynamic force has been considerably reduced. The advantage of the active strategy over the semi-active is much less pronounced. However, the active strategy, besides decreasing the peak dynamic force, which was the objective here, also significantly decreased the maximum piston strokes needed to complete the dissipation process. With the active strategy the energy is thus dissipated on a shorter distance. The displacements of the pistons were reduced by 15% on average, what significantly enlarges the energy dissipation potential of the AIA.

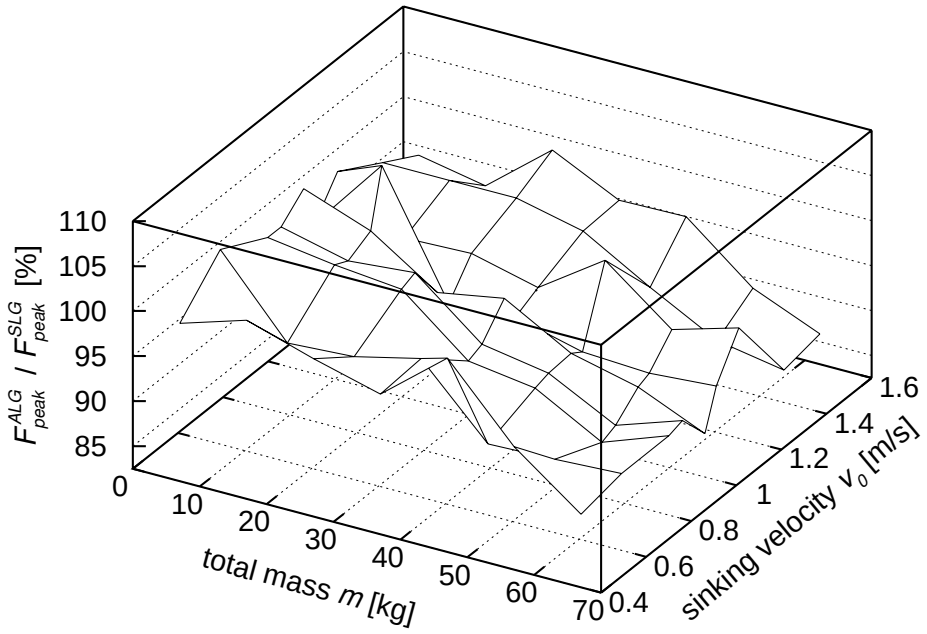

Figure 6.20: Active control experimentally compared to semi-active control: ratio of measured peak dynamic forces.

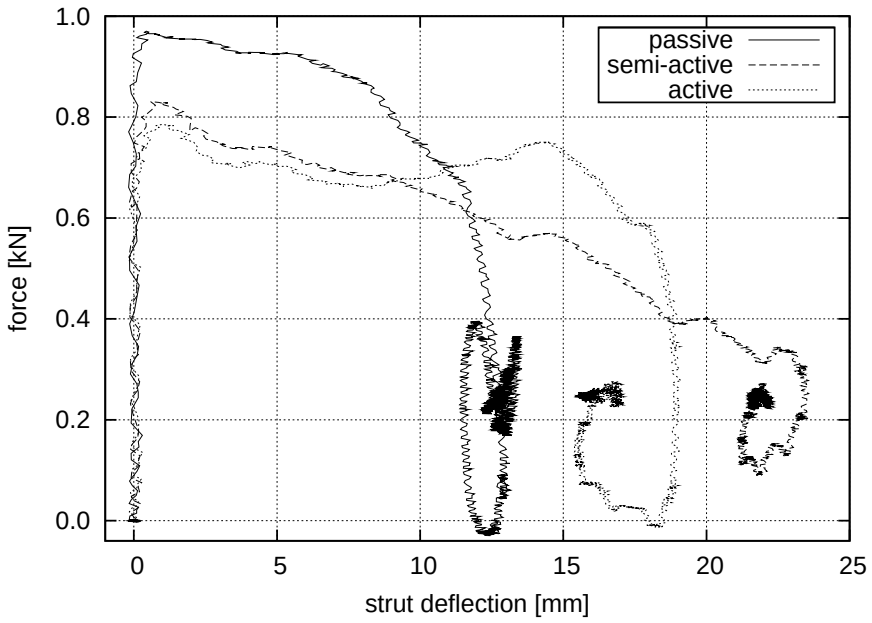

Figure 6.21: Experimental AIA hysteresis at passive, semi-active and active control strategies for $m = 37$ kg and $v_0 = 0.79$ m/s (drop height 32 mm).

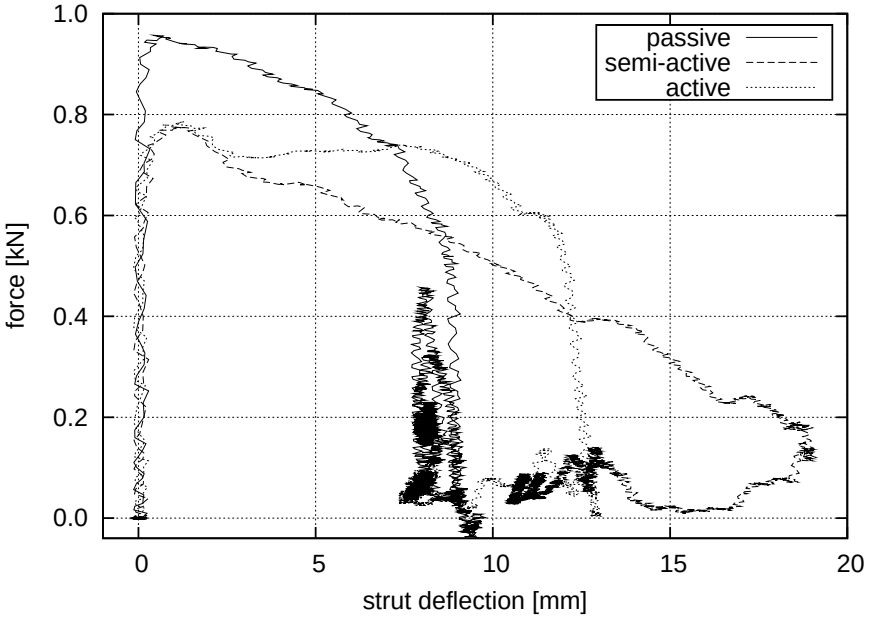

Figure 6.22: Experimental AIA hysteresis at passive, semi-active and active control strategies for $m = 27$ kg and $v_0 = 0.85$ m/s (drop height 37 mm).

6.6 Summary of Chapter 6

As it was presented in this chapter, the active control strategy presented in the previous chapter was successfully implemented in the laboratory tests and compared to the numerical results obtained for the case of an existing LG. The extended test program proved that the control strategy is repetitive in operation and effective in reduction of the maximal values of dynamic loads transferred on the protected structure. The results are in qualitative agreement with the results of simulations of the existing LG.

Chapter 7

Conclusions

7.1 Concluding remarks

The concluding part of this thesis firstly presents a brief summary of the chapters content and in the following part, emphasises the key original achievements of the study.

7.1.1 Summary

The objective of this thesis was to present a comprehensive analysis of a concept of Adaptive Impact Absorber based on magnetorheological fluids. As an example of application that is subjected to repetitive impact loadings, an aircraft landing gear was chosen. The general tasks analysed in the research were the questions of feasibility of the MR technology in the landing gears, and a special focus was directed to the problem of control methods in the face of impact phenomenon characterised by very short duration.

The thesis began with definition of the problem of adaptive impact absorption and its application fields. A brief discussion was presented over the methods of passive and active mitigation of the results of impacts. A special attention was given to the topic of active landing gears, and their drawbacks in comparison to semi-active solutions. The introductory part of the thesis was concluded with explanation of reasons for the analysis of adaptive landing gears actuated by MR fluid.

Chapter 2 discussed the area of the fundamental mechanics of magnetorheological fluids. It provided a literature review, which gave an overview of MRF modeling issues. The main part of the chapter presented a model used in this research for description of MRF in flow mode, where there was a significant fluctuation of magnetic flux density across the flow orifice. Finally, an experimental

verification of the results was presented on an intentionally fabricated device, which allowed the visualisation of the MRF under flow mode.

Chapter 3 was dedicated to an analysis of operation and formulation of modelling of a magnetorheological damper RD 1005-3 manufactured by LORD Corporation. That damper was the dissipative magnetorheological device used in the experiments for this research. An analytically formulated model of the device was proposed, which incorporated all of the physical effects occurring in the device. A special attention was given to the problem of modelling of MR fluid flow in the device.

Chapter 4 presented a discussion devoted to methods of accelerating the operation of the MR devices. The main sources of the time delays in the execution systems were analysed and a solutions proposed. The discussion contained a set of experimental examples for illustration of the described methods.

Chapter 5 discussed the possibilities and problems connected to implementation of the MR fluids in the adaptive landing gears. The objective of this chapter was to validate the concept of adaptive impact absorber based on MRF, by presenting the operation of an experimental system. The results of the research proved a potential feasibility of an ALG based on MRF.

Chapter 6 was devoted to a discussion of the gains that can be obtained as the result of introduction of the controllable AIA systems. Special attention here was given to estimation of the potential reduction of dynamic loadings that the aircraft is subjected to, thanks to employment of the semi-active aircraft landing gears.

7.2 Key achievements of the investigation

The first objective of the thesis was:

To derive and experimentally validate a model of flow of MR fluid in the conditions of significant field density variation.

This objective was achieved as the derivation of the fluid flow law presented in Chapter 2 was validated experimentally by means of an intentionally fabricated mockup. The results showed that the proposed model with incorporated influence of the magnetic fluid variation between the poles significantly improved the prediction results provided by the model. An additional very important achievement of this research was conducting of the visualisation experiment in order to deepen the understanding of the phenomena that occur in MR fluid under the flow mode.

An important achievement was also formulation of an analytically based model of MR damper. The formulation of the model was subsequent to deep analysis of effects, which affect the resulting reacting damping force generated

by the device. All the elements of the model were defined in a way that allow to interpret them physically. The model was identified on the basis of a set of intentionally designed measurement experiments in order to extract the values of all particular parameters governing the forces' definitions used in the modelling.

The original author's contribution was:

- building of the mockup for flow visualisation of the MR fluid
- formulation of a more precise flow law for MRF under non homogeneous magnetic field
- development of analytically based model of a magnetorheological damper and its experimental verification

The second general objective of this thesis was:

To develop and experimentally validate a control procedure for adaptive impact absorbers based on magnetorheological fluids.

The problem of feasibility assessment for the magnetorheological devices operated under the condition of impact is complex. However, in this thesis an analysis of main issues was presented and crucial points connected with the control problem of the AIA were solved and validated experimentally.

The feasibility of impact absorbers based on MRF for the adaptive landing gears depend strongly on the response time exhibited by the actuation system. An advanced control system must have been designed in such a way that allows the actuator to operate with time delays below 5 ms (0.005 s). Moreover, the developed control strategy must have been able to meet all of the specific requirements and constraints typical for aviation. The analysed control procedure primarily focused on the impact phase of an aircraft's landing as this was the crucial point in the assessment of the feasibility of the system.

The original author's contribution was:

- building of the stand for dropping tests able to demonstrate the concept of the adaptive landing gear
- proposing and programming of the controller for the system with the respond time equal or less than 0.005 s
- integration of the adaptively controlled ALG model based on MR damper RD-1005-3 and the developed controller
- experimental verification of the ALG concept
- numerical and experimental assessment of the potential improvement in the behaviour of landing gears on an example of an existing aircraft

7.3 Critical remarks

In this section I would like to discuss the topics that weren't in the scope of this thesis but are connected with employment of the MRF in landing gears.

Firstly, important problems of durability of magnetorheological devices were out of the scope of this study. The problem is new and important since the medium has properties which are innovative on the market. The classical oils are produced according to industry standards that assume a high level of purity. In accordance to aviation standards an allowable amount of particles in the hydraulic oil are 4 per cm^3, and the MRF contains more than 30% of hard particles by volume. This fact drives the designers to completely new technological challenges like development of a new class of sealing that would be resistant to wear caused by presence of hard pieces in the medium. The conventional sealing is relatively fast degraded by wearing action of the particles as tested in [96]. A tested damper was excited by 10 Hz sinusoidal excitation with stroke 2mm and the degradation of sealing was readable after 1M cycles, and after 1.75M cycles the leakage of the oil was significant (1 cycle was defined as 1 period of sinusoidal excitation). A proposition of a new method of sealing of the MR devices was presented in [48], which was based on the idea of employment of a permanent magnet in the sealing area for attraction of the metallic particles and prevent the destruction of the sealing protecting the oil against leaking.

Another problem that can have a significant influence on the durability of the MR devices is wearing of the magnetisable particles in the fluid. As it was shown in the durability test performed by Ulicny et al. [97], the iron particles undergo a degradation during operation in the devices. The particles, which have initially round shape, take irregular shapes in result of a loosing material. The reported influence on the device's responsibility was measured as 15% of reduction after 540 h of the test duration.

The proposed idea of application of the magnetorheological fluids to the aircraft landing gears provokes the discussion over topics that are directly related to this application. In the presently manufactured aeroplanes the design process is aimed at reaching the minimal weight of the machine in order to have the largest possible potential for carrying the payloads. The engineers are optimizing the structures to make them as light as possible and each particular saved kilogramme is important. In the case of the landing gears adapted to the MR technology its weight would be increased due to higher density of the MR fluid in comparison to the hydraulic oils utilised presently. Moreover, the actuation of the MR fluid requires installing of electromagnet coil, which also increases the total weight of the complete landing gear. However, the increase in the weight of the landing gear could be compensated by reduction of mass in other parts of the structure due to improved fatigue life of the aircraft.

Another important problem that relates to the application of the magnetorhe-

ological fluids in landing gears is sedimentation of the iron particles in the volume of the fluid [98]. The effect is caused by inequality of density between the iron particles and the carrier fluid, and results in concentration of the micro-particles in the bottom part of the volumes filed with MR fluids. The phenomenon significantly affects the responsiveness of the medium and causes malfunction of the devices. Reduction of the effect is obtained by employment of chemical additives, which increase the periods to the appearance of the non-homogeneity. The resistivity of devices on the effects of sedimentation depend strongly on the operation character. In the case of devices which are in movement, the mixing of the fluid is performed naturally e.g. in the case of the car suspensions. However, there exist a class of applications where the fluid is kept stable for long periods (seismic protection [52, 77]). For these applications the role of carrier fluids are played by gels, which exhibit higher values of viscosity and prevent the sedimentation process. In the case of landing gears, the magnetorheological fluids can be threatened by sedimentation as the devices are kept deactivated during long flights.

The next important issue that should be precisely analysed when a magnetorheological device is designed for a particular application is the heat transfer. There were experimental results presented [99, 100], which have concluded that the effectiveness and responsiveness of the MR devices decreases when a critical operational temperature has been exceeded. For that reason, the proper thermo-conductivity analysis of the devices is one of important tasks that should be performed on the design stage of the development. The problem is under intensive investigation in the recent years in the research centres around the world [101, 102, 103, 104].

References

[1] J. Holnicki-Szulc and L. Knap. Crash-worthiness of dynamically adaptive structures. In J. Rodellar, A. H. Barbat, and F. Casciati, editors, *Advances in structural control*. CIMNE, Barcelona, 1999. [cited at p. 3]

[2] J. Holnicki-Szulc, P. Pawłowski, and M. Wikło. High-performance impact absorbing materials - the concept, design tools and applications. *Smart Materials and Structures*, 12:461–467, 2003. [cited at p. 3]

[3] J. Holnicki-Szulc, editor. *Smart Technologies for Safety Engineering*. Wiley, 2008. in press. [cited at p. 3]

[4] A. Mróz, J. Holnicki-Szulc, and T. Karna. Mitigation of ice loading on off-shore wind turbines, feasibility study of semi-active solution. In *Proceedings of II ECCOMAS Thematic Conference on Smart Stuctures and Materials, SMART 05, 18-21 July, Lisboa, Portugal*, 2005. [cited at p. 3]

[5] A. Mróz and J. Holnicki-Szulc. Semi-active control of wind impact effects by means of pneumatic system. In *Proceedings of Nonsmooth/Nonconvex Mechanics with Applications in Engineering, Thessaloniki, Greece*, 2006. [cited at p. 3]

[6] G. Mikułowski and J. Holnicki-Szulc. Adaptive landing gear concept — feedback control validation. *Smart Materials and Structures*, 16:2146–2158, 2007. [cited at p. 3, 9, 11, 64]

[7] N. Jones and T. Wierzbicki. *Structural Crashworthiness*. London: Butterworths, 1983. [cited at p. 4]

[8] T. Wierzbicki and N. Jones. *Structural Failure*. New York: Wiley, 1989. [cited at p. 4]

[9] N. Jones and T. Wierzbicki. *Structural Crashworthiness and Failure*. London: Elsevier, 1993. [cited at p. 4]

[10] C. M. Harris and A. G. Piersol. *Harris' Shock and Vibration Handbook*. New York: McGraw-Hill, 2002. [cited at p. 4, 5]

[11] R. Gryboś. *Teoria Uderzenia w Dyskretnych Układach Mechanicznych*. Warszawa: Państwowe Wydawnictwo Naukowe, 1969. [cited at p. 4, 5]

[12] Federal Aviation Regulations (FAR), Part 23 — Airworthiness Standards: Normal, Utility, Acrobatic and Commuter Category Airplanes. [cited at p. 6, 88, 106]

[13] Ł. Jankowski and G. Mikułowski. Adaptive landing gear: optimum control strategy and improvement potential. In *ISMA 2006*, 2006. [cited at p. 6, 61, 108]

[14] N. S. Currey. *Aircraft landing gear design: principles and pratices.* AIAA, 1988. [cited at p. 6, 7]

[15] B. Milwitzky and F. E. Cook. Analysis of landing gear behaviour. Technical Report 1154, NACA, 1953. [cited at p. 6, 7, 55, 88, 89, 90, 139]

[16] H. G. Conway. *Landing gears design.* A Series of Textbooks published under the authority of the Royal Aeronautical Society. Chapman & Hall Ltd, 1958. [cited at p. 7]

[17] J. H. Walls. An experimental study of orifice coefficents, internal strut pressures, and loads on a small oleo-pneumatic shock strut. Technical note 3426, National Advisory Comittee for Aeroanutics, 1955. [cited at p. 7, 46]

[18] A. W. Hall, R. H. Sawyer, and J. M. McKay. Study of groud-reaction forces measured during landing impacts of a large airplane. Technical note 4247, National Advisory Committee for Aeronautics, May 1958. [cited at p. 7]

[19] W. Flügge. Landing-gear impact. Technical note 2743, National Advisory Committee for Aeronautics, October 1952. [cited at p. 7]

[20] J. E. Wignot, P. C. Durup, and M. A. Gamon. Design formulation and analysis of an active landing gear. AFFDL-TR-71-80 Vol. I, U.S. Air Force, 1971. [cited at p. 8]

[21] E. K. Bender, E. F. Berkman, and M. Bieber. A feasibility study of active landing gear. Affdl-tr-70-126, U.S. Air Force, 1971. [cited at p. 8]

[22] J. R. McGehee and H. D. Carden. A mathematical model of an active control landing gear for load control during impact and roll-out. Technical Note NASA TN D-8080, NASA Langley Research Center, February 1976. [cited at p. 8]

[23] J. R. McGehee and H. D. Carden. Analytical investigation of the landing dynamics of a large airplane with a load-control system in the main landing gear. Technical Report 1555, NASA, 1979. [cited at p. 8]

[24] I. Ross. Flightworthy active control landing gear system for a supersonic aircraft. Technical report, Hydraulic Research Textron, 1980. [cited at p. 8]

[25] I. Ross and R. Edson. An electronic control for an elecrtrohydraulic active control landing gear for the f-4 aircraft. Technical report, Hydraulic Research Textron, Inc, 1982. [cited at p. 8]

[26] J. R. McGehee and R. C. Dreher. Experimental investigation of active loads control for aircraft landing gear. NASA Technical Paper 2042, Langley Research Centre, 1982. [cited at p. 8]

[27] J. R. McGehee and D. L. Morris. Active control landing gear for ground load alleviation. In *AGARD Conf. Proc. 384, FMP Symposium*, 1984. Toronto. [cited at p. 8]

[28] W. E. Howell, J. R. McGehee, R. H. Daaugherty, and W. A. Vogler. F-106b airplane active control landing gear drop test performance. NASA Technical Memorandum 102741, Langley Research Centre, November 1990. [cited at p. 8]

[29] L. G. Horta, R. H. Daugherty, and V. J. Martinson. Modeling and validation of a Navy A6-Intruder actively controlled landing gear system. Technical Report TP-1999-209124, NASA, 1999. [cited at p. 8]

[30] L. G. Horta, R. H. Daugherty, and V. J. Martinson. Actively controlled landing gear for aircraft vibration reduction. Technical Paper NASA-99-ceas-lgh, NASA, 1999. [cited at p. 8]

[31] R. Freymann. Actively damped landing gear system. In *AGARD CP-484 Ref. 20, Proc. of the 71st Meeting of the AGARD Structures and Materials Panel*, October 1990. [cited at p. 8]

[32] Z. Lou, R. D. Ervin, C. B. Winkler, and F. E. Filisko. An electrorheologically controlled semi-active landing gear. SAE paper 931403, Langley Research Centre, January 1993. [cited at p. 8]

[33] H. Wentscher, W. Kortüm, and W. R. Krüger. Fuselage vibration control using semi-active front gear. In *Proceedings of the 81st meeting of the AGARD SMP Panel on "The design, Qualification and Maintenance of Vibration-Free Landing Gears"*, 1995. [cited at p. 8]

[34] X. Wang and U. Carl. Fuzzy control of aircraft semi-active landing gear system. In *Proc. of the 37th AIAA Aerospace Sciences Meeting and Exhibit*, January 1999. [cited at p. 8]

[35] W. Krüger. *Integrated Design Process for the Development of Semi-Active Landing Gears for Transport Aircraft.* PhD thesis, University of Stuttgart, December 2000. [cited at p. 8]

[36] G. L. Ghiringhelli. Testing of semiactive landing gear control for a general aviation aircraft. *AIAA Journal of Aircraft*, 37(4):606–616, 2000. [cited at p. 9]

[37] G. L. Ghiringhelli and S. Gualdi. Evaluation of a landing gear semi-active control system for complete aircraft landing. *Aerotecnica Missili e Spazio*, 83:21–31, January 2004. [cited at p. 9]

[38] Adaptive Landing Gears for Improved Impact Absorption, ADLAND, EU FP6 project IST-FP6-2002-Aero-1-502793-STREP. `http://smart.ippt.gov.pl/adland`. [cited at p. 9, 11]

[39] D. C. Batterbee, N. D. Sims, R. Staway, and Z. Wołejsza. Magnetorheological landing gear: 1. a design methodology. *Smart Material and Structures*, 16:2429–2440, 2007. [cited at p. 9]

[40] D. C. Batterbee, N. D. Sims, R. Staway, and M. Rennison. Magnetorheological landing gear: 2. validation using experimental data. *Smart Materials and Structures*, 16:2441–2452, 2007. [cited at p. 9]

[41] G. Gautschi. *Piezoelectric sensorics.* Springer Verlag, 2002. [cited at p. 9]

[42] Physik instrumente. www.physikinstrumente.com, 2008. [cited at p. 9]

[43] M. Kallio. *The elastic and damping properties of magnetorheological elastomers.* PhD thesis, VTT, 2005. [cited at p. 9]

[44] A. B. Flatau, D. L. Hall, and J. M. Schlesselman. Magnetostrictive vibration control systems. *Journal of Intelligent Material Systems and Structures*, 4:560–565, 1993. [cited at p. 9]

[45] F. T. Calkins, A. T. Flatau, and M. J. Dapino. Overview of magnetostrictive sensor technology. *Journal of Intelligent Material Systems and Structures*, 18:1057–1066, 2007. [cited at p. 9]

[46] J. D. Carlson. Introduction to magnetorheological fluids. In *SMART01 Workshop (Warsaw)*, 2001. [cited at p. 9]

[47] Lord corporation. www.lord.com, 2006. [cited at p. 9, 10, 70, 76]

[48] B. Sapiński. *Linear magnetorheological fluid dampers for vibration mitigation: Modelling, control and experimental testing.* AGH Uczelniane Wydawnictwa Naukowo-Dydaktyczne, 2004. [cited at p. 9, 10, 41, 114]

[49] B. Kavlicoglu, F. Gordaninejad, C. A. Evrensel, N. Cobanoglu, M. Xin, C. Heine, A. Fuchs, and G. Korol. A high-torque magnetorheological fluid clutch. In *Proceedings of SPIE Conference on Smart Materials and Structures*, San Diego, March 2002. [cited at p. 10]

[50] J. Huang, J. Q. Zhang, Y. Yang, and Y. Q. Wei. Analysis and design of a cylindrical magnetorheological fluid brake. *Journal of Materials Processing Technology*, 129:559–562, 2002. [cited at p. 10]

[51] F. Weber, G. Feltrin, and M. Motavalli. Passive damping of cables with mr dampers. *Materials and Structures*, 38:568–577, 2005. [cited at p. 10]

[52] G. Yang, B. F. Spencer Jr, J. D. Carlson, and M. K. Sain. Large-scale mr fluid dampers: Modelling and dynamic performance considerations. *Engineering Structures*, 24:309–323, 2002. [cited at p. 10, 16, 17, 115]

[53] E. O. Eriksen and F. Gordaninejad. A magnetorheological fluid shock absorber for an off-road motorcycle. *International Journal of Vehicle Design*, 2003. [cited at p. 10]

[54] F. Gordadinejad and S. P. Kelso. Fail-safe magnetorheological fluid dampers for off-highway, high-payload vehicles. *Journal of Intelligent Material System and Structures*, 11:395–406, 2000. [cited at p. 10]

[55] W. H. Li, H. Du, and N. Q. Guo. Design and testing of an mr steering damper for motorcycles. *International Journal of Advanced Manufactoring Technology*, 22:288–294, 2003. [cited at p. 10]

[56] W. H. Li and H. Du. Design and experimental evaluation of a magnetorheological brake. *International Journal of Advanced Manufacturing Technology*, 21:508–515, 2003. [cited at p. 10]

[57] T. Pranoto and K. Nagaya. Development on 2dof-type and rotary-type shock absorber damper using mrf and their efficiencies. *Journal of Materials Processing Technology*, 161:146–150, 2005. [cited at p. 11]

[58] G. Mikułowski and J. Holnicki-Szulc. Fast controller and control algorithms for mr based adaptive impact absorbers - force based control. *Machine Dynamics Problems*, 30:113–122, 2006. [cited at p. 11, 69, 81, 84, 85, 137]

[59] D. C. Batterbee, N. D. Sims, Z. Wolejsza, and A. Laffitte. Magnetorheological landing gear design: a feasibility study for small and large-scale aircraft. In *ISMA 2006*, 2006. [cited at p. 11]

[60] B. F. Spencer, S. J. Dyke, M. K. Sain, and J. D. Carlson. Phenomenological model for magnetorheological dampers. *Journal of engneering mechanics*, 123:230–238, 1997. [cited at p. 15]

[61] N. M. Wereley and Li Pang. Nondimensional analysis of semi-active electrorheological and magnetorheological dampers using approximate parallel plate models. *Smart Materials and Structures*, 7:732–743, 1998. [cited at p. 16, 23, 29, 41]

[62] F. D. Goncalves, M. Ahmadian, and J. D. Carlson. Investigating the magnetorheological effect at high flow velocities. *Smart Materials and Structures*, 15:75–85, 2006. [cited at p. 16]

[63] N. M. Wereley, J. Lindler, N. Rosenfeld, and Y-T Choi. Biviscous damping behaviour in electrorheological shock absorbers. *Smart Materials and Structures*, 13:743–752, 2004. [cited at p. 16]

[64] X. Wang and F. Gordaninejad. Flow analysis of field-controllable, electro- and magneto-rheological fluids using Herschel-Bulkley model. *Journal of Intelligent Material Systems and Structures*, 10:601–608, 2000. [cited at p. 16, 41]

[65] D. J. Peel and W. A. Bullough. Prediction of ER valve performance in steady flow. In *Proceedings of the Institution of Mechanical Engineers, Part C: Journal of Mechanical Engineering Science, 208, 253-266*, 1994. [cited at p. 16, 29]

[66] G. M. Kamath, M. K. Hurt, and N. M. Wereley. Anaysis and testing of Bingham plastic behaviour in semi-active eletrorheological fluid dampers. *Smart Materials and Structures*, 5:576–590, 1996. [cited at p. 16, 19, 23, 41]

[67] H. P. Gavin. Design method for high-force electrorheological dampers. *Smart Materials and Structures*, 7:664–673, 1998. [cited at p. 16, 29]

[68] N. C. Kovlicoglu, B. M. Kovlicoglu, Y. Liu, C. A. Evrensel, A. Fuchs, G. Korol, and F. Gordaninejad. Response time and performance of a high torque magnetorheological fluid limited slip differential clutch. *Smart Materials and Structures*, 16:149–159, 2007. [cited at p. 16]

[69] D. C. Batterbee, N. D. Sims, R. Stanway, and Z. Wolejsza. Design and performance optimisation of magnetorheological oleopneumatic landing gear. In *SPIE Anual International Symposium on Smart Structures and Materials: Damping and Isolation*, 2005. [cited at p. 16]

[70] Y. T. Choi, J. U. Choi, S. B. Choi, and N. M. Wereley. Constitutive models of electrorheological and magnetorheological fluids using viscometers. *Smart Materials and Structures*, 14:1025–1036, 2005. [cited at p. 16]

[71] V. L. Streeter and E. B. Wylie. *Fluid mechanics*. McGraw-Hill, 1979. [cited at p. 19]

[72] G. Astarita and G. Marrucci. *Principles of non-Newtonian fluid mechanics*. McGraw-Hill, 1974. [cited at p. 20, 23, 127, 131]

[73] 350 Second Avenue Waltham MA 02451 USA Foster-Miller, Inc. Femm, 2005. [cited at p. 30]

[74] H. Boese. Data sheet for ad275 mr fluid, personal communication, 2004. [cited at p. 31, 38]

[75] L. M. Jansen and S. J. Dyke. Semi-active control strategies for MR dampers: Comparative study. *Journal of Engineering Mechanics*, 126, 2000. [cited at p. 41]

[76] N. D. Sims, R. Stanway, D. J. Peel, W. A. Bullough, and A. R. Johnson. Smart fluid damping: Shaping the force/velocity response through feedback control. *Journal of Intelligent Material Systems and Sructures*, 11:945–949, 2000. [cited at p. 41]

[77] O. Yoshida. *Torsionally coupled response control of earthquake excited assymmetric buildings: Develoment and application of effective control systems using smart dampers*. PhD thesis, Washington University, 2003. [cited at p. 41, 115]

[78] B. Sapiński. Linearised characterisation of a magnetorheological fluid damper. *Mechanics*, 24:144–149, 2005. [cited at p. 41]

[79] G. K. Kamath and N. M. Wereley. A nonlinear viscoelastic-plastic model for electrorheological fluids. *Smart Materials and Structures*, 6:351–359, 1997. [cited at p. 41]

[80] N. C. Rosenfeld and N. W. Wereley. Volume-constrained optimisation of magnetorheological and electrorheological valves and dampers. *Smart Materials and Structures*, 13:1303–1313, 2004. [cited at p. 41]

[81] Q-H. Nguyen, Y-M. Han, S-B. Choi, and N. W. Wereley. Geometry optimization of MR valves constrained in a specific volume using the finite element method. *Smart Materials and Structures*, 16:2242–2252, 2007. [cited at p. 41]

[82] G. A. Dimock, J-H. Yoo, and N. M. Wereley. Quasi-steady bingham biplastic analysis of electrorheological and magnetorheological dampers. *Journal of Intelligent Material Systems and Structures*, 13:549–559, 2002. [cited at p. 41]

[83] J. Bajkowski. Personal communication. Warsaw Universty of Technology, Faculty of Cars and Heavy Machinery, 2005. [cited at p. 50]

[84] L. Remmers. Personal communication, 2004. EADS Munich Germany. [cited at p. 61]

[85] H. Gavin, J. Hoagg, and M. Dobossy. Optimal design of mr dampers. In K. Kawashima, B. F. Spencer, and Y. Suzuki, editors, *US-Japan Workshop on Smart Structures for Improved Seismic Performace in Urban Regions (Seattle*, pages 225–236, 2001. [cited at p. 63]

[86] A. Milecki. Investigation of dynamic properties and control method influences on mr fluid dampers' performance. *Journal of Intelligent Material Systems and Structures*, 13:453–458, 2002. [cited at p. 63]

[87] Rexroth Bosch Group. www.boschrexroth.com, 2007. [cited at p. 67]

[88] Moog inc. www.moog.com, 2007. [cited at p. 67]

[89] K. Sekuła, G. Mikułowski, and J. Holnicki-Szulc. Real-time dynamic mass identification. In A. Guemes, editor, *3rd European Workshop on Structural Health Monitoring (Granada)*, pages 864–871, 2006. [cited at p. 68, 70]

[90] B. Sapiński and M. Rosół. MR damper performance for shock isolation. *Journal of theoretical and applied mechanics*, 45:133–145, 2007. [cited at p. 70]

[91] T. Kaczorek, A. Dzieliński, W. Dąbrowski, and R. Łopatka. *Podstawy teorii sterowania*. Wydawnictwa Naukowo Techniczne, 2006. [cited at p. 70]

[92] W. Chester. *Mechanics*. London: George Allen & Unwin, 1979. [cited at p. 71]

[93] I23 technical specification. Institute of Aviation, Warsaw, Poland. [cited at p. 88, 90, 139]

[94] D. Batterbee, N. D. Sims, and R. Stanway. ADLAND report: Annex USFD-1(a): Oleo-pneumatic shock absorber modelling and initial MR device sizing. Technical report, University of Sheffield, 2004. [cited at p. 90, 139]

[95] G. Mikułowski and Ł. Jankowski. Adaptive landing gear: optimum control strategy and potential for improvement. *Shock and Vibration*, submitted, 2008. [cited at p. 108]

[96] G. Mikułowski. Durability test of an mr damper. Internal report of SAFEpipes project, unpublished. [cited at p. 114]

[97] J. C. Ulicny, M. P. Balogh, N. M. Potter, and R. A. Waldo. Magnetorheological fluid durability test – iron analysis. *Materials Science and Engineering A*, 443:16–24, 2007. [cited at p. 114]

[98] B. D. Chin, J. H. Park, M. H. Kwon, and O. Ok Park. Rheological properties and dispersion stability of magnetorheological (mr) suspensions. *Rheol Acta*, 40:211–219, 2001. [cited at p. 115]

[99] F. Gordaninejad and D. G. Breese. Heating of magnetorheological fluid dampers. *Journal of Intelligent Material Systems and Structures*, 10:634–645, 1999. [cited at p. 115]

[100] B. Sapiński. Analiza rozkładu temperatury w liniowym tłumiku magnetoreologicznym metodą termograficzną. *Hydraulika i pneumatyka*, 5:13–19, 2001. [cited at p. 115]

[101] M. B. Dogruoz, E. L. Wang F. Gordaninejad, and A. J. Stipanovic. Augmenting heat transfer from fail-safe magnetorheological fluid dampers using fins. *Journal of Intelligent Material Systems and Structures*, 14:79–86, 2003. [cited at p. 115]

[102] I. Bica. The influence of temperature and of a longitudinal magnetic field upon the electrical conductivity of magnetorheological suspensions. *Physica B*, 371:145–148, 2006. [cited at p. 115]

[103] J. Bajkowski. Study of temperature influence on mr damper working parameters. In *Proceedings of 8th conference on active noise and vibration control methods, Krakow-Krasiczyn*, 2007. [cited at p. 115]

[104] J. Bajkowski, J. Nachman, M. Shillor, and M. Sofonea. A model for magnetorheological damper. *Mathematical and computer modelling*, in press, 2007. [cited at p. 115]

Appendices

Appendix A

Reformulation of Newtonian fluid flow equations

The flow equation for an incompressible Newtonian fluid can be expressed as [72]:

$$\rho \frac{D\underline{u}}{Dt} = \rho \underline{g} - \nabla p + \eta \nabla^2 \underline{u}, \tag{A.1}$$

where: $\frac{D\underline{u}}{Dt}$ - material derivative, ρ - fluid density, $\underline{u}$ - fluid velocity vector, g - gravity, p - fluid pressure, η - viscosity of the fluid.

The fluid velocity vector is represented in a Cartesian coordinate system as:

$$\underline{u} = (u, v, w),$$

and the $\nabla^2 \underline{u}$ is defined and formulated in components of Cartesian coordinate system as:

$$\begin{gathered} \frac{\partial^2 u}{\partial x^2} + \frac{\partial^2 u}{\partial y^2} + \frac{\partial^2 u}{\partial z^2} \\ \frac{\partial^2 v}{\partial x^2} + \frac{\partial^2 v}{\partial y^2} + \frac{\partial^2 v}{\partial z^2} \\ \frac{\partial^2 u}{\partial w^2} + \frac{\partial^2 w}{\partial y^2} + \frac{\partial^2 w}{\partial z^2} \end{gathered}$$

Then in the Cartesian coordinate system Eq. (A.1) have the form:

$$\begin{aligned}
\rho \frac{\mathrm{d}u}{\mathrm{d}t} &= \rho g_x - \frac{\partial p}{\partial x} + \eta \left(\frac{\partial^2 u}{\partial x^2} + \frac{\partial^2 u}{\partial y^2} + \frac{\partial^2 u}{\partial z^2} \right), \\
\rho \frac{\mathrm{d}v}{\mathrm{d}t} &= \rho g_y - \frac{\partial p}{\partial y} + \eta \left(\frac{\partial^2 v}{\partial x^2} + \frac{\partial^2 v}{\partial y^2} + \frac{\partial^2 v}{\partial z^2} \right), \\
\rho \frac{\mathrm{d}w}{\mathrm{d}t} &= \rho g_z - \frac{\partial p}{\partial z} + \eta \left(\frac{\partial^2 w}{\partial x^2} + \frac{\partial^2 w}{\partial y^2} + \frac{\partial^2 w}{\partial z^2} \right).
\end{aligned} \tag{A.2}$$

The left hand side of the Eq. (A.1) can be expressed as:

$$\rho \frac{D\underline{u}}{Dt} = \rho \left(\frac{\partial \underline{u}}{\partial t} + (\underline{u} \nabla) \bullet \underline{u} \right) \tag{A.3}$$

which is equivalent to:

$$\rho \frac{D\underline{u}}{Dt} = \rho \left(\frac{\partial \underline{u}}{\partial t} + grad(\underline{u}) \bullet \underline{u} \right).$$

Thus in the Cartesian coordinate system, the components of the material derivative Eq. (A.3) take the form:

$$\begin{aligned}
\rho \frac{du}{dt} &= \rho \left(\frac{\partial u}{\partial t} + u \frac{\partial u}{\partial x} + v \frac{\partial u}{\partial y} + w \frac{\partial u}{\partial z} \right), \\
\rho \frac{dv}{dt} &= \rho \left(\frac{\partial v}{\partial t} + u \frac{\partial v}{\partial x} + v \frac{\partial v}{\partial y} + w \frac{\partial v}{\partial z} \right), \\
\rho \frac{dw}{dt} &= \rho \left(\frac{\partial w}{\partial t} + u \frac{\partial w}{\partial x} + v \frac{\partial w}{\partial z} + w \frac{\partial w}{\partial z} \right).
\end{aligned} \tag{A.4}$$

Then the general form of the Eq. (A.1) formulated in Cartesian coordinate system can be expressed in the following form:

$$\begin{aligned}
\rho \left(\frac{\partial u}{\partial t} + u \frac{\partial u}{\partial x} + v \frac{\partial u}{\partial y} + w \frac{\partial u}{\partial z} \right) &= \rho g_x - \frac{\partial p}{\partial x} + \eta \left(\frac{\partial^2 u}{\partial x^2} + \frac{\partial^2 u}{\partial y^2} + \frac{\partial^2 u}{\partial z^2} \right), \\
\rho \left(\frac{\partial v}{\partial t} + u \frac{\partial v}{\partial x} + v \frac{\partial v}{\partial y} + w \frac{\partial v}{\partial z} \right) &= \rho g_y - \frac{\partial p}{\partial y} + \eta \left(\frac{\partial^2 v}{\partial x^2} + \frac{\partial^2 v}{\partial y^2} + \frac{\partial^2 v}{\partial z^2} \right), \\
\rho \left(\frac{\partial w}{\partial t} + u \frac{\partial w}{\partial x} + v \frac{\partial w}{\partial y} + w \frac{\partial w}{\partial z} \right) &= \rho g_z - \frac{\partial p}{\partial z} + \eta \left(\frac{\partial^2 w}{\partial x^2} + \frac{\partial^2 w}{\partial y^2} + \frac{\partial^2 w}{\partial z^2} \right).
\end{aligned} \tag{A.5}$$

By reduction of the expressions connected with z direction, one can obtain the fluid flow equations for 2D analysis:

$$\begin{aligned}
\rho\left(\frac{\partial u}{\partial t}+u\,\frac{\partial u}{\partial x}+v\,\frac{\partial u}{\partial y}\right) &= \rho g_x-\frac{\partial p}{\partial x}+\eta\left(\frac{\partial^2 u}{\partial x^2}+\frac{\partial^2 u}{\partial y^2}\right),\\
\rho\left(\frac{\partial v}{\partial t}+u\,\frac{\partial v}{\partial x}+v\,\frac{\partial v}{\partial y}\right) &= \rho g_y-\frac{\partial p}{\partial y}+\eta\left(\frac{\partial^2 v}{\partial x^2}+\frac{\partial^2 v}{\partial y^2}\right).
\end{aligned} \tag{A.6}$$

Appendix B

Reformulation of non-Newtonian fluid flow equations

The fluid flow equation was derived from the generalized form of the Navier-Stokes equations [72]. The flow equation for an incompressible, non-Newtonian fluid can be expressed as:

$$\rho \frac{D\underline{u}}{Dt} = \rho \underline{g} + div(\underline{\tau}), \tag{B.1}$$

where: $\frac{D}{Dt}$ - material derivative, ρ - fluid density, $\underline{u}$ - fluid velocity vector, g - gravity, $\underline{\tau}$ - general stresses on the fluid element.

The fluid velocity vector is represented in Cartesian coordinate system as:

$$\underline{u} = (u, v, w).$$

The normal stresses in the Cartesian coordinate system are defined as follows:

$$\tau_{xx} = -p_{xx}, \qquad \tau_{yy} = -p_{yy}, \qquad \tau_{zz} = -p_{zz}. \tag{B.2}$$

Then the components of the Eq. (B.1) can be expressed as:

$$\begin{aligned} \rho \frac{\mathrm{d}u}{\mathrm{d}t} &= \rho g_x - \frac{\partial p_{xx}}{\partial x} + \frac{\partial \tau_{xy}}{\partial y} + \frac{\partial \tau_{xz}}{\partial z}, \\ \rho \frac{\mathrm{d}v}{\mathrm{d}t} &= \rho g_y + \frac{\partial \tau_{yx}}{\partial x} - \frac{\partial p_{yy}}{\partial y} + \frac{\partial \tau_{yz}}{\partial z}, \\ \rho \frac{\mathrm{d}w}{\mathrm{d}t} &= \rho g_z + \frac{\partial \tau_{zx}}{\partial x} + \frac{\partial \tau_{zy}}{\partial y} - \frac{\partial p_{zz}}{\partial zy}. \end{aligned} \tag{B.3}$$

The normal stresses are defined as composition of hydrostatic pressure and the resultant pressure being an outcome of viscosity of the fluid:

$$\begin{aligned} p_{xx} &= p + p'_{xx}, \\ p_{yy} &= p + p'_{yy}, \\ p_{zz} &= p + p'_{zz}. \end{aligned} \tag{B.4}$$

Note that p is hydrostatic pressure that does not depend on shear stresses and normal stresses. According to that assumption, $p'_{xx}, p'_{yy}, p'_{zz}$ also do not depend on p.

The derivatives of the normal stresses are:

$$\begin{aligned} \frac{\partial p_{xx}}{\partial x} &= \frac{\partial}{\partial x}\left(p + p'_{xx}\right) = \frac{\partial p}{\partial x} + \frac{\partial p'_{xx}}{\partial x}\,, \\ \frac{\partial p_{yy}}{\partial y} &= \frac{\partial}{\partial y}\left(p + p'_{yy}\right) = \frac{\partial p}{\partial y} + \frac{\partial p'_{yy}}{\partial y}\,, \\ \frac{\partial p_{zz}}{\partial z} &= \frac{\partial}{\partial z}\left(p + p'_{zz}\right) = \frac{\partial p}{\partial z} + \frac{\partial p'_{zz}}{\partial z}\,. \end{aligned} \tag{B.5}$$

When we assume that the coefficient of increment of the normal stresses to shear rate is K, then we obtain:

$$p'_{xx} = K\,\frac{\partial u}{\partial x}\,, \qquad p'_{yy} = K\,\frac{\partial v}{\partial y}\,, \qquad p'_{zz} = K\,\frac{\partial w}{\partial z}\,. \tag{B.6}$$

Substitution of the Eq. (B.6) to Eq. (B.5) gives:

$$\begin{aligned} \frac{\partial p_{xx}}{\partial x} &= \frac{\partial p}{\partial x} + K\,\frac{\partial^2 u}{\partial x^2}\,, \\ \frac{\partial p_{yy}}{\partial y} &= \frac{\partial p}{\partial y} + K\,\frac{\partial^2 v}{\partial y^2}\,, \\ \frac{\partial p_{zz}}{\partial z} &= \frac{\partial p}{\partial z} + K\,\frac{\partial^2 w}{\partial z^2}\,. \end{aligned} \tag{B.7}$$

If the considered fluid is assumed to be incompressible the following equation is valid:

$$p'_{xx} + p'_{yy} + p'_{zz} = 0, \tag{B.8}$$

which implies the following:

$$p_{xx} + p_{yy} + p_{zz} = 3p \quad \text{or} \quad p = \frac{p_{xx} + p_{yy} + p_{zz}}{3}. \tag{B.9}$$

The material derivative on the left side of the equation can be expressed as:

$$\rho \frac{D\underline{u}}{Dt} = \rho \left(\frac{\partial \underline{u}}{\partial t} + (\underline{u} \nabla) \bullet \underline{u} \right), \tag{B.10}$$

and written in the Cartesian coordinate system components of the material derivative are:

$$\begin{aligned} \rho \frac{du}{dt} &= \rho \left(\frac{\partial u}{\partial t} + u \frac{\partial u}{\partial x} + v \frac{\partial u}{\partial y} + w \frac{\partial u}{\partial z} \right), \\ \rho \frac{dv}{dt} &= \rho \left(\frac{\partial v}{\partial t} + u \frac{\partial v}{\partial x} + v \frac{\partial v}{\partial y} + w \frac{\partial v}{\partial z} \right), \\ \rho \frac{dw}{dt} &= \rho \left(\frac{\partial w}{\partial t} + u \frac{\partial w}{\partial x} + v \frac{\partial w}{\partial y} + w \frac{\partial w}{\partial z} \right). \end{aligned} \tag{B.11}$$

Then the general form of the equations can be expressed in the following form:

$$\begin{aligned} \rho \left(\frac{\partial u}{\partial t} + u \frac{\partial u}{\partial x} + v \frac{\partial u}{\partial y} + w \frac{\partial u}{\partial z} \right) &= \rho g_x - \frac{\partial p}{\partial x} - K \frac{\partial^2 u}{\partial x^2} + \frac{\partial \tau_{yx}}{\partial y} + \frac{\partial \tau_{zx}}{\partial z}, \\ \rho \left(\frac{\partial v}{\partial t} + u \frac{\partial v}{\partial x} + v \frac{\partial v}{\partial y} + w \frac{\partial v}{\partial z} \right) &= \rho g_y - \frac{\partial p}{\partial y} + \frac{\partial \tau_{xy}}{\partial x} - K \frac{\partial^2 v}{\partial y^2} + \frac{\partial \tau_{zy}}{\partial z}, \\ \rho \left(\frac{\partial w}{\partial t} + u \frac{\partial w}{\partial x} + v \frac{\partial w}{\partial y} + w \frac{\partial w}{\partial z} \right) &= \rho g_z - \frac{\partial p}{\partial z} + \frac{\partial \tau_{xz}}{\partial x} + \frac{\partial \tau_{yz}}{\partial y} - K \frac{\partial^2 w}{\partial z^2}. \end{aligned} \tag{B.12}$$

And by reduction of the expressions connected with direction z one can obtain the fluid flow equations for 2D analysis:

$$\begin{aligned} \rho \left(\frac{\partial u}{\partial t} + u \frac{\partial u}{\partial x} + v \frac{\partial u}{\partial y} \right) &= \rho g_x - \frac{\partial p}{\partial x} - K \frac{\partial^2 u}{\partial x^2} + \frac{\partial \tau_{yx}}{\partial y}, \\ \rho \left(\frac{\partial v}{\partial t} + u \frac{\partial v}{\partial x} + v \frac{\partial v}{\partial y} \right) &= \rho g_y - \frac{\partial p}{\partial y} + \frac{\partial \tau_{xy}}{\partial x} - K \frac{\partial^2 v}{\partial y^2}. \end{aligned} \tag{B.13}$$

List of Figures

List of Tables